uc3m | Universidad Carlos III de Madrid

University Degree in Aerospace Engineering

2025-2026

Bachelor Thesis

Wavelet Analysis Of Azimuthal Plasma Instabilities In Hall Effect Thrusters.

Alejandro Ruiz Cepeda

Mario Merino Martínez

Madrid, May 2026

SUMMARY

The anomalous axial electron transport in Hall effect thrusters is largely driven by the Electron Cyclotron Drift Instability. Current studies have focused on the characterization of the saturation regime, which is represented by non-linear interactions that drive this phenomenon. Previous studies have relied on higher-order spectral Fourier analysis like the bicoherence and the bispectrum, which are inherently limited by the assumption that the signal analyzed has a stationary behavior. To overcome this, the current study uses time-resolved tools such as the wavelet bicoherence to reevaluate the Fourier-based analysis performed on a Particle-In-Cell (PIC) simulation of an $E \times B$ discharge. The main outcome of the wavelet analysis was not the identification of newer, previously undetected modes, but rather the identification the cyclic behavior of the spectral properties of the plasma. Additionally, a new intermittent mode associated with ion is identified, which is involved in nonlinear couplings, but does not contribute to the mean-flow transport. Methodologically, multiple bicoherence methods were tested, with the Instantaneous Wavelet Bicoherence being the best suited for this analysis.

Keywords: Electron Cyclotron Drift Instability, Hall Plasma Thrusters, Spectral Analysis, Fourier Analysis, Wavelet Analysis, Bicoherence, Bispectrum, Higher-Order Spectral Analysis

DEDICATION

To my past self who started this: you had no idea how big this project would be, and that was probably for the best.

CONTENTS

LIST OF FIGURES

LIST OF TABLES

ACRONYMS

CD Convergent Divergent 8

COI Cone Of Influence 28

CWT Continuous Wavelet Transform , 25–27, 36–39, 58

DFT Discrete Fourier Transform 23, 29, 42

DWT Dyadic Wavelet Transform 26, 27

ECDI Electron Cyclotron Drift Instability 1–4, 13, 17, 19, 30, 45–47, 50, 68

EDI Electron Drift Instabilities 1, 11

EP Electric Propulsion 7, 8

EPT Electrodeless Plasma Thrusters 1, 69

ESD Energy Spectral Density 29

EVDF Electron Velocity Distribution Function 14, 17

HET Hall Effect Thruster 1–5, 8, 10, 13, 17, 30, 44, 69

HOS Higher-Order Spectral 2, 3, 15, 30, 36, 52, 69

HPT Helicon Plasma Thrusters 1, 69

IWB Instantaneous Wavelet Bicoherence , 37, 39, 52, 57, 59–66, 69

LEO Low Earth Orbit 8

MIA Modified Ion Acoustic 18, 19

NENBW Normalized Equivalent Noise Bandwidth 39

PDF Probability Distribution Function , 42

PIC Particle-In-Cell iii, 2–4, 44

PSD Power Spectral Density 29, 30, 32, 43, 47

SEE Secondary Electron Emission 10

STFT Short-Time Fourier Transform 23–25, 38, 39, 52

VDF Velocity Distribution Function 44

WB Wavelet Bicoherence , 36–40, 52, 57–61, 63, 65, 66

WPS Wavelet Power Spectrum 36, 40, 57

1. INTRODUCTION

1.1. Motivation

Hall Effect Thrusters (HETs) are one of the main types of electric thrusters used on satellites. This type of device works by ionizing a gas in mutually perpendicular electric and magnetic fields, which ejects the ions to produce thrust, while keeping electrons trapped to sustain the discharge.

Fig. 1.1. Picture from NASA's Jet Propulsion Laboratory (JPL) of a HET. On the left, the plasma during operation emitting a blue light characteristic of xenon plasma, on the right the thruster turned off [1].

When the electrons exit their confinement and move towards the anode (upstream) at a rate faster than predicted by theory, the transport is said to be anomalous, which is the main source of performance losses, leading to heating and wall erosion. Being able to simulate the instabilities that cause this transport would help to design more efficient thrusters with longer lifespans.

As an alternative to conventional HETs, Electrodeless Plasma Thrusterss (EPTs) have been in development. These are simpler and more durable thrusters that can operate with different types of propellant. This technology is still maturing, as it offers lower thrust efficiencies compared to classical HETs. An example of an EPT is the Helicon Plasma Thrusters (HPT), which uses radio-frequency electromagnetic waves to ionize and heat the plasma, which is then expelled through a magnetic nozzle. This nozzle channels the magnetized electrons through its diverging field lines, which produce a self-consistent electric field that accelerates the ions. Although these devices do not have electrodes, they are similar to HET in the sense that they are also $\mathrm{E} \times \mathrm{B}$ discharges, and thus are subject to oscillations and instabilities potentially similar to those of HETs [2].

Among all the instabilities, this study will focus on the analysis of the Electron Cyclotron Drift Instability (ECDI), which is one of the most important and widely studied members of the Electron Drift Instabilities (EDI). The ECDI occurs when the acoustic frequency of the ions coincides with the electron cyclotron resonances due to the Doppler shift of the electron motion [3].

Due to the lack of complete physical understanding of plasma properties and the challenges of recreating real-life configurations, the study of the anomalous electron transport relies on a semi-empirical approach, rather than on principle-based derivations. In the case of the ECDI some of the most common methods employed are: coherent Thomson scattering, incoherent Thomson scattering and the use of probes [4]. However, these techniques have some constraints related to the tools themselves, since they might interfere with the plasma or they might not be able to measure precisely the desired property (e.g. the electric field perturbations).

These limitations can be bypassed with the use of PIC simulations. These types of simulations treat the plasma as a collection of macro-particles, each representing a group of real particles, whose trajectories are computed to yield the plasma properties. In order to recreate the real behavior of particles, PIC codes are usually composed of three solvers: the time-integrator to solve the equations of motion, a field solver to compute the evolution of the electromagnetic field, and a set of stochastic Monte Carlo rules for collisions and surface processes [5]. However, the precision of PIC simulations comes at a high computational cost and produces large datasets that require complex analytical tools for their analysis [4].

In the case of ECDI it is especially difficult to analyze the data due to the turbulent nature of the flow, nonlinear couplings, and because the spectral content of the plasma properties evolves over time. To deal with this, recent studies have relied on Fourier Higher-Order Spectral (HOS) analysis such as bicoherence to analyze this nonlinear behavior [3]. But this method assumes the signal to be stationary, which calls for the use of more complex tools such as the wavelet transforms that allow the analysis of the time-varying spectral properties of the plasma.

1.2. Objectives

Of all the types of instabilities that occur in HETs, this study will focus on the previously described ECDI, which has been found to be one of the principal contributors to the anomalous electron transport [3], [4], [6].

The existence of this instability was first discovered by Forslund et al. [7], who established the basis for the kinetic theory of the ECDI, which is a well-established topic [8], [9]. Later studies confirmed the existence of this instability in experimental setups [10], [11]. Additionally, the ECDI has also been described from a fluid perspective by Ramos et al. [12] with a model that assumes electrons and ions as two distinct and interacting fluids moving through an $E \times B$ field. This model is able to recreate the ECDI predicted by kinetic theory in addition to other types of instabilities that can arise in these discharges. Nevertheless, the nonlinear evolution of the ECDI is not yet fully understood.

On the simulation side, Adam et al. [13] were the first to develop a 2D fully-kinetic simulation of a HET. Their results hinted at the azimuthal drift of particles as being responsible for the oscillations of the electron density and electric field, which resulted in the anomalous transport. From then on, PIC tools have become essential tools for the study of plasma instabilities. This work relies on PICASO, a PIC code developed by *The Plasma & Space Propulsion Team (EP2)* [6], which was built for the study of the nonlinear evolution of ECDI in the 2D axial-azimuthal plane, resembling the geometry of a $\mathrm{E} \times \mathrm{B}$ discharge.

To study plasma oscillations in $\mathrm{E} \times \mathrm{B}$ discharges a variety of analysis tools have been applied, ranging from modal decomposition [14], to the Fourier bicoherence. This project builds on the work of Bayón-Buján et al. [3], in which they use HOS analysis to study the modes associated with the saturation region of the ECDI by analyzing an $\mathrm{E} \times \mathrm{B}$ discharge. Their analysis of the data indicated that the fundamental ECDI mode is the principal contributor to the anomalous transport. While higher wavenumber modes do not contribute directly to the anomalous electron transport, they showcase nonlinear coupling between one another and with the fundamental mode, engaging with additional modes not predicted by the linear theory described above. However, Fourier bicoherence assumes a stationary spectrum, which was previously shown to not be the case since the instability showcases an intermittent behavior [15]. As a result, short-lived structures might go undetected by the averaging performed by this method.

This thesis reevaluates these results, addressing the non-stationary behavior of the plasma by using wavelet analysis, a time-resolved tool that is better suited for these types of flows. The main hypothesis is that wavelet analysis can reveal interactions that were kept hidden with Fourier tools.

Therefore, the objectives of this thesis are:

(i) To review the literature on plasma discharges and the ECDI.

(ii) To review the principles of Fourier and wavelet analysis, and compare both methods theoretically.

(iii) To implement the wavelet power spectrogram, wavelet bicoherence and Fourier windowed bicoherence using MATLAB[1].

(iv) To apply these wavelet techniques to the same PIC simulation data used by Bayón-Buján et al. [3] and to compare them to the Fourier methods previously used, evaluating if they can reveal any new information.

(v) To physically interpret the results, evaluating whether the wavelet analysis confirms the couplings found by Bayón-Buján et al. [3] and which behaviors, if any, are revealed by the time-resolved analysis.

[1]The implementation is available upon request at `https://github.com/AlexRCepe/TFG-Wavelets`.

1.3. Thesis Structure

The thesis is structured to provide a progressive and comprehensive approach towards the final results. Chapter 2 begins with a review of space propulsion and the different types of electric propulsion devices. Next, the foundation necessary to understand the formation of the ECDI in HETs is reviewed. This is divided into three parts: the first discusses plasma behavior under $E \times B$ electromagnetic fields, the second reviews how waves are described in a plasma, and the third one joins both concepts to explain the physics behind the ECDI.

Chapter 3 starts with a review of the basics of Fourier and wavelet analysis. Then the concepts of power spectrum and higher-order spectrum are introduced for both Fourier and wavelet analysis. Here, two different wavelet bicoherence approaches are explained and compared. Finally, the wavelet selection is discussed.

In Chapter 4 the methodologies previously discussed are applied to the results of a PIC simulation, and the Fourier and the two wavelet bicoherence approaches are compared. Finally, Chapter 5 summarizes the main findings and proposes possible directions for future work.

1.4. Socioeconomic Environment & Regulatory Framework

1.4.1. Regulatory Framework

Although more than 50 years have passed since the first time a human stepped on the moon, space regulation is still a relatively new field for lawmakers. The first laws related to space were the Outer Space Treaty (1967) [16], signed by 108 countries by the year 2019 [17]. This treaty set a regulatory framework for non-appropriation, liabilities, and international cooperation. With the arrival of the 2020s, increasing geopolitical tensions between countries have forced governments to seek space independence, giving rise to new proposals to regulate space. Despite this, there are still no laws that directly regulate electric thrusters or any kind of space propulsion systems. However, other broader laws still have an impact on these types of devices. One example is the EU Space Act [18], which was proposed in June of last year. This is an initiative which aims to unify the regulatory framework in the Union, but puts a big emphasis on space debris, which will require constellations of ten or more satellites to be equipped with propulsion systems to avoid collisions. In addition, Spain is preparing its own Space Law whose aim is to provide legal certainty to the national space sector, including companies working on plasma thrusters [19].

1.4.2. Socioeconomic Impact

Due to the increase in satellite demand, there has been an increase in the global market for electric propulsion systems. Although the figures vary depending on the source, all projections expect the market for these types of devices to roughly double by the year 2034 [20], [21]. Electric propulsion is preferred over chemical propulsion for satellites mainly due to its higher fuel efficiency, which makes them more suitable for missions of longer duration. Of the whole electric propulsion market, it is estimated that roughly 38% is held by HETs by value, which are one of the main solutions used for the propulsion systems by the primary low-Earth-orbit megaconstellations (Starlink, OneWeb, Kuiper, etc.) [22].

As was previously described, plasma thrusters are subject to instabilities that reduce their efficiency and lifetime. Having predictive models of such behavior could reduce development costs, and consequently the cost of electrical propulsion systems. An overall decrease in their cost would help further develop the democratization of space, providing reliable connectivity in remote places and enabling the growth of IoT-related services. At the same time, a lower cost would incentivize installation of these devices in all types of satellites, enabling collision avoidance maneuvers and safe-deorbiting trajectories, which would reduce space debris.

1.4.3. Budget

The total budget for the realization of this project is summarized in Table 1.1.

As a remark, electricity was calculated as the power consumption of the computer (230 W) and the router (8 W [27]) during working hours. For the computer, a period of 4 years of amortization was assumed, as suggested by the Spanish tax agency [28] for a total purchase price of 1050.00 €.

The hourly cost of personnel is taken as the total cost it would have for the employer, which includes the gross salary and the social-security contributions, which were approximately 30% for 2026 [29].

TABLE 1.1. TOTAL BUDGET.

Item	Amount	Unity	Unitary cost [€/unit]	Price [€]
Student Labor (Junior Engineer)	800	hours	30.00	24,000.00
Advisor Supervision (Senior Professor)	30	hours	45.00	1,350.00
Hardware Amortization (HP Victus with Intel i7 processor and NVIDIA RTX 4060)	1.75	years	262.50	459.38
MATLAB License (Student Suite + Wavelet Toolbox)	1.75	years	106.00	185.50
Electricity	190.4	kW·h	0.14	26.66
Internet (Movistar basic plan)	21	months	35.00	735.00
Total				26,756.54

Source: [23]–[26]

2. PLASMA PHYSICS OF HALL EFFECT THRUSTERS

2.1. Propulsion Basics

According to Newton's first law, an external force must be applied to an object to change its state of motion (i.e., to move it from rest or alter its constant velocity). To produce this force, spacecraft take advantage of Newton's third law: for every action, there is an equal and opposite reaction. By applying this principle, space vehicles expel hot gases, which produces a reactive force called *thrust*. This thrust can be described by the following equation [30]:

$$F = \dot{m}v_e + (p_e - p_a)\,A_e$$

This equation can be divided into two terms: the *jet thrust* and the *pressure thrust*. The first term, $\dot{m}v_e$, relates the mass flow rate of the gases that exit the nozzle ($\dot{m}$) to their exhaust velocity (v_e). This jet thrust represents the force generated by the momentum exchange between the spacecraft and the expelled gases. The second term, $(p_e - p_a)\,A_e$, represents the pressure thrust. It accounts for the force contribution from the difference between the exhaust pressure at the exit of the nozzle (p_e) and the ambient pressure (p_a), acting on the exit area of the nozzle (A_e). For ion and Hall thrusters, this second term is usually ignored, because the jet thrust is much larger than the pressure thrust: $\dot{m}v_e \gg (p_e - p_a)\,A_e$ [31].

To measure the efficiency of a propulsion system, the *Specific Impulse* (I_{sp}) is commonly used. This quantity allows for the comparison and classification of different propulsion systems by relating the thrust produced to the rate of propellant consumption. It is defined as [30]:

$$I_{sp} = \frac{F}{\dot{m}\,g_e}$$

where g_e is Earth's gravity at sea level (9.81 m/s^2) and is used as a convention to give the specific impulse units of seconds. Table 2.1 gives a superficial comparison of the propulsion systems that are being used today. Overall, one can say that chemical propulsion systems have lower specific impulse, consequently worse fuel efficiency, high thrust, reduced acceleration times and high mass. On the other hand, Electric Propulsion (EP) has much better fuel efficiency, thus less fuel and a propellant reservoir are required. This difference makes EP more suitable for small satellite applications (under 500 kg [32]).

TABLE 2.1. CLASSIFICATION OF MULTIPLE PROPULSION SYSTEMS

System	Typical I_{sp} range [s]
Solid rocket motor	150–350
Liquid rocket engine – monopropellant	200–250
Liquid rocket engine – bipropellant	300–460
Hybrid rocket engine	300–350
Nuclear thermal engine	800–1000
Hall Effect Thrusters	500–3000
Arcjet	400–1500
Ion	1000–10,000

Source: [30], [32]

2.2. Electric Propulsion Devices

Electric Propulsion can be defined as "The use of energy from a source not stored in the chemical bonds of the propellants to augment or provide the exhaust velocity of the propulsion device" [30]. As mentioned before, these systems are mainly used in smallsats in Low Earth Orbit (LEO), but they are also one of the preferred methods when talking about deep space exploration [4], [33]. These kinds of thrusters usually have a lifespan of 10,000 hours and produce 0.1-1 N [34].

EP systems can be divided into three main categories: *electrothermal propulsion*, *electromagnetic propulsion* and *electrostatic propulsion*. The first type, electrothermal, is very similar to chemical propulsion in the sense that both methods heat up the propellants, which are then exhausted through a Convergent Divergent (CD) nozzle. In the case of Arcjet thrusters, this increase of temperature is achieved by passing a current through two electrodes of opposite polarity at both ends of a narrow duct to induce a sustained electric arc [32]. Another example of electrothermal propulsion systems the *Resistojet* thruster. On the other hand, there is electromagnetic propulsion, in which the propellant is ionized and accelerated by the application of electric and magnetic fields. Devices such as *Pulsed Plasma Thrusters* and *Magneto-Plasma Dynamics Thrusters* enter this category [32]. Finally, electrostatic thrusters work by ionizing propellant through the application of electric power. The propellant is then accelerated via the electric field produced by the electrodes. Here, one can find different technologies such as *Electrospray Thrusters*, *Gridded Ion Thrusters* and *Hall Thrusters*.

2.2.1. Hall Thrusters

Among all types of electrostatic thrusters, the most interesting one from the perspective of this study is the HETs or Stationary Plasma Thruster (SPT). Figure 2.1 showcases the usual construction of a HET. In this type of device, a direct electric field at the exit is used

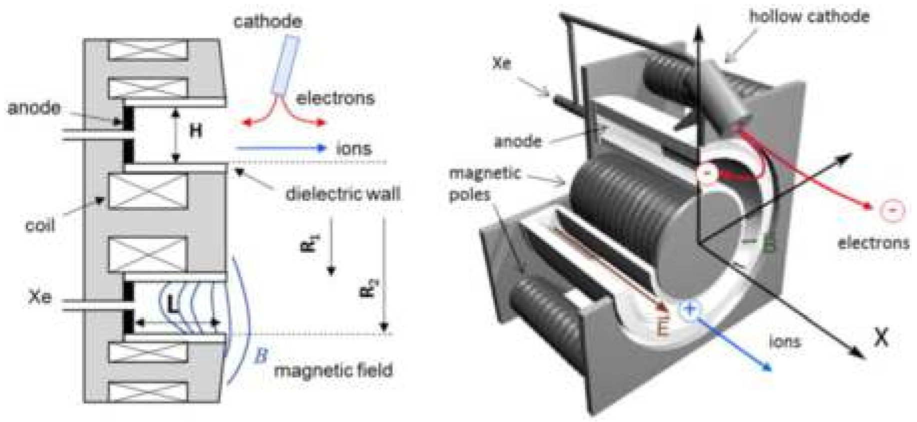

Fig. 2.1. Schematic of a typical Hall Effect Thruster. Reprinted from J.-P. Boeuf, "Tutorial: Physics and modeling of hall thrusters," *Journal of Applied Physics*, vol. 121, no. 1, p. 011 101, 2017. DOI: 10.1063/1.4972269, with the permission of AIP Publishing.

to accelerate ions and produce thrust. This force pushing on the device is also described as the Lorentz Force acting on the electron current and is equivalent to the electrostatic force acting on the ions [31]:

$$F = 2\pi \iint q\, n_e\, \vec{u}_e \times \vec{B}\, r\, dr\, dz = 2\pi \iint q\, n_i\, \vec{E}\, r\, dr\, dz$$

where q is the charge of an ion, n_i is the ion number density, $\vec{E}$ is the electric field at the thruster, n_e is the electron number density, $\vec{u}_e$ is the electron drift velocity, which is described as $\vec{u}_e = (\vec{E} \times \vec{B})/B^2$, and $\vec{B}$ is the magnetic field applied by the thruster. In order to improve the impulse generated by such devices, one can take advantage of the fact that plasmas are relatively good at conducting electricity and the electric field far from the walls is normally small. One of the ways of achieving this is by decreasing the electron conductivity, which can be done by applying a magnetic field perpendicular to the electron current [35]. This magnetic field is usually of the order of 150 Gauss, which is enough to magnetize electrons, whilst not affecting the ions since they have a much greater Larmor radius [34].

As a consequence of the addition of the magnetic field, electrons are trapped in an azimuthal $\vec{E} \times \vec{B}$ drift around the annular channel and slowly move towards the anode (Figure 2.2). This effect is commonly referred to as the Hall Effect. These trapped electrons at the exit of the channel are then used to ionize the propellant, usually xenon [34], which is fed through the anode.

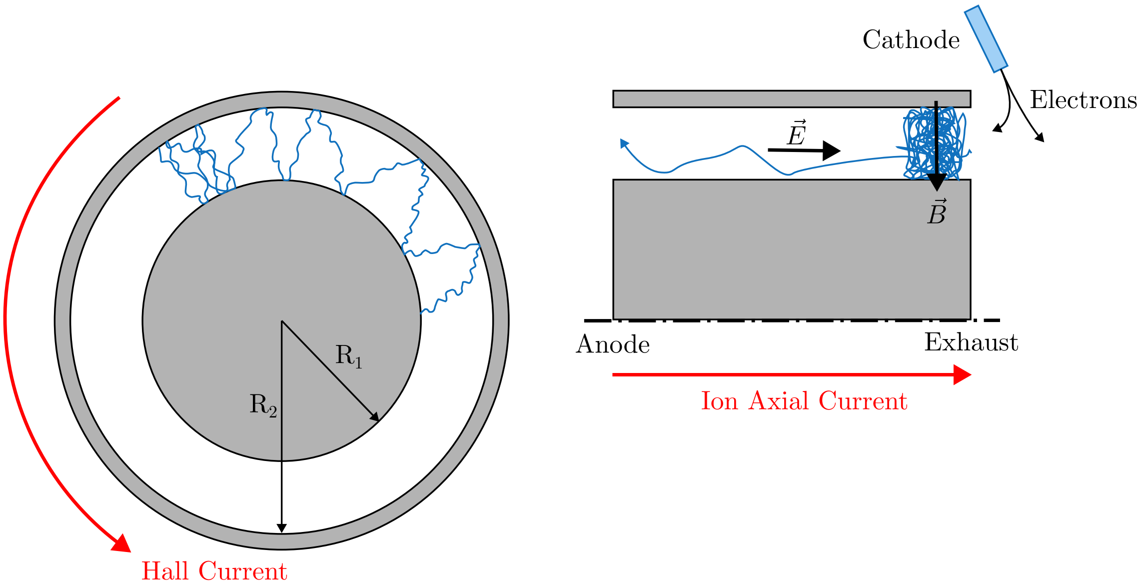

Fig. 2.2. Trajectory of a single electron on a simplified sketch of a HET. On the right side, 2D trajectory on the annular channel. On the left side, the 1D trajectory of the electron along the axial direction.

2.3. Instabilities In $E \times B$ Devices

$E \times B$ devices are those in which a strong electric field is generated by the application of an external magnetic field perpendicular to the discharge current. Among them, we can find HETs and CD magnetrons for plasma processing.

The most recent studies in the field have focused on investigating the instabilities that arise in these devices, which cause anomalous electron transport towards the anode. This phenomenon is relevant for the development and improvement of $E \times B$ devices, since anomalous transport is the main source of performance losses [3]. Some of the most common types of instabilities in $E \times B$ devices are:

- **Plasma Wall Interactions**: thrust performance can be influenced by the wall material through an effect called Electron-Induced Secondary Electron Emission (SEE), which causes additional transport across the magnetic field. These interactions between the plasma and the wall have been shown to affect the magnitude and fluctuation frequency (known as the breathing mode) of the discharge current. However, thrust and thrust efficiency are less affected by these [4]. SEE becomes more notable when the flux of emitted electrons is greater than the flux of primary electrons.

- **Low Frequency Oscillations**: this is one of the most notable instabilities at device scale. It is described as oscillations below 100 kHz, which are able to reach up to 100% modulation of the plasma parameters. In other words, this type of motion is able to produce fluctuations that can change plasma values by 100%. Low frequency oscillations are dominated by two major modes: the breathing mode and the spoke mode. The first mode is propagated axially in HETs, being one of the most powerful for these devices. These oscillations can have amplitudes as big as the mean discharge current. The second mode is manifested as strong disturbances in plasma density which travel in the $\mathrm{E} \times \mathrm{B}$ direction (azimuthal direction for cylindrical devices) [4].

- **EDI**: these are high-frequency, short wavelength oscillations that appear in partially magnetized $\mathrm{E} \times \mathrm{B}$ plasmas and cause an increase in electron movement across the magnetic field [4].

2.3.1. Behavior Of A Plasma Under An $\mathrm{E} \times \mathrm{B}$ Electromagnetic Field

The interaction of charged particles with electromagnetic fields is described by the Lorentz Force. For a non-relativistic particle ($v^2 \ll c^2$) with charge q and moving with velocity $\vec{v}$, it relates its momentum ($\vec{p} = m\vec{v}$) to the electric $\vec{E}$ and magnetic field $\vec{B}$ to which it is subject [36]:

$$m \cdot \frac{d\vec{v}}{dt} = q \cdot (\vec{E} + \vec{v} \times \vec{B}) \tag{2.1}$$

Therefore, if the plasma is formed by N different particles, it would be possible to describe the dynamics of the plasma by solving the N nonlinear coupled differential equations, knowing the external fields applied and the internal ones generated by the motion of the plasma particles. Note that the equations used to describe the dynamics of the particles are intrinsically coupled with those that describe the existing electric and magnetic fields. In other words, the motion of the particles influences the internally produced fields, which, at the same time, produce a change in the motion of particles. As the instabilities studied in this chapter are purely electrostatic, the evolution of the electric field will be determined by Poisson's Equation:

$$\vec{\nabla}^2 \phi = -\frac{\rho}{\epsilon_0} \tag{2.2}$$

where ϵ_0 is the electric permittivity of free space and ρ is the plasma charge density. In order to study the motion of the particles inside the plasma, Equation 2.1 is solved for the velocity. To do so, the velocity and electric field are divided into two components: one parallel to the magnetic field and another perpendicular to it. Applying this to Equation 2.1 gives [36]:

$$m \cdot \frac{d\vec{v}_\parallel}{dt} = q \cdot \vec{E}_\parallel \tag{2.3}$$

$$m \cdot \frac{d\vec{v}_\perp}{dt} = q \cdot (\vec{E}_\perp + \vec{v}_\perp \times \vec{B}) \tag{2.4}$$

From Equation 2.3 it can be clearly seen that the particle is following a uniformly accelerated motion in this direction with acceleration $q \cdot E_\parallel / m$. However, the motion in

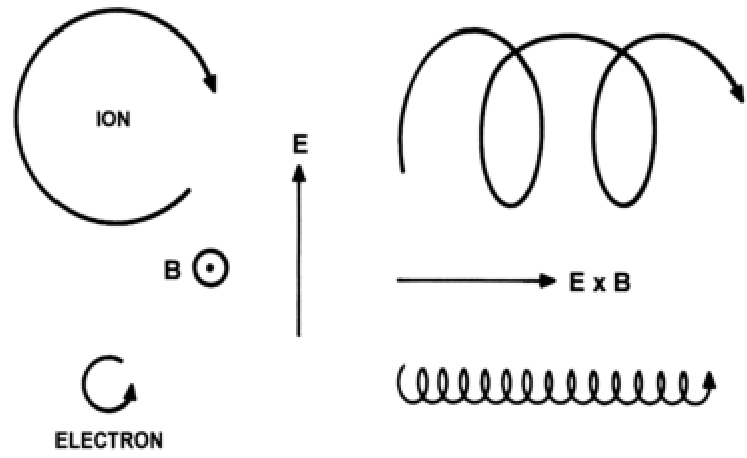

Fig. 2.3. Cycloidal trajectory of an ion (upper part of the image) and an electron (lower part of the image). The Magnetic and Electric drift causes the particles to move in the direction of E × B . Note that for ions and electrons the direction of rotation is opposite, due to the opposite charges [36].

the perpendicular direction has a more complex solution. In this case, it is convenient to divide the perpendicular component of the particle's velocity into a constant and a time-varying term such that $\vec{v}_\perp = \vec{v}'_\perp + \vec{u}_d$. The constant part of the previous expression, $\vec{u}_d$, is called the E × B drift velocity and is described as [36]:

$$\vec{u}_d = \frac{\vec{E}_\perp \times \vec{B}}{B^2} \tag{2.5}$$

Note that since this term does not vary with time, the velocity $\vec{v}'_\perp$ can be considered as the velocity of the particle as seen from an observer that is moving at constant velocity $\vec{u}_d$. Under this assumption, the differential equation becomes [36]:

$$m \cdot \frac{d\vec{v}'_\perp}{dt} = q \cdot (\vec{v}'_\perp \times \vec{B}) \tag{2.6}$$

Equation 2.6 describes a circular motion with frequency ω_c and radius ρ [36]:

$$\vec{v}'_\perp = \vec{\omega}_c \times \vec{\rho}$$

Here, ω_c denotes the *Cyclotron Frequency*, described as $\omega_c = (|q| \cdot B)/m$, and ρ is the distance from the *Instantaneous Center of Gyration* of the particle (also known as *gyrocenter* or *guiding center*) to the particle itself. The radius of this circular orbit is usually referred to as the *Radius of Gyration* or *Larmor Radius*, which is defined as [36]:

$$\vec{\rho} = \frac{m}{|q|\,B^2}(\vec{v} \times \vec{B})$$

Whenever both the electric and the magnetic fields are perpendicular to each other, the parallel component of the electric field disappears, making the particles move in the same way as sketched in Figure 2.3. Under this condition, the expression for the gyrocenter's position and velocity can be obtained in Cartesian coordinates. To do so, the following electric and magnetic fields are defined:

$$\vec{B}_0 = B_0\vec{e}_x$$
$$\vec{E}_0 = E_0\vec{e}_z$$

where the x, y and z directions resemble the radial, azimuthal, and axial directions of an HET. This mutually perpendicular electromagnetic field produces an electron drift velocity $\vec{u}_{ye0} = u_{ye0}\vec{e}_y$. Note that u is used to refer to the average or bulk velocity of a species, while v denotes the velocity of individual particles. The position of the gyrocenter for this motion is defined as $\vec{r}_g = \vec{r} - \vec{\rho}$, where $\vec{r} = x\,\vec{e}_x + y\,\vec{e}_y + z\,\vec{e}_z$ is the position of the particle, which moves with velocity $\vec{v} = v_x\vec{e}_x + v_y\vec{e}_y + v_z\vec{e}_z$. Using all of this, the following expression of the position is obtained:

$$\vec{r}_g = \vec{r} - \vec{\rho} = \vec{r} - \frac{m}{e\,B_0^2}(\vec{v} \times \vec{B}_0) = \left(y_e - \frac{m \cdot v_{ze}}{e \cdot B_0}\right)\vec{e}_y + \left(z_e + \frac{m \cdot v_{ye}}{e \cdot B_0}\right)\vec{e}_z \tag{2.7}$$

where e is the elementary charge. Since both fields are perpendicular, the velocity parallel to the magnetic field is zero because $E_{\parallel} = 0$, meaning the resulting velocity would be in the $\mathrm{E} \times \mathrm{B}$ direction. On the other hand, the perpendicular velocity was previously defined as $\vec{v}_{\perp} = \vec{v}'_{\perp} + \vec{u}_d$. In this case $\vec{v}_{\perp}$ is the velocity of the particle with respect to the stationary reference frame and $\vec{v}'_{\perp}$ is the velocity of the particle with respect to the gyrocenter. This means that the drift velocity is actually the velocity of the guiding center:

$$\frac{d\vec{r}_g}{dt} \equiv \vec{u}_g = \vec{u}_d = \frac{\vec{E}_0 \times \vec{B}_0}{B_0^2} = \frac{E_0}{B_0}\vec{e}_y = u_{ye0}\vec{e}_y$$

In the context of ECDI it is important to add an extra term to the electric field vector corresponding to the perturbation of the electric potential due to the formation of the instability: $\vec{E}_1 = -\vec{\nabla}\phi$ [2]. Under the assumption that this perturbation varies very slowly and that the plasma is 2D (the plasma exists in the y-z plane), the position of the gyrocenter remains unchanged (Equation 2.7). However, for the velocity, the drift velocity due to this disturbance of the potential has to be taken into account:

$$\vec{u}_g = \left(u_{ye0} + \frac{E_{z1}}{B_0}\right)\vec{e}_y - \frac{E_{y1}}{B_0}\vec{e}_z$$

[2] Throughout this document the subscript "0" is employed to denote equilibrium conditions, whilst "1" stands for perturbed conditions.

The expressions given up to now are only used to describe the behavior of a single particle inside the plasma. However, when the number of particles N is significantly large, this becomes impractical. In order to facilitate dealing with plasma properties, a statistical approach is followed. In this way, the velocities of particles within the plasma are described by a velocity distribution function $f(\vec{r}, \vec{v}, t)$, which depends on time, position ($\vec{r}$), and velocity ($\vec{v}$). Knowing this expression allows us to determine the macroscopic properties of the plasma. For example, the particle density can be obtained as follows [37]:

$$n(\vec{r}, t) = \int f(\vec{r}, \vec{v}, t)\, d\vec{v}$$

Finally, it is also relevant to talk about how the plasma electron current behaves in the z-direction, which will later be investigated and will be referred to as the axial direction. The total plasma current is given by:

$$\vec{j}_p = \sum_s n_s \cdot q_s \cdot \vec{u}_s \tag{2.8}$$

where s denotes a given species within the plasma. For electrons, Equation 2.8 becomes $\vec{j}_e = n_e \cdot (-e) \cdot \vec{u}_e$. Now, the collisionless electron momentum equation on the y-axis is given by [38]:

$$\frac{\partial(n_e\, m_e\, \vec{u}_{ye})}{\partial t} + \vec{\nabla}\, [P_e + m_e\, n_e\, \vec{u}_e\, \vec{u}_e]_y = -n_e\, e\left(\vec{E} + \vec{u}_e \times \vec{B}_0\right)_y \tag{2.9}$$

where P_e is the electron pressure tensor and m_e is the mass of electrons. In order to simplify the latter equation, the *Electron Momentum Tensor* is introduced. This quantity is described as follows:

$$M_e = \iiint \vec{v}_e \vec{v}_e f_e\; d^3\vec{v}_e$$

where f_e is the Electron Velocity Distribution Function (EVDF). This new quantity is related to the electron pressure tensor as $m_e\, M_e = P_e + m_e\, n_e\, \vec{u}_e\, \vec{u}_e$ [39], so that:

$$\vec{\nabla}\, [P_e + m_e\, n_e\, \vec{u}_e\, \vec{u}_e]_y = m_e\, [\vec{\nabla} M_e]_y = m_e \left(\frac{\partial M_{yye}}{\partial y} + \frac{\partial M_{zye}}{\partial z}\right)$$

Additionally, to further simplify the left-hand side of Equation 2.9 one can realize that the only component of the electron field in the y-direction is E_{y1} and notice that $\left[(-en_e\vec{u}_e) \times \vec{B}_0\right]_y = \left[\vec{j}_e \times \vec{B}_0\right]_y = j_{ze} B_0$. Introducing all of this into 2.9 and rearranging the terms gives the expression for the azimuthal electron current:

$$j_{ze}(t, y) = en_e \frac{E_{y1}}{B_0} + \frac{m_e}{B_0}\left(\frac{\partial M_{yye}}{\partial y} + \frac{\partial M_{zye}}{\partial z} + \frac{\partial(n_e \vec{u}_{ye})}{\partial t}\right) \tag{2.10}$$

Looking at Equation 2.10, one can see that it is composed of two terms. The first, $j^E_{ze} = e\, n_e\, E_{y1}/B_0$, is the first-order $\mathrm{E} \times \mathrm{B}$ contribution to the axial electron flux, which originates from the perturbed azimuthal field E_{y1}. The second is an extra contribution given by the electron's momentum when the particles have a finite characteristic Larmor radius $\rho_{e0} = \sqrt{m_e T_{e0}}/(eB_0)$, where T_{e0} is the electron's temperature expressed in electron volts (eV). As a whole, these two terms are related to each other as [3]:

$$j_{ze}(t,y) = j_{ze}^{E}(t,y) + O\left(e\, n_e\, c_{e0}\, \frac{\rho_{e0}}{L_z}\right)$$

where L_z is the span of the axial domain and $c_{e0} = \sqrt{T_{e0}/m_e}$ is the thermal velocity of electrons. By describing the density as a constant and a fluctuating term, such that $n_e = n_0 + n_1$, and by taking the average of the flux, the following expression is obtained:

$$\langle j_{ze}(t,y)\rangle_{avg} \approx \langle j_{ze}^{E}(t,y)\rangle_{avg} = \frac{e}{B_0}\langle n_e E_{y1}\rangle_{avg} = \frac{e}{B_0}\langle n_1 E_{y1}\rangle_{avg}$$

where $\langle\cdot\rangle_{avg}$ represents the average. Note that the term with n_0 vanishes due to it having a constant value, and E_{y1} having zero-mean. Although E_{y1} and n_1 can be seen as two separate signals with zero-mean, their product, $\langle n_1 E_{y1}\rangle$, does not average to zero as long as the oscillations of these plasma properties are correlated. This correlation is the origin of the anomalous electron transport. Because this flux depends on the phase coupling between E_{y1} and n_1, it calls for tools such as HOS for the analysis of this phenomenon, which are described in the next chapter.

2.3.2. Plasma Sound Waves

Previously, a kinetic interpretation of the motion of plasmas was seen. However, it is not desirable to study the individual particles that form it, but rather it is more suitable to study their collective behavior. To do so, fluid models are usually employed, with the key distinction from regular fluids being that plasmas are affected by electromagnetic fields.

As in any other fluid, when it is disturbed, oscillations appear which can be modeled by Fourier analysis into a set of sinusoidal functions with different frequencies and wavenumbers. Whenever these oscillations have a small amplitude they can be described as a single sinusoidal function, which will be represented as:

$$\mathcal{X}_1 = \mathcal{X} \cdot \exp\left[i\left(\vec{k} \cdot \vec{r} - \omega t\right)\right] \tag{2.11}$$

where $\mathcal{X}$ represents any plasma property and $\vec{k} \cdot \vec{r} = k_x x + k_y y + k_z z$, where k_x, k_y and k_z are the wavenumbers in the x, y and z directions, respectively. When looking at a point of constant phase, it moves according to the following expression:

$$\frac{d(kx - \omega t)}{dt} = 0, \qquad \text{or} \qquad \frac{dx}{dt} = \frac{\omega}{k} \equiv v_\varphi$$

Here v_φ is the *Phase Velocity*. This velocity is usually higher than the speed of light c, which does not violate the theory of relativity, since an infinitely long wave train of constant amplitude does not carry information. However, information is not transmitted at the phase velocity, but rather at the *Group Velocity*, which is defined as:

$$v_{group} = \frac{d\omega}{dk}$$

In a regular fluid, such as air, information travels at the speed of sound, which is described as:

$$\frac{\omega}{k} = \left(\frac{\gamma k_B T}{M}\right)^{1/2}$$

where M is the mass of the fluid, k_B is the Boltzmann constant and T is the temperature of the fluid expressed in Kelvin. This quantity indicates the speed at which pressure waves travel through a fluid medium by collision of adjacent molecules. For plasmas with no neutral particles and few collisions, a similar phenomenon occurs, which is called an *ion acoustic wave* or *ion wave*.

Without collisions, regular sound waves cannot take place. However, the charge of ions allows oscillations to be transmitted between them by a perturbation of the electric field. In order to study how these oscillations affect the ion's particle density, the ion momentum equation in the presence of an electric field $\vec{E} = -\vec{\nabla}\phi$ and the absence of magnetic fields is as follows [40]:

$$m_i\, n \left[\frac{\partial \vec{u}_i}{\partial t} + \left(\vec{u}_i \cdot \vec{\nabla}\right)\vec{u}_i\right] = e\, n\, \vec{E} - \vec{\nabla} p = -en\vec{\nabla}\phi$$

Note that since the ions are cold ($k_B T_i \rightarrow 0$), the ion pressure $p_i = n_i k_B T_i \rightarrow 0$, and as a consequence the pressure gradient contribution vanishes [40]. Linearizing and assuming planar waves gives:

$$-i\omega m_i n_0 u_{i1} = -en_0 ik\phi_1 \tag{2.12}$$

Now, the ion continuity equation is used and linearized in the same way as the momentum one:

$$\frac{\partial n_i}{\partial t} = -\vec{\nabla} \cdot (n_i \vec{u}_i) \implies -i\omega n_{i1} + ikn_0 u_{i1} = 0 \tag{2.13}$$

Putting Equations 2.12 and 2.13 together, an expression for the perturbed ion particle density is obtained [8]:

$$n_{i1} = \frac{n_0 k^2 e\phi_1}{m_i \omega^2}$$

2.3.3. ECDI Dispersion Relation

In order to better understand how ECDI behaves, it is important to obtain the dispersion relation for this instability. For any plasma oscillation, the wave modes are described by this dispersion relation, which relates the wave frequency to the wavenumber. To do so, the same setup as that used at the end of Chapter 2.3.1 is employed. This consists of a collisionless 2D plasma with mutually perpendicular electric and magnetic fields, resembling a HET. It is assumed that the magnitude of the magnetic field is such that the electrons have a drift velocity $\vec{u}_{ye0} = u_{ye0}\vec{e}_y$, while the ions are kept unmagnetized due to their higher Larmor radius. In addition, it will also be assumed that the particle density of the unperturbed plasma is constant throughout the space $n(x, y, z) = n_0$. In this configuration, the ECDI is modeled as a pure electrostatic perturbation:

$$\phi = \phi_0 \exp\left[i(k_x x + k_y y + k_z z - \omega t)\right] \tag{2.14}$$

At equilibrium, electrons follow a typical Maxwellian EVDF, with a density n_0 and temperature T_{e0} shifted by the drift velocity [8]:

$$f_0 = n_0 \left(\frac{m_e}{2\pi T_{e0}}\right)^{3/2} \exp\left[-\frac{(v - u_{ye0})^2}{2\, c_{e0}^2}\right]$$

Note that, when taking into account the perturbation, the Vlasov equation is satisfied by the electron distribution function f_e, such that [8]:

$$\frac{\partial f_e}{\partial t} + \vec{v}_e \cdot \frac{\partial f_e}{\partial \vec{r}} - \frac{e}{m}\left[-\vec{\nabla}\phi + \vec{v}_e \times \vec{B}_0\right] \cdot \frac{\partial f_e}{\partial \vec{v}_e} = 0 \tag{2.15}$$

Equation 2.15 can be used to obtain the perturbed electron density. To do so, f_e is linearized, and the Vlasov equation is integrated along the unperturbed orbits, giving [6]:

$$\frac{n_{e1}}{n_0} = \left[1 - g(\omega_e, b_e; \omega_{ce})\right] \frac{e\,\phi}{T_{e0}} \tag{2.16}$$

with

$$g(\omega_e, b_e; \omega_{ce}) = \exp(-b_e)\left[I_0(b_e) + 2\sum_{m=1}^{\infty} \frac{\omega_e^2 I_m(b_e)}{\omega_e^2 - m^2\omega_{ce}^2}\right] \tag{2.17}$$

Here, $\omega_{ce} = eB_0/m_e$ is the electron cyclotron frequency, $b_e = k^2\rho_{e0}^2$ with $\rho_{e0} = c_{e0}/\omega_{ce}$ being the electron Larmor radius, $\omega_e = \omega - k_y u_{ye0}$ is the electron Doppler-shifted frequency and I_m are the modified Bessel functions of the first kind. Taking a closer look at Equation 2.17, whenever $\omega_e = m\,\omega_{ce}$, $g \to \infty$, which means that the perturbed electron density has resonances at the electron cyclotron frequency and its harmonics.

For the ion density, Equation 2.14 is used. This can be expressed in terms of the ion Doppler-shifted frequency $\omega_i = \omega - k_z u_{zi0}$ and the ion sound speed $c_{s0} = \sqrt{T_{e0}/m_i}$ [6]:

$$\frac{n_{i1}}{n_0} = \frac{k^2 c_{s0}^2}{\omega_i^2} \frac{e\,\phi}{T_{e0}} \tag{2.18}$$

Introducing Equations 2.16 and 2.18 into the Poisson equation gives the following two-dimensional dispersion relation [6]:

$$1 + k^2 \lambda_{D0}^2 = \frac{k^2 c_{s0}^2}{\omega_i^2} + g(\omega_e, b_e; \omega_{ce}) \tag{2.19}$$

where $\lambda_{D0} = \sqrt{\epsilon_0 T_{e0}/(n_0 e^2)}$ is the Debye length, which is the characteristic length beyond which the plasma cancels out the electric field of a single particle. This quantity can also be expressed in terms of the electron plasma frequency $\omega_{pe0} = \sqrt{n_0 e^2/(\epsilon_0 m_e)}$, which is the frequency at which electrons oscillate when displaced from their equilibrium position, so that $\lambda_{D0} = \sqrt{T_{e0}/(m_e \omega_{pe0}^2)}$. Similarly to this quantity, the ion plasma frequency $\omega_{pi0} = \sqrt{n_0 e^2/(\epsilon_0 m_i)}$ is the frequency at which the ions oscillate about their equilibrium position.

Equation 2.19 can now be solved using complex frequencies such that $\omega = \omega_r + i\gamma$. Note that by using complex frequencies, the result can be divided into the real frequency ω_r, and the imaginary part, the growth rate of the instability γ[3]. Solving yields the following three different pairs of modes [6]:

- A pair of ion-acoustic modes with $g \ll k^2 c_{s0}^2/\omega_i$ and real-valued frequencies $\omega_i = \pm\omega_{IA}$ where

$$\omega_{IA} = \frac{k c_{s0}}{\sqrt{1 + k^2 \lambda_{D0}^2}}$$

- When $g \gg k^2 c_{s0}^2/\omega_i$, the frequencies with real values are close to the resonances $\omega_e = m\omega_{ce}$. These are called Electron Bernstein Waves, which are electrostatic waves propagating perpendicular to the magnetic field at harmonics of the cyclotron frequency.

- When $g \sim k^2 c_{s0}^2/\omega_i$, there is a coupling between the Bernstein waves and the ion acoustic modes, resulting in the Modified Ion Acoustic (MIA), whose frequency is:

$$\omega_i = \pm \frac{k c_{s0}}{\sqrt{1 + k^2 \lambda_{D0}^2 - g(\omega_e)}}$$

[3] Substituting into the time-dependent part of the perturbation equation (Equation 2.11) with a complex frequency gives: $\exp(-i\omega t) = \exp(-i\omega_r t)\exp(\gamma t)$. From this expression it can be clearly seen that ω_r is the frequency of the oscillation, whilst γ determines if the oscillations grow or decrease. When $\gamma < 0$, the oscillations get attenuated, but when $\gamma > 0$ these increase in magnitude.

The previously described ECDI is produced when the MIA mode becomes unstable, i.e. $g > 1 + k^2\lambda_{D0}^2$. Due to the fact that g changes from $\pm\infty$ when it crosses the resonance $\omega_e = m\omega_{ce}$, the MIA mode becomes unstable when $\omega_e = (m\,\omega_{ce})^+$ and becomes stable before reaching the next resonance $(m + 1)$ [6].

In terms of the growth rate γ, as seen in the work by Bello-Benítez et al. [6] (or Figure 4.4) the growth of the instability is concentrated near the resonance frequencies $\omega_e = m\omega_{ce}$ forming well-localized peaks of narrow bandwidth. Recalling that $\omega_e = \omega - k_y u_{ye0}$ and applying that, for a purely azimuthal ECDI, the real frequency is negligible with respect to the Doppler term ($|\omega| \ll k_y u_{ye0}$ [6]), the resonance condition becomes $k_y u_{ye0} \approx m\omega_{ce}$, so that the previously described peaks are located at the wavenumbers:

$$k_m \approx \frac{m\,\omega_{ce}}{u_{ye0}}, \qquad m = 1, 2, 3, \ldots$$

As a result, the real frequencies follow the linear approximation $\omega \approx k_y u_{ye0}$ [6].

As shown in previous studies [7], [8], the source of energy for this instability comes from the relative drift velocity between ions and electrons, rather than density or magnetic field gradients, which were shown to have no involvement. Although the conditions for the development are known, its evolution is not fully understood due to its nonlinear couplings. When given the conditions, ECDI grows until it reaches saturation due to nonlinear couplings balancing the exponential growth rate. As a result, oscillations differ from what is predicted by linear theory.

3. SIGNAL PROCESSING - FOURIER & WAVELET ANALYSIS

3.1. Fourier Analysis

Before trying to understand how the wavelet transform and bi-coherence work, it is required to review the contents of Fourier analysis as they are the basis for these tools.

In the year 1822 *La Théorie Analytique de la Chaleur* was published as a memoir by the physicist and mathematician Jean Baptiste Joseph Fourier [41]. In his book, Fourier proposed a way to extract practical information from differential equations with the simple but powerful idea that any periodic function can be represented by a series of sines and cosines. This new way of representing functions changed the mathematical world forever.

This type of representation is typically known as *Fourier Series*. In a more mathematical way, this means that given a periodic function x with period 2π, it can be represented with a trigonometric series, such that [42]:

$$x(t) = \frac{a_0}{2} + \sum_{n=1}^{\infty} a_n \cdot \cos(n\,t) + b_n \cdot \sin(n\,t) \tag{3.1}$$

where the coefficients a_0, a_n and b_n are obtained by taking advantage of the orthogonality of functions. In a similar way to vectors, two functions are orthogonal if they balance out perfectly to zero over a given interval, i.e. given two nonzero functions $x(t)$ and $g(t)$, they are said to be orthogonal in the interval $a \leq t \leq b$, if [42]:

$$\langle x, g \rangle = \int_a^b x(t) \cdot g(t)\, dt = 0$$

This property of functions can be extrapolated for sines and cosines, which yields the following [42]:

$$\int_{-\pi}^{\pi} \sin(n\,t) \cdot \sin(m\,t)\, dt = \begin{cases} \pi & \text{if } n = m, \\ 0 & \text{if } n \neq m. \end{cases}$$

$$\int_{-\pi}^{\pi} \cos(n\,t) \cdot \cos(m\,t)\, dt = \begin{cases} \pi & \text{if } n = m, \\ 0 & \text{if } n \neq m. \end{cases}$$

Multiplying Equation 3.1 by either $\sin(m\,t)$ or $\cos(m\,t)$ and then integrating over the interval $[-\pi, \pi]$, the values of a_0, a_n and b_n can be obtained [42]:

$$a_0 = \frac{1}{\pi} \int_{-\pi}^{\pi} x(t)\, dt$$

$$a_n = \frac{1}{\pi}\int_{-\pi}^{\pi} x(t)\cdot\cos(n\,t)\,dt, \qquad n = 1,\ 2,\ 3,\ \ldots$$

$$b_n = \frac{1}{\pi}\int_{-\pi}^{\pi} x(t)\cdot\sin(n\,t)\,dt, \qquad n = 0,\ 1,\ 2,\ \ldots$$

Sometimes it is desirable to adapt the Fourier series to periodic functions with period $p = 2L > 0$ in the interval $[-L, L]$. If one performs a change of variable such that $t/x = L/\pi$ it can be demonstrated that [42]:

$$x(t) \sim \frac{a_0}{2} + \sum_{n=1}^{\infty} a_n \cos\left(\frac{\pi\,n\,t}{L}\right) + b_n \sin\left(\frac{\pi\,n\,t}{L}\right)$$

As these types of series are expressed in terms of sines and cosines, it is sometimes interesting to take advantage of Euler's formula ($\exp(ix) = \cos(x) + i\ \sin(x)$) and express the Fourier series in complex form. This is achieved by taking $c_0 = a_0/2$, $c_n = (a_n - ib_n)/2$ and $c_{-n} = (a_n + ib_n)/2$, where c_{-n} is the coefficient of the complex Fourier series when n is smaller than 0. As a whole, it is expressed as follows [42]:

$$x(t) = \sum_{n=-\infty}^{\infty} c_n \cdot \exp\left(\frac{i\,\pi\,n\,t}{L}\right)$$

$$c_n = \frac{1}{2L}\int_{-L}^{L} x(t)\cdot\exp\left(-\frac{i\,\pi\,n\,t}{L}\right)dt, \qquad n = 0, \pm 1, \pm 2, \ldots$$

3.1.1. Fourier Transform

Fourier's hypothesis revealed a tool able to simplify complex differential equations into a set of simpler equations by applying a transformation. This transformation is known as the Fourier transform. This tool works just as a mathematical prism that separates light into colors, but instead transforms a function x, which is defined in the *time domain* (it depends on time), into the function X that is defined in the *frequency domain* [41].

Although the functions x and X might seem completely different, they are two faces of the same coin. On the one hand, the original function displays all the time information while hiding the information of the frequencies. On the other hand, the transform shows the information of the frequencies, while hiding the time information. An easier way to understand this is to think of the function x as the recording of a song. The Fourier transform from the record would tell which notes were played, but it would be impossible to determine when they were played.

This time-frequency relation between the original function and its transform can be easily visualized using *Heisenberg boxes* (See Figure 3.1).

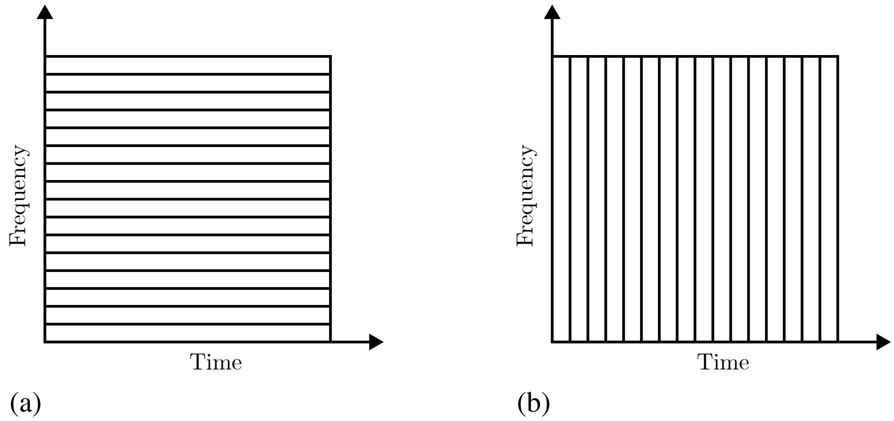

Fig. 3.1. (a) time domain representation using Heisenberg Boxes. The boxes are vertical and narrow in the horizontal direction, as the frequency information is hidden. (b) frequency domain representation. It is the opposite to the time boxes since they stretch in the horizontal direction and are narrow on the vertical one.

In mathematical terms, the Fourier transform of a function $x : \mathbb{R} \to \mathbb{C}$ is defined by [42]:

$$X(\omega) = \mathcal{F}[x(t)](\omega) = \int_{-\infty}^{\infty} x(t) \cdot \exp(-i\,\omega\,t)\,dt$$

for all $\omega \in \mathbb{R}$ where the improper integral converges. This operation can be reversed to obtain the original signal, using what is called as inverse Fourier transform, which is expressed as follows [42]:

$$x(t) = \frac{1}{2\pi} \int_{-\infty}^{\infty} X(\omega) \cdot \exp(i\,\omega\,t)\,d\omega$$

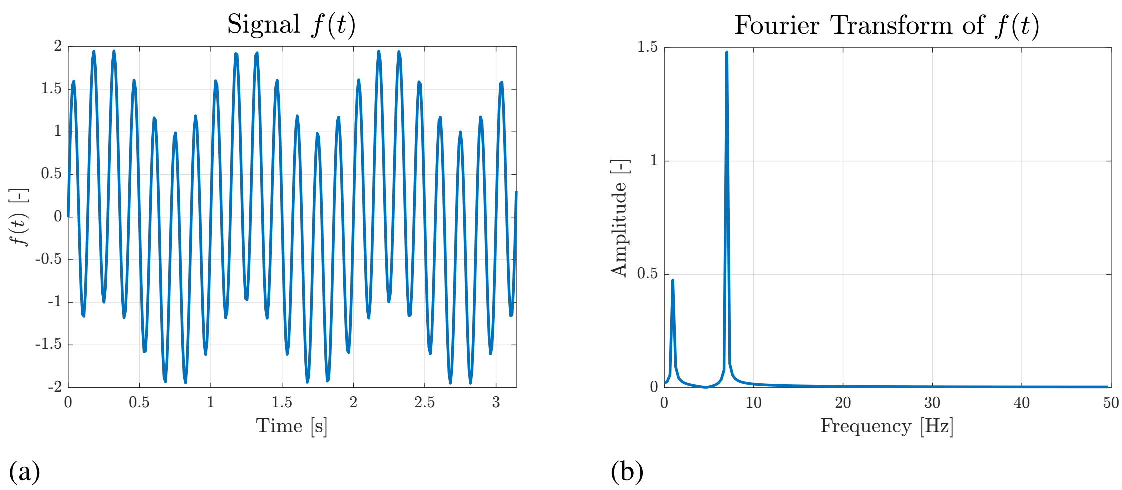

Fig. 3.2. (a) time representation of the function $x(t) = 0.5 \cdot \sin(2\pi\,t) + 1.5 \cdot \sin(7 \cdot 2\pi\,t)$. (b) Fourier transform of the signal $x(t)$. The transform presents two maxima at points $(1, 0.5)$ and $(7, 1.5)$ which coincide with both the amplitude and the frequency from each of the sines used to construct the signal.

3.1.2. Discrete Fourier Series And Transform

In the previous part, the existence of Fourier transform and its inverse in the continuous form was discussed. However, these tools are not valid for the analysis and processing of information with the use of digital devices, as they work with discrete data. For this reason, the discrete version of both the Fourier and the inverse Fourier series are typically used.

Then, given a continuous signal $x(t)$, the N samples taken from this function are defined as $x[n] = x(n\,\Delta t)$, where Δt is the time step for signal sampling and $n = 0,\ 1,\ 2,\ \ldots N-1$. Thus, the Discrete Fourier Transform (DFT) is given by [43]:

$$X[\zeta] = X(\zeta\,\Delta f) = \frac{1}{N}\sum_{n=0}^{N-1} x[n]\cdot\exp\left(-i\,2\pi\,\frac{n}{N}\,\zeta\right) \qquad \forall\zeta,\ where\ x[n]\in\mathbb{C}$$

where $\Delta f = 1/(N\,\Delta t)$ is the resolvable frequency. On the other hand, the discrete inverse Fourier transform of x is obtained in the same way as its continuous analog [43].

$$x[n] = \sum_{\zeta=0}^{N-1} X[\zeta]\cdot\exp\left(i\,2\pi\,\frac{n}{N}\,\zeta\right)$$

3.1.3. Short-Time Fourier Transform

When working with the Fourier Transform, there is a subtle, but very important assumption that is being made. This type of analysis assumes that the function or signal that is being analyzed is static. This does not mean that the value of x does not change in time, but rather that its spectral content (the frequencies that compose the signal) does not change in time. This assumption might be valid in some cases, but the truth is that in the real world almost all signals vary in time. Returning to the example of a song, musical compositions are usually formed by a set of notes played at a determinate time. The sounds produced by different notes are produced by a change in pitch, i.e. they are produced by a change in frequencies. As a result, the recorded signal would be made up of different frequencies that change with each playing note.

As seen before, the Fourier transform is only capable of giving a frequency representation of the signal, hiding all temporal information associated with it. Following this musical analogy, this means that this representation makes it very difficult to determine which notes (frequencies) were playing at a given instant. In order to solve this problem, a trade-off between time and frequency resolution can be done to have something in between. In the mid-twentieth century, the physicist Dennis Gabor proposed to study signals sequence by sequence with the use of windowing functions [44]. In comparison to a normal Fourier transform which compares the whole signal to sines and cosines, this method, called Short-Time Fourier Transform (STFT) or Windowed Fourier Transform, does it on small bits of the original signal, and when it is done it "slides" the window to compare another segment, until the whole signal has been analyzed [44].

The Gabor Transform, a special case of the STFT, changes the Fourier kernel from $\exp(i\omega t)$ to $g_{t,\omega}(s) = g(s-t)\cdot\exp(i\omega s)$. So, the transform is defined as [45]:

$$G[x](t,\,\omega) = \int_{-\infty}^{\infty} x(s)\cdot\bar{g}(s-t)\cdot\exp(-i\omega s)\,ds = \langle x, g_{t,\omega}\rangle \tag{3.2}$$

where $\bar{g}$ is the complex conjugate of the windowing function. As it can be seen in Equation 3.2, the transform function now becomes dependent on both time and frequency, rather than just frequency. Equation 3.2 can be used to define an energy density, commonly referred to as spectrogram [46]:

$$S_x(t,\,\omega) = |G[x](t,\,\omega)|^2$$

This method is far from perfect because, as described before, it offers a trade-off between time and frequency due to the principle of uncertainty, which states that we cannot know which frequencies exist at which time instance. But, it can know what frequency bands exist at what time intervals [44]:

$$\Delta t\cdot\Delta f \geq \frac{1}{4\pi} \tag{3.3}$$

However, the resolution for each frequency band would be influenced by the size of the window that is being used. Narrow windows would improve time resolution while reducing frequency resolution. On the other hand, wide windows would have poor time resolution while having good frequency resolution [45].

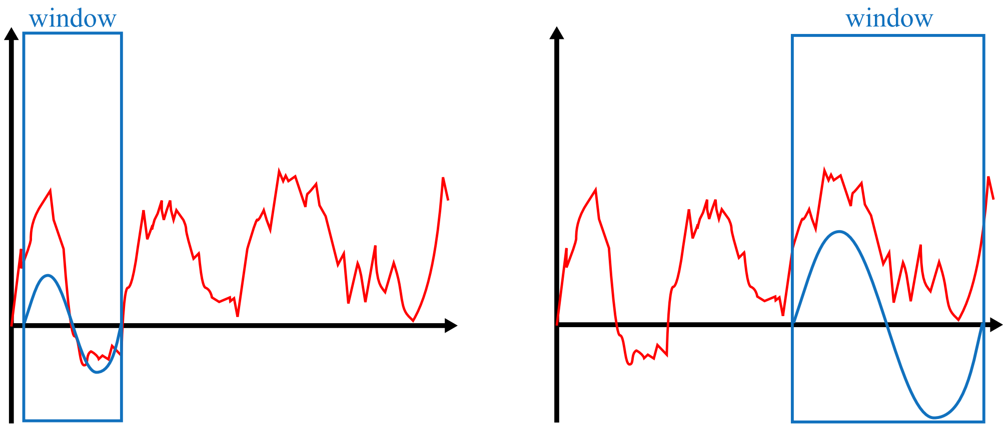

(a) (b)

Fig. 3.3. (a) Narrow window over a signal. These types of windows increase time resolution which is better for high frequency components as they last very short times. (b) Wide window over a signal. These types of windows are better for low frequency components as they last long periods of time and thus, demand high frequency resolution.

3.2. Wavelet Analysis

Around the year 1975, the geophysicist Jean Morlet proposed another way to address the time-frequency analysis problem [41]. The main drawback with STFT is that it tries to fit different signals inside the window, and thus the resolution directly affects its size. However, Morlet did just the opposite, he kept the number of oscillations constant in the window, but he would deform it. So when the window is stretched it reduces the frequency, and when compressed it produces an increase in frequency. As a result, it allows for multiple resolutions at once, thus giving rise to multi-resolution analysis. Just as Amara Graps states in her article *An Introduction to Wavelets* [47]: "The result in wavelet analysis is to see both the forest and the trees, so to speak.".

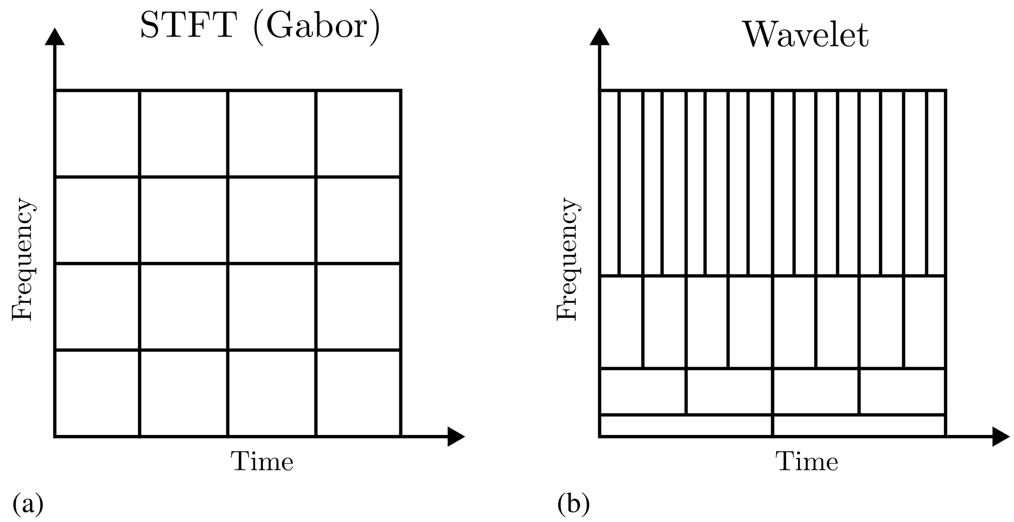

Fig. 3.4. (a) for the Gabor transform every box is equal, affecting the resolution at multiple scales. (b) for wavelet analysis the size of the boxes adapt to the different frequencies optimizing the resolution at each frequency band (narrow for high frequencies and wide for the lower ones).

These deforming windows are known as *wavelets*. The word wavelet is a calque from the French word *"ondelette"* which means little wave [41]. These waveforms come in different forms and shapes that form wavelet families (Morlet, Haar, Daubechies...). Each of the wavelet families is formed by the *mother* or *basic* wavelet, and its children, which are its deformed versions [44]. In order for a function to be considered a mother wavelet it must fulfill the admissibility condition, which is defined as [48]:

$$C_\psi = \int_{-\infty}^{\infty} \frac{|\Psi(\omega)|^2}{|\omega|} d\omega < \infty$$

where $\Psi(\omega)$ is the Fourier transform of the basic wavelet $\psi(t)$ and C_ψ is the wavelet admissible constant. Then, relative to each mother wavelet the Continuous Wavelet Transform (CWT) is defined as [48]:

$$W_\psi[x](b,a) = \frac{1}{\sqrt{|a|}} \int_{-\infty}^{\infty} x(t) \cdot \bar{\psi}\left(\frac{t-b}{a}\right) dt, \qquad a, b \in \mathbb{R} \text{ with } a \neq 0 \tag{3.4}$$

where b indicates the time shift and a, usually called the scale parameter, controls the wavelet scale. W_ψ represents the wavelet coefficients, which have a higher value the closer the frequency of the wavelet is to that of the signal. By setting [48]:

$$\psi_{b,a}(t) = \frac{1}{\sqrt{|a|}} \psi\left(\frac{t-b}{a}\right)$$

Equation 3.4 can be simplified to [48]:

$$W_\psi[x](b,a) = \langle x, \psi_{b,a} \rangle$$

This transform can also be reverted to reconstruct any finite-energy signal from its wavelet coefficients in the following way [48]:

$$x(t) = \frac{2}{C_\psi} \int_0^{\infty} \left[\int_{-\infty}^{\infty} [W_\psi[x](b,a)] \cdot \psi_{b,a}(t)\, db \right] \frac{da}{a^2} \tag{3.5}$$

Note that the integral over a is only defined in the interval $[0, \infty]$. This is because in signal processing only positive frequencies are considered. Equation 3.5 also shows that the function is now not formed by trigonometric functions but with wavelets.

Just as in Fourier analysis, there exist both continuous and discrete versions of the wavelet transform. The *Discrete* or *Dyadic Wavelet Transform (DWT)* is defined as [44]:

$$D[x](k2^j, 2^j) = \frac{1}{\sqrt{2^j}} \int_{-\infty}^{\infty} x(t) \cdot \bar{\psi}\left(\frac{t-k2^j}{2^j}\right) dt \tag{3.6}$$

Here, the difference between the CWT and DWT does not rest on whether the data analyzed is continuous or discrete, but rather on how they decompose the signal. On the one hand, the DWT (Equation 3.6), uses scale factors of the power of two ($a = 2^j$, $b = k2^j, \quad j,k \in \mathbb{Z}$). This change allows for a more efficient and non-redundant representation of the data. On the other hand, CWT allows a to be any real value except zero, which creates redundancy on the coefficients and helps better visualize the information by increasing the resolution, at the only cost of computational horsepower [44]. To highlight the difference between both transforms, Figure 3.9 compares the CWT and DWT representations of a hyperbolic chirp.

The discrete version of the CWT that was just mentioned is described by the following expression [49]:

$$W_x[n,a] = \frac{1}{\sqrt{|a|}} \sum_{n'=0}^{N-1} x[n']\, \bar{\psi}\left(\frac{(n'-n)\,\delta t}{a}\right)$$

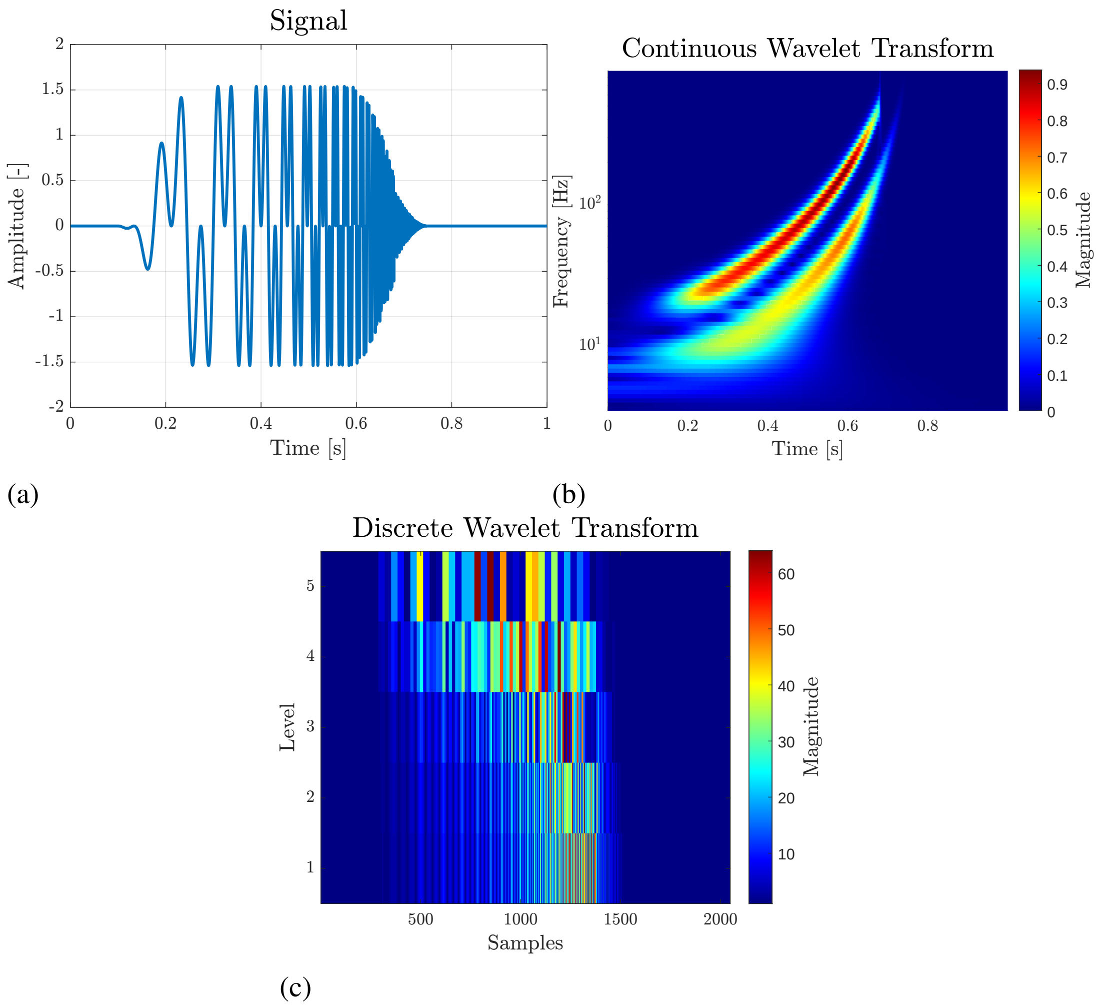

Fig. 3.5. (a) signal composed of two hyperbolic chirps, one from 0.1 to 0.68 seconds with an instantaneous frequency of $\frac{15\pi}{2\pi(0.8-t)^2}$ and another one from 0.1 to 0.75 with an instantaneous frequency of $\frac{5\pi}{2\pi(0.8-t)^2}$ at time t. (b) Continuous Wavelet Transform of the signal. The two chirps that form the signal can be clearly differentiated. (c) Discrete wavelet transform of the signal. Although the form of the signal can be more or less seen, the chirps cannot be distinguished.

Although the scale parameter a in the above equation is allowed to take any positive real value, at the time of computing this quantity, one must choose a finite set of scales at which the transform will be evaluated. For an orthogonal wavelet basis, this set is fixed by power of two ($a = 2^j, \quad j \in \mathbb{Z}$). However, for a non-orthogonal basis, this constraint does not exist, since they are sampled arbitrarily[4]. Torrence and Compo [49] conveniently suggest expressing the scales as fractional powers of two:

[4]Orthogonal and non-orthogonal wavelets versus CWT and DWT is a common point of confusion in wavelet analysis. The first describes the wavelet family that is being used, and the second describes the transform algorithm. Although both concepts are not equal, they are closely connected: the DWT is the natural environment of orthogonal wavelets, while the CWT is typically employed with non-orthogonal ones. Both can be mixed, but this loses the main advantage of each.

$$a_j = a_0 2^{j \cdot \delta j}, \quad j = 0, 1, \dots, J$$

$$J = \delta j^{-1} \cdot \log_2(N\Delta t / a_0)$$

where a_0 is the smallest resolvable scale, J determines the larger scale, and δj sets the resolution. Usually a_0 is taken so that the equivalent Fourier period satisfies the Nyquist criterion, e.g. $a = 2\Delta t$. Note that MATLAB uses a parameter that is called "Voices per Octave", which is defined as $N_v = 1/\delta j$ [50].

The squared modulus of the wavelet coefficients $|W_x(b,a)|^2$ is called scalogram. This represents a local time-scale energy density that corresponds to the Heisenberg box of each wavelet $\psi_{b,a}$ centered at (b,a)[46]:

$$SC_x(b,a) = |W_x(b,a)|^2$$

For analytic wavelets the scale can be transformed into frequency by using the center frequency (ω_c) of that wavelet: $\omega = \omega_c/a$. In this case, the scalogram is displayed in the time-frequency domain, commonly referred to as the wavelet power spectrogram [46]:

$$S_x^w(b,\omega) = |W_x(b,a)|^2 = |W_x(b,\omega_c/\omega)|^2$$

Note that this is the wavelet counterpart of the regular spectrogram.

Most of the time, the signal of interest has a finite length. Due to the wavelet being slid through the span of the signal, errors are introduced at the beginning and end of the scalogram. One of the typical solutions is to add zeros beyond the edges of the function before performing the transform and then removing them. However, this introduces large discontinuities at the borders and, as the scales are being reduced, the amplitude near the edges lowers as more zeros enter the analysis. As a whole, the Cone Of Influence (COI) is defined as the region of the wavelet spectrum where the edge effects become more significant. When the signal is periodic, there is no need to add zeros, which means that there is no COI [49].

3.3. Power Spectrum

3.3.1. Power Spectral Density

When studying a signal, it is usually of interest to determine how the total energy or power is distributed along the spectrum. In signal processing, energy and power classifications are mutually exclusive. This is because a power signal has infinite energy, while an energy signal has zero average power. Energy signals are usually those which are finite and well-localized, i.e. signals which are non-periodic and deterministic. In this sense, a discrete-time deterministic signal $y[n]$ has finite energy if [51]:

$$\sum_{n=-\infty}^{\infty} |y[n]|^2 < \infty$$

For such signals, the energy distribution is described by the Energy Spectral Density (ESD), which is given by [51]:

$$E_y[\zeta] = |Y[\zeta]|^2$$

where $Y[\zeta]$ is the DFT of the signal $y[n]$. However, most real-world signals (especially those in complex systems) do not fall into this category. Their future values cannot be precisely known because their behavior is either random or stochastic and, thus, it is only possible to make probabilistic statements about the future variation of the signal. To describe this behavior, one can see the signal as a random sequence which consists of a set of possible occurrences, each with its own probability of happening. When an observer analyzes one of these realizations, one might be tempted to treat it as a deterministic phenomenon, since one can only visualize one realization at a time. However, this cannot be done since the DFT of a random signal does not converge in the traditional sense because it is not absolutely summable. However, a random signal commonly has finite average power and, as a result, can be described by an average Power Spectral Density (PSD), which is defined as the DFT of the autocorrelation function $R_{xx}[\tau]$ [51]:

$$P_{xx}[\zeta] = \frac{1}{N} \sum_{\tau=0}^{N-1} R_{xx}[\tau] \cdot \exp\left(-i\, 2\pi \, \frac{\tau}{N} \, \zeta\right)$$

where the autocorrelation for a stationary process (a stochastic process whose statistical properties do not change over time) is given by the expectation [51]:

$$R_{xx}[\tau] = \mathrm{E}\{x[n] \cdot \bar{x}[n+\tau]\}$$

In practice, the estimate is obtained from a fine set of N samples. A common approach is to approximate the autocorrelation by averaging the number of samples, which leads to the periodogram estimate [52]:

$$R_{xx}[\tau] \approx \frac{1}{N} \sum_{n=0}^{N-1} x[n] \cdot \bar{x}[n+\tau]$$

Note that using this estimator will result in the following simplification of the PSD [52]:

$$P_{xx}[\zeta] = \frac{1}{N}|X[\zeta]|^2$$

To check whether this particular estimate is a good estimator, the mean and variance of the PSD can be studied. By doing so, one can prove that, as $N \rightarrow \infty$, the mean becomes unbiased. However, the variance behaves as the square of the power spectrum of the signal, proving that it is not a consistent estimator. To fix this one can rely on Welch's Method, which reduces the variance by averaging over multiple realizations of the signal [52]:

$$P_{xx}[\zeta] = \langle |X[\zeta]|^2 \rangle_{ens}$$

To perform this average, the signal length N is divided into K overlapping segments of length N_K. Each segment is then multiplied by a window function $w[n]$ to reduce spectral leakage, so that: [52]

$$x_w[n] = x[rR + n]\, w[n], \qquad n = 0, 1, \ldots, N_K - 1, \quad r = 0, 1, \ldots, K - 1$$

This method offers a trade-off between bias and variance such that neither of both values can be minimized at the same time. The relationship between the total samples N, number of segments K, the shift N_{shift}, and the length of the segments N_K is given by the following expression [52]:

$$N \geq (K - 1) \cdot N_{shift} + N_K$$

In the case where there is no overlap between the windows ($N_{shift} = N_K$), the latter expression becomes $K \cdot N_K \leq N$, so that if K increases, N_K must be reduced, and vice versa. This will have a direct impact on the statistical properties of the PSD since the number of segments gives the factor of variance reduction and segment length determines the bias. However, windows can be overlapped ($N_{shift} < N_K$) allowing both K and N_K to increase, but reducing the independence of segments, which increases the effect of the window choice. [52]

3.3.2. Higher-Order Spectral Analysis

As discussed in Chapter 2.2.1, ECDI is a highly nonlinear phenomenon that is prone to occur in HETs. This means that the interaction between different modes is not only additive, but also multiplicative and resonant. To describe this nonlinear coupling between modes, apart from the power distribution, it is also required to know what the phase relation is between the different components. Thus, it is rather necessary to expand the framework into HOS analysis.

The description of any stochastic process starts with the definition of its statistical moments. For a stationary discrete random process $x[n]$, the moments of order r are given by [53]:

$$m_x^r[\tau_1, \tau_2, \ldots, \tau_{r-1}] = \mathrm{E}\{x[n] \cdot x[n+\tau_1] \cdots \bar{x}[n+\tau_{r-1}]\}$$

From this definition, the correlation functions of higher order for a complex-valued random process are obtained as [54]:

$$\begin{array}{ll} \text{Mean:} & m_x^1 = \mu_x = \mathrm{E}\{x[n]\} \\ \text{Correlation:} & m_x^2 = R_{xx}[\tau_1] = \mathrm{E}\{x[n] \cdot \bar{x}[n+\tau_1]\} \\ \text{Bi-correlation:} & m_x^3 = R_{xxx}[\tau_1, \tau_2] = \mathrm{E}\{x[n] \cdot x[n+\tau_1] \cdot \bar{x}[n+\tau_2]\} \end{array}$$

It is now convenient to introduce cumulants, which measure the extent of non-normality and statistical dependence of random variables [55]. The r^{th} order cumulants are functions of the moments of order up to r. For example [53]:

$$\begin{aligned}
1^{\text{st}} \text{ Order:}\quad & c_x^1 = m_x^1 = \mathrm{E}\{x[n]\} \\
2^{\text{nd}} \text{ Order:}\quad & c_x^2[\tau_1] = m_x^2[\tau_1] - (m_x^1)^2 \\
3^{\text{rd}} \text{ Order:}\quad & c_x^3[\tau_1, \tau_2] = m_x^3[\tau_1, \tau_2] - m_x^1 \cdot \left(m_x^2[\tau_1] + m_x^2[\tau_2] + m_x^2[\tau_2 - \tau_1]\right) + 2 \cdot (m_x^1)^3 \\
4^{\text{th}} \text{ Order:}\quad & c_x^4[\tau_1, \tau_2, \tau_3] = m_x^4[\tau_1, \tau_2, \tau_3] - m_x^2[\tau_1] \cdot m_x^2[\tau_3 - \tau_2] - m_x^2[\tau_2] \cdot m_x^2[\tau_3 - \tau_1] \\
& \qquad - m_x^2[\tau_3] \cdot m_x^2[\tau_2 - \tau_1] \\
& \qquad - m_x^1 \cdot \left(m_x^3[\tau_2 - \tau_1, \tau_3 - \tau_1] + m_x^3[\tau_2, \tau_3] + m_x^3[\tau_1, \tau_3] + m_x^3[\tau_1, \tau_2]\right) \\
& \qquad + (m_x^1)^2 \cdot \left(m_x^2[\tau_1] + m_x^2[\tau_2] + m_x^2[\tau_3] + m_x^2[\tau_3 - \tau_1] + m_x^2[\tau_3 - \tau_2]\right) \\
& \qquad - 6 \cdot (m_x^1)^4
\end{aligned}$$

The most relevant properties of cumulants for the definition of the bispectrum are [53]:

Property 1. If $x[n]$ is Gaussian, $c_x^r[\tau_1, \tau_2, \ldots, \tau_{r-1}] = 0$ for $r > 2$. This implies that the information describing a Gaussian process is only contained in the first and second-order cumulants.

Property 2. Additivity holds for cumulants. In other words, given a signal $x[n] = x_1[n] + x_2[n]$, where $x_1[n]$ and $x_2[n]$ are two statistically independent processes, then

$$c_x^r[\tau_1, \tau_2, \ldots, \tau_{r-1}] = c_{x_1}^r[\tau_1, \tau_2, \ldots, \tau_{r-1}] + c_{x_2}^r[\tau_1, \tau_2, \ldots, \tau_{r-1}] \tag{3.7}$$

Property 3. If $x[n]$ has zero-mean, then, for $r \leq 3$, $c_x^r[\tau_1, \tau_2, \ldots, \tau_{r-1}] = m_x^r[\tau_1, \tau_2, \ldots, \tau_{r-1}]$.

Note that by using Properties 1 and 2, it can be seen that for a signal $x[n]$ comprised of a Gaussian noise signal $x_1[n]$ and the signal of interest $x_2[n]$, it holds true that for $r > 2$, Equation 3.7 becomes:

$$c_x^r[\tau_1, \tau_2, \ldots, \tau_{r-1}] = c_{x_2}^r[\tau_1, \tau_2, \ldots, \tau_{r-1}]$$

In an analogous way to the PSD, the (self-)bispectrum[5] is defined as the third-order cumulant spectra of the signal[6]. For simplicity, it is mathematically accepted that the random signal has zero-mean, so the bispectrum can be expressed as the Fourier transform of the bi-autocorrelation function [54]:

$$B[\zeta_1, \zeta_2] = \mathrm{E}\{\mathcal{F}[R_{xxx}]\} = \mathrm{E}\{X[\zeta_1] \cdot X[\zeta_2] \cdot \bar{X}[\zeta_1 + \zeta_2]\} \tag{3.8}$$

where ζ_1 and ζ_2 are allowed to take negative values. In reality, most signals do not have a zero-mean. In this case, the mean of the signal is initially computed and then subtracted from itself, so Equation 3.8 can be used [54].

From Equation 3.8 it can be clearly seen that the bispectrum is a measurement of the statistical dependence between three waves. In order for the bispectrum to yield non-zero values, two conditions must be met. The first is that the transform of the signal at ζ_1, ζ_2 and $\zeta_3 = \zeta_1 + \zeta_2$ must not be zero. The second and most important one is that these three spectral components must be correlated. When this is not the case, the expectation process averages the value to zero. It is important to note that Equation 3.8 will return complex values even when the signal is real-valued [54].

In a similar way to coherence, which measures the degree of linear correlation between the spectrum of two signals, bicoherence is used as a way to determine coherence between three waves due to wave coupling. The bicoherence is described mathematically as the normalized version of the bispectrum [55]:

$$b^2[\zeta_1, \zeta_2] = \frac{|B[\zeta_1, \zeta_2]|^2}{\mathrm{E}\{|X[\zeta_1] \cdot X[\zeta_2]|^2\} \cdot \mathrm{E}\{|X[\zeta_1 + \zeta_2]|^2\}} \tag{3.9}$$

where for both the bispectrum and bicoherence, the expected value is obtained by ensemble averaging the signal (using Welch's Method). The values of the bicoherence vary between 0, for noise or random phases, and 1, for phase-coupled modes. For finite-length time series, Equation 3.9 gives non-zero values even for completely independent modes. The expression for a 95% confidence threshold for determining that a signal is not noise is $\epsilon[b^2] = 6/\mathrm{dof}$, where dof refers to the degrees of freedom or the total amount of independent data used for computing the bicoherence. When estimating the data by ensemble

[5] For simplicity, the prefix *self-* is dropped, and the self-bispectrum and self-bicoherence are simply referred to as the bispectrum and bicoherence. Their cross counterparts are defined below.

[6] The PSD can also be seen as the second-order cumulant spectra of the signal.

averaging, the number of degrees of freedom is obtained as dof $= 2M$, where M is the total number of independent realizations [56].

The definitions above correspond to the *self*-bispectrum and *self*-bicoherence, which are used to detect couplings within a single signal. However, when studying this coupling between different signals, the cross-bispectrum and cross-bicoherence are used. In this way, given three signals x, y and z, the cross-bispectrum and cross-bicoherence are given by:

$$B_{xyz}[\zeta_1, \zeta_2] = \mathrm{E}\{X[\zeta_1] \cdot Y[\zeta_2] \cdot \bar{Z}[\zeta_1 + \zeta_2]\} \tag{3.10}$$

$$b^2_{xyz}[\zeta_1, \zeta_2] = \frac{|B_{xyz}[\zeta_1, \zeta_2]|^2}{\mathrm{E}\{|X[\zeta_1] \cdot Y[\zeta_2]|^2\} \cdot \mathrm{E}\{|Z[\zeta_1 + \zeta_2]|^2\}} \tag{3.11}$$

When $x = y = z$, these reduce to the self-versions defined above. Although bispectrum and bicoherence are mathematically computed using discrete indices (ζ_1, ζ_2), for physical interpretation it is common to map these back to their continuous frequencies (ω_1, ω_2).

When two specific modes interact with each other, they appear on the bicoherence plot as isolated "islands" with high value. The width of these islands represents the spectral broadening of the modes, i.e. how much the interacting modes have spread across frequencies. On the other hand, when a single frequency interacts with a continuous band of several frequencies instead of a single point, the interaction extends across the plot. As a result, this creates lines or segments rather than isolated spots. Depending on the direction, these might indicate which frequency is staying constant. For vertical lines, $\omega_1 =$ const., for horizontal lines $\omega_2 =$ const. and for diagonals $\omega_3 =$ const.

When interpreting bicoherence results, it is important to note that a high correlation value does not imply causation via quadratic coupling. In addition, bicoherence cannot determine the direction of power flow through the modes. This means that one cannot determine whether ω_1 and ω_2 activate ω_3 or vice versa [3].

It also has to be noted that it is not necessary to draw the whole ω_1-ω_2 plane when representing the results, since some simplifications can be made [57]:

- Both ω_1, ω_2, and $\omega_3 = \omega_1 + \omega_2$ must be smaller than the Nyquist frequency: $\omega_N = \omega_{samp}/2$, where ω_{samp} is the sampling frequency of the signal.
- Because ω_1 and ω_2 are interchangeable, the plot might be restricted to $\omega_1 \geq \omega_2$
- The case (ω_1, ω_2) is identical to the case $(-\omega_1, -\omega_2)$ when the signal is real-valued.

A visual representation of the bicoherence and bispectrum can be used to better understand this tool. The condition for quadratic coupling requires the interacting modes to satisfy the frequency sum rule. In the discrete computational domain, this corresponds to matching indices, which maps to continuous frequencies as follows [58]:

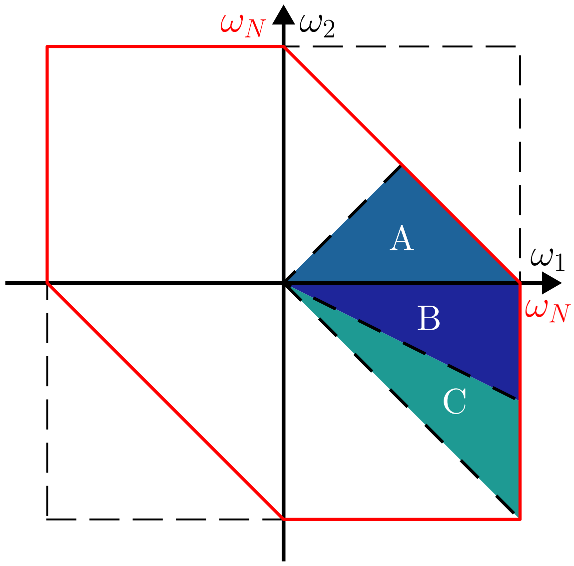

Fig. 3.6. Bicoherence domain for a finite-length signal. Note that the bicoherence is bounded by the Nyquist frequency, represented by the solid red line. Regions A, B and C correspond to the final calculation areas remaining after applying the previously described symmetries.

$$\zeta_3 = \zeta_1 + \zeta_2 \implies \omega_3 = \omega_1 + \omega_2$$
$$\theta_3 = \theta_1 + \theta_2$$

where ω_i (for $i = 1, 2, 3$) is the frequency and θ_i is the phase of the Fourier components of the signal. Here, nonlinear coupling occurs between ω_1 and ω_2, which generate a third wave at the sum frequency ω_3.

The process of obtaining the bispectrum (Equation 3.8) can be visualized in a complex plane, which is represented in Figure 3.7. When there is a coupling between the components, the value of the bispectrum will be high. On the other hand, when the components do not have a coupling or the portion analyzed is noise, the value will tend to zero as the number of averages increases.

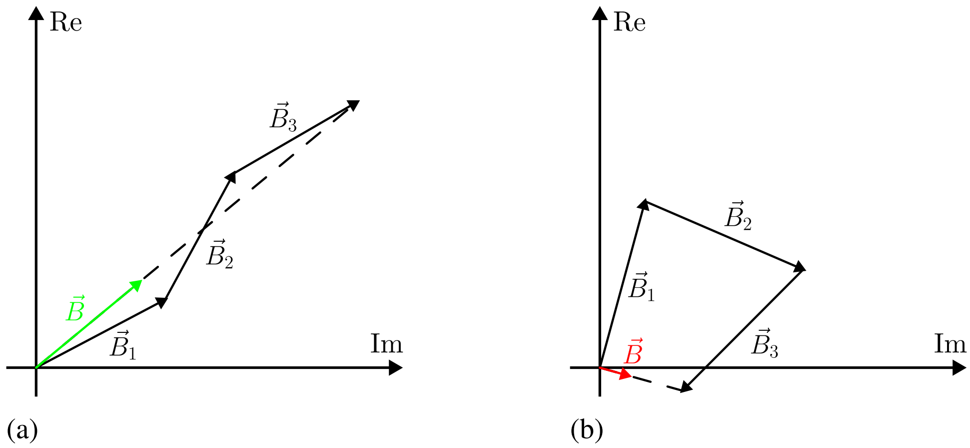

Fig. 3.7. Visual representation of bispectrum for a stationary signal for given (ω_1, ω_2) components. (a) If both frequencies are coupled, the phase relation with the third one will be kept constant over time. As a result, the bispectrum of the multiple realizations $\vec{B}_1$, $\vec{B}_2$, and $\vec{B}_3$, will align and the resulting averaged complex vector $\vec{B}$ will have a large magnitude. (b) When the components are decoupled, the steps will be given in random directions, and thus the average value will be small.

One of the key underlying assumptions of bicoherence is that it assumes that the spectrum is stationary, i.e. the spectral properties of the signal do not vary with time. Going back to the visualization of Figure 3.7, when a non-stationary signal is considered, the "steps" given by each of the realizations may vary. This introduces a high bias to the bicoherence values, which might indicate high values, even when there is no phase coupling between the modes (Figure 3.8) [58].

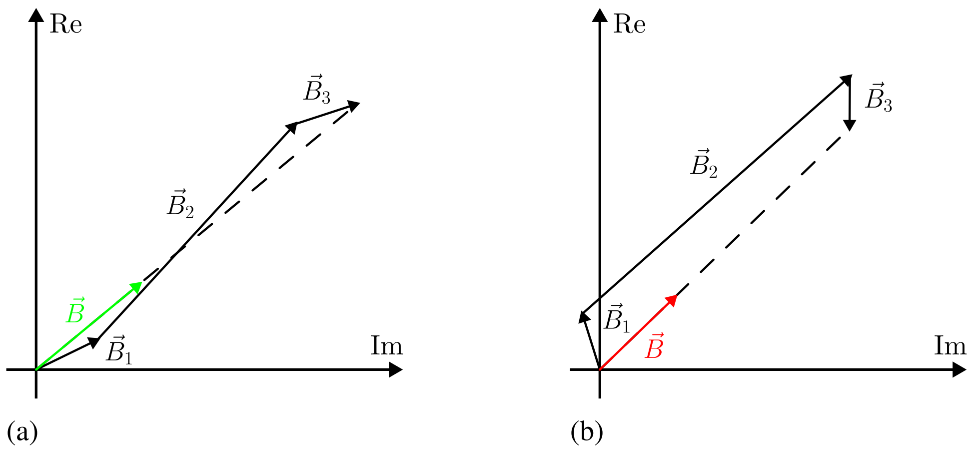

Fig. 3.8. Visual representation of bispectrum for a non-stationary signal for given (ω_1, ω_2) components. (a) When both frequencies are coupled the average complex vector will have a large magnitude. (b) Even if the phases are random, when the signal is non-stationary it might result large values of bispectrum, leading to false positives.

In continuous form, the PSD of the signal is given by:

$$P_{xx}(\omega) = \mathrm{E}\{|X(\omega)|^2\}$$

Additionally, the bispectrum and bicoherence expressed in continuous form are:

$$B(\omega_1, \omega_2) = \mathrm{E}\{X(\omega_1) \cdot X(\omega_2) \cdot \bar{X}(\omega_1 + \omega_2)\}$$

$$b^2(\omega_1, \omega_2) = \frac{|B(\omega_1, \omega_2)|^2}{\mathrm{E}\{|X(\omega_1) \cdot X(\omega_2)|^2\} \cdot \mathrm{E}\{|X(\omega_1 + \omega_2)|^2\}}$$

3.3.3. Wavelet Power Spectrum

Just as any of the other tools for Fourier analysis that were discussed, both the power spectra and the bicoherence have a wavelet counterpart. The way of obtaining these is analogous to their Fourier version.

To simplify the notation and highlight the physical meaning of the parameters in HOS analysis, the CWT coefficients defined in Equation 3.4 will be denoted as $W_x(t, a)$. In this notation, the translation parameter b is replaced by the local time variable t, and the integration variable is renamed to τ:

$$W_x(t, a) \equiv W_\psi[x](t, a) = \frac{1}{\sqrt{|a|}} \int_{-\infty}^{\infty} x(\tau) \cdot \bar{\psi}\left(\frac{\tau - t}{a}\right) d\tau \tag{3.12}$$

Starting with the Wavelet Power Spectrum (WPS), it is defined as the time integral of the scalogram [59]:

$$P^w_{xx}(a) = \frac{1}{T} \int_T SC_x(t, a)\, dt = \frac{1}{T} \int_T \bar{W}_x(t, a) \cdot W_x(t, a)\, dt$$

The wavelet bispectrum is given by the third-order wavelet HOS, which is defined as follows [60]:

$$B^w = \mathrm{E}\{W_x(t, a_1) \cdot W_x(t, a_2) \cdot \bar{W}_x(t, a_3)\}$$

where the three scales follow an analogous version of the frequency sum rule: $a_3^{-1} = a_1^{-1} + a_2^{-1}$. Note that depending on the estimator used, the bispectrum will be a function of the scales a_1, a_2 and time t, or just a function of the scales. Similarly as in Fourier HOS analysis, the Wavelet Bicoherence (WB) is described as the normalized version of the bispectrum [60]:

$$[b^w]^2 = \frac{|B^w|^2}{\mathrm{E}\left\{|W_x(t, a_1) \cdot W_x(t, a_2)|^2\right\} \cdot \mathrm{E}\left\{|W_x(t, a_3)|^2\right\}} \tag{3.13}$$

Both the wavelet bispectrum and WB were introduced for the first time by van Milligen et al. [57]. In their study, they averaged the signal over an interval $T : t_1 \leq t \leq t_2$, where the signal is assumed to be stationary, to maintain statistical stability. This interval can be slid over the signal domain to obtain the time resolution of the bicoherence. However, in more modern approaches, like the one described by Gelman et al. [60], the signal is ensemble averaged, so that the time dependence is maintained. This last version of bicoherence is generally referred to as the Instantaneous Wavelet Bicoherence (IWB). In this sense, both forms of the WB are able to detect not only where phase coupling is present, but also when this occurs, unlike the Fourier version which averages out the bicoherence along the length of the signal, so that short bursts of bicoherence might go undetected.

As in the Fourier case (Eqs. 3.10–3.11), these definitions can be extended to analyze three distinct signals by replacing W_x with W_x, W_y and W_z, resulting in the wavelet cross-bispectrum and cross-bicoherence.

An important thing to note is that for any form of the wavelet bicoherence it is no longer assumed that the signal has zero-mean. In Appendix A it is proven that for any constant-valued function, the wavelet transform is equal to zero. So, if one describes x as a function composed of a constant component and a varying component, then by the linearity of the CWT, the wavelet transform of x is equal to the transform of the varying component.

The main difference between the Fourier and Wavelet versions of the bicoherence is the coupling condition. As discussed in the previous section, Fourier bicoherence imposes a strict constraint on the relation between frequencies, such that $\omega_3 = \omega_1 + \omega_2$. However, in the case of wavelets, this relation is expressed in terms of scales. To facilitate the physical interpretation of these scales, these are usually mapped to equivalent frequencies: $\omega_i = \omega_c/a_i$, where ω_c is the center frequency of the wavelet (discussed in the next section). Since a wavelet of scale a has a determinate bandwidth associated with it, WB is not a matter of matching frequencies but a matter of matching wavelets at determinate scales. As a result, the coupling condition is relaxed, and it becomes [57]:

$$\omega_3 = \omega_1 + \omega_2 + \Delta\omega$$

where $\Delta\omega$ corresponds to the frequency mismatch tolerated by the WB, which is set by the wavelet frequency resolution corresponding to the highest frequency of the set $\{\omega_1, \omega_2, \omega_3\}$. Note that this $\Delta\omega$ is larger than the frequency resolution offered by its Fourier counterpart, making the wavelet version a better candidate for studying the bicoherence of signals in real-world systems, where small mismatches might occur due to the randomness of the system [57].

Another of the advantages that the WB has is the nature of its basis functions. As described at the beginning of this chapter, Fourier analysis assumes that the signals can be described in terms of oscillatory functions that span all over the signal, so it looks for modes that last for long times. However, turbulent flow generally does not follow this behavior, as it is formed by transient, short-lived structures that appear, develop, and decay.

On the other hand, the CWT uses wavelets, which are localized oscillatory functions that resemble much better these structures. As a result, WB is better at detecting short-lived structures in turbulent environments than its Fourier counterpart. However, both methods are still limited in the sense that they are still not able to differentiate between structures passing by the observation point and dynamic wave interactions. This issue can only be solved by analyzing data from multiple observation points [57].

In terms of the significance threshold for the averaged WB[7], the 95% confidence floor noise level is given by (Derived in Appendix B):

$$\epsilon\left[[b^w(\omega_1,\omega_2)]^2\right] = D_{0.05} = \tanh^2\left(\frac{1.96}{\sqrt{N_e}}\right) \tag{3.14}$$

where N_e is the effective number of independent data points, which is given by [59]:

$$N_e(\omega_1,\omega_2) = \frac{2\pi \cdot N_T}{\omega_c \cdot \omega_s \cdot \max\left[\frac{\sqrt{\omega_1^2+\omega_2^2}}{\omega_1\omega_2}, \frac{2}{\omega_1+\omega_2}\right]\sqrt{\ln\kappa}} \tag{3.15}$$

where N_T is the number of samples in the time T, ω_s is the sample frequency and κ is a decorrelation factor, whose value is usually between 5 and 20 [61]. This correction of the number of samples is done due to the fact that wavelets change size depending on the frequency, thus the effective number of samples will change along the spectrum. Thus, a bicoherence of 0.1 might be relevant at low frequencies but completely insignificant at high frequencies. To further compare this method with its Fourier counterpart, assume that the WB is being applied to a one-dimensional signal such that $N_T = N$. From Fourier bicoherence, it would be expected that the noise floor is proportional to $1/M$. Moreover, assume that the length of the signal is large enough so that $Z_{\alpha/2}/\sqrt{N_e} \ll 1$, then:

$$\epsilon\left[[b^w(\omega_1,\omega_2)]^2\right]\Big|_{WB} \approx \frac{1.96^2}{N_e} \propto \frac{1}{N_T} = \frac{1}{N}$$

From this relation, it can be clearly seen that the wavelet counterpart does a greater job in reducing the noise in the bicoherence, since the number of samples (N) in the whole signal is greater than the number of samples of the realizations (N_K). Another interpretation of this expression is that the WB requires fewer samples than the Fourier version to obtain the same noise floor, which makes the WB a better candidate when analyzing signals of limited length. As a consequence, it is able to detect phase coupling that the Fourier bicoherence keeps hidden below the noise floor.

Note that when calculating the WB over multiple intervals of length T, it can be seen as applying multiple rectangular windows without overlap. Thus, in an analogous way to the STFT a smoothing window can be applied. It is important to note that when applying

[7]In this context the "averaged" WB, or simply WB will be used to refer to the version proposed by van Milligen et al.

this window, the number of samples N_T used in Equation 3.15 has to be corrected using the Normalized Equivalent Noise Bandwidth (NENBW) [62], [63]:

$$N_T|_w = \frac{\left[\sum\limits_{i=1}^{N_T} w_i\right]^2}{\sum\limits_{i=1}^{N_T} w_i^2} = \frac{N_T}{\text{NENBW}}$$

where $0 \leq w_i \leq 1$ denote the weights of the windowing function. There are a wide variety of windows that can be used to smooth out the bicoherence, but the one used for this specific study was the Hann (or Hanning) window. This is due to the fact that it is well defined in an interval $T_H : -T_H/2 \leq t \leq T_H/2$, it has zero derivative at the edges (smooth edges) and the value of the NENBW is somewhat reasonable with a value of 1.5 [62].

In terms of the IWB, the noise floor is the exact same as the one obtained when using Fourier bicoherence as demonstrated in Appendix C:

$$\epsilon\left[[b^w]^2\right]\Big|_{IWB} = \frac{3}{M}$$

Following the same approach as the WB, the windowed Fourier bicoherence is proposed. In previous sections, it was described how the STFT and the wavelet bicoherence are similar in the sense that both methods use sliding windows. The hypothesis here is that the CWT can be substituted with the STFT to recover temporal information in a way similar to that of wavelet methods. This approach will be tested to see how it compares with its wavelet counterparts. The windowed Fourier bicoherence is expected to have a high noise floor since it follows the same expression as the regular Fourier bicoherence ($\epsilon[b^2] = 6/\text{dof}$) and the number of samples is reduced due to the windows.

3.4. Wavelet Selection

Throughout this chapter, there has been a lot of discussion about the different things that can be done using wavelets, but nothing has been said yet about the specific wavelet that will be used for the analysis.

In wavelet analysis, the selection of the wavelet and its parameters is often an iterative process, which often implies comparing different candidates [64], [65]. Since there is no universal wavelet that can be used for all signals, this process is often seen as arbitrary [49]. Although there is no standard process for choosing one, the set of candidate wavelets can be reduced depending on what we want to do with them. A way of guiding this analysis is by looking at the properties of the wavelet function itself. Some of the most important aspects to take into account when selecting a wavelet are the following:

- **Orthogonal vs non-orthogonal**: as described before, a wavelet can be orthogonal or not depending on whether it is defined on a set of discrete dyadic scales or can be calculated on any scale. Orthogonal wavelets are better for more efficient representations, while non-orthogonal wavelets are better for the interpretation of time series, resulting in smooth and continuous representations of the coefficients [49].

- **Complex vs real**: complex wavelets (Morlet, Paul) display both amplitude and phase of the signal, whereas real wavelets isolate peaks and discontinuities [66].
- **Analytical vs non-analytical**: analytical wavelets are complex wavelets whose Fourier coefficients are zero for negative frequencies. This allows the transform to have a well-defined modulus (energy) and phase, since they avoid interference from negative frequencies [67].
- **Width**: broad wavelets have high frequency resolution and poor time resolution. Narrow wavelets do the opposite. Some wavelets such as the Morlet possess a parameter that allows the modification of the width by changing it [49].
- **Shape**: since the wavelet transform can be seen as the convolution between the signal and the wavelet being employed, it is easy to see that the former acts as a lens through which the signal is observed. As a result, we want this lens to be as close to the true shape of the signal as possible [67].

For the bicoherence to yield reliable results, van Milligen et al. [57] describe the properties that the analyzing wavelet is required to have. From the perspective of wavelet selection, both the WPS and WB have similar requisites. Since the latter is more strict than the former, the same wavelet can be used.

- **The wavelet must have a single, well-localized peak in the Fourier domain**: in order to fulfill the frequency sum rule, the wavelet scales must allow mapping into a single frequency such that $\omega_i = \omega_c / a_i$. When this is not the case the bicoherence becomes ambiguous, since a single scale will be related to multiple frequencies.
- **Wavelet must be analytical**: by definition of bicoherence, the main goal is to check whether there is phase coupling in the signal. If the wavelet coefficients are not complex, then no phase coupling can be detected.
- **Fast and smooth temporal decay**. The effective number of samples N_e and, as a consequence, the significance threshold of the WB are values that depend on ω_c and κ, which themselves depend on how fast the wavelet decays with time. For a low value of the noise level, the wavelet is required to decay fast enough, so that the correlation between close points dies rapidly.
- **Time-frequency resolution should be controlled**: although, not a strict requirement, ideally, the wavelet selected should be able to vary its width based on a set of parameters to allow tuning of the bicoherence so that it better matches the signal. Wavelets with a single parameter which controls the resolution are preferred, since they simplify the analysis.

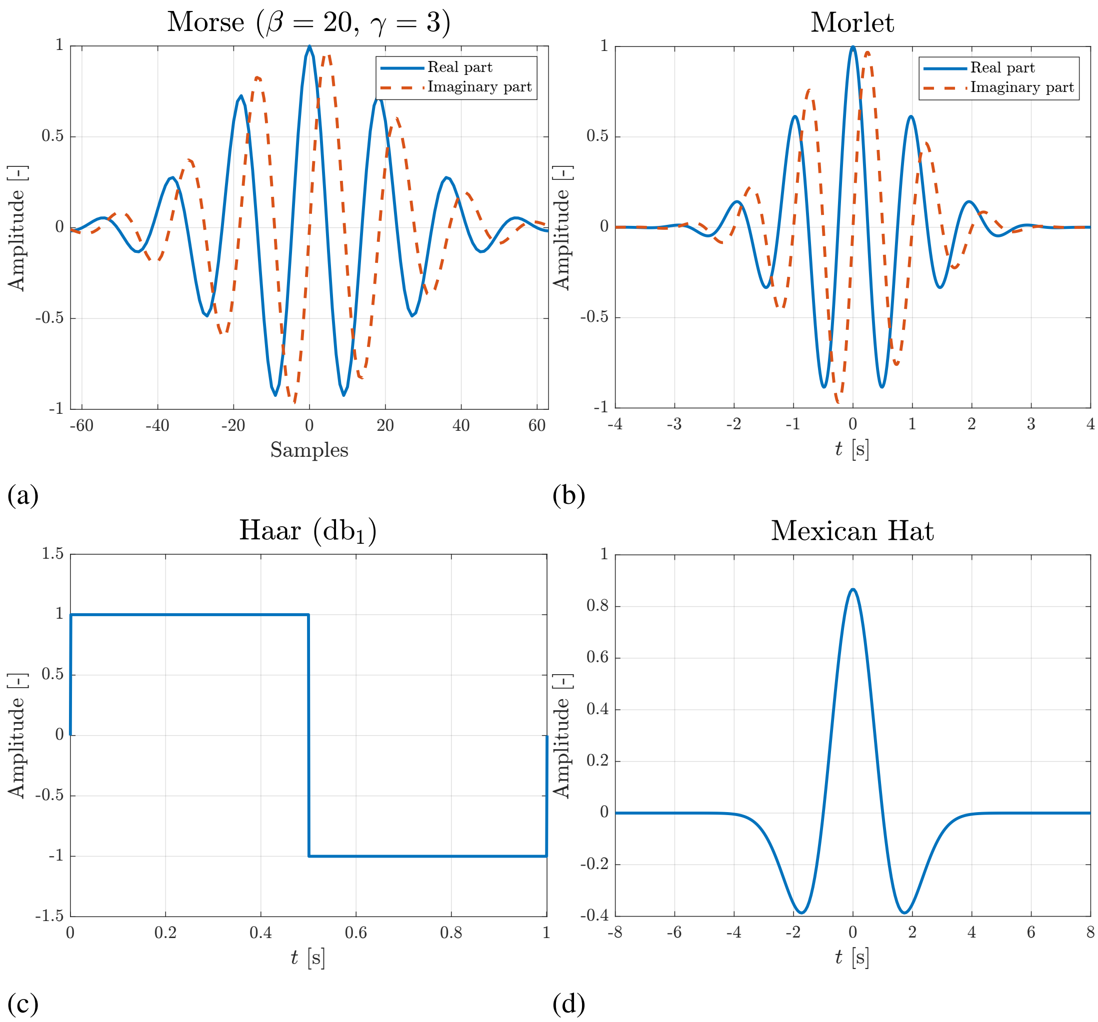

Fig. 3.9. Different wavelets at unit scale ($a = 1$). (a) Morse wavelet: analytic non-orthogonal. (b) Analytic Morlet wavelet: analytic non-orthogonal. (c) Haar wavelet: real, orthogonal. (d) Mexican Hat wavelet: real, non-orthogonal.

- **The wavelet should resemble a wave pulse**: since this work focuses on the analysis of turbulent plasma flows, the wavelet should have a similar shape to that of the short-lived transient structures that one expects to find in these types of flows. As a result, the wavelet should have a well-localized pulse-like shape containing only a few oscillations.

Two wavelet families fit these requirements: the Morse wavelet (or Morse family) and the Analytic Morlet. The first one, the Morse wavelet, is not a specific wavelet, but a family of them. This wavelet is given by the following expression [67]:

$$\Psi_{\beta,\gamma}(\omega) = U(\omega) \cdot a_{\beta,\gamma} \cdot \omega^{\beta} \cdot e^{-\omega^{\gamma}}$$

where $a_{\beta,\gamma}$ is a normalization constant, $U(\omega)$ is the unit step function, and β and γ are two parameters that control the behavior of the wavelet. Here β is used to control the length of the wavelet (time-bandwidth product), whereas γ is used to control the shape, in particular, the symmetry of the frequency response close to the peak.

However, for the sake of simplifying the analysis, in this study the Morlet wavelet is used, since its shape can be controlled by just one parameter. In addition, using a wavelet other than the Morlet will change the expressions for the Probability Distribution Function (PDF) derived by Ge [59], making the previous statistical statements invalid. This wavelet is defined by the following expression [57]:

$$\psi_{b,a}(t) = \frac{1}{\sqrt{a}} \cdot \exp\left[i\frac{2\pi t}{a} - \frac{1}{2}\left(\frac{t}{ad}\right)^2\right] \tag{3.16}$$

where d determines the exponential decay of the wavelet. For this specific form of the Morlet wavelet, the central frequency is $\omega_c = 2\pi$, and the resolution is approximately given by $\Delta\omega = \omega_i/4d = (\omega_c/a_i)/4d$. Consequently, the time resolution is given by the decay of the exponential section of the wavelet $\Delta t = ad$. Note that as the decay increases $d \to \infty$, the wavelet analysis approaches the Fourier analysis asymptotically. Following the same approach as van Milligen et al. [57] a value of $d = 1$ is used, since it provides a reasonable trade-off between time and frequency resolution.

An important remark has to be made concerning the value of the central frequency used in practice. The derivation of the statistical properties described in the previous section assumed a value of $\omega_c = 2\pi$, according to the Morlet wavelet definition presented above. However, the implementation in MATLAB's wavelet toolbox ("amor") uses a value of $\omega_c = 6$. This discrepancy is small enough so that the wavelet shape is almost indistinguishable. As a result, the statistical properties are still applicable for the analysis.

3.5. Multidimensional Signals

The tools presented so far have been written for one-dimensional signals that depend only on time. However, the signals studied in the next chapter depend on both time and space, $x(t, y)$. In this case, the signal is sampled on a grid $x[n_t, n_y] = x(n_t \cdot \Delta t,\ n_y \cdot \Delta y)$, with $n_t = 0, \ldots, N_t - 1$ and $n_y = 0, \ldots, N_y - 1$, where Δy is the spatial step.

Due to the Fourier kernel being separable, it can be applied independently on each of the dimensions. For example, in the case of the DFT, the two-dimensional version is defined as:

$$X[\zeta, \xi] = \frac{1}{N_t N_y} \sum_{n_t=0}^{N_t-1} \sum_{n_y=0}^{N_y-1} x[n_t, n_y] \cdot \exp\left[-i\,2\pi\left(\frac{n_t}{N_t}\zeta + \frac{n_y}{N_y}\xi\right)\right] \tag{3.17}$$

Note that applying the transform to the spatial dimension turns the frequency index into a wavenumber index. In the case of a periodic boundary condition, the relationship between the index and the wavenumbers is given by:

$$k = 2\pi\xi/L_y, \text{ with } \xi = 0, 1, 2, \ldots$$

A consequence of this two-dimensional version of the Fourier transform is that the dimensionality of the power spectrum is also affected. In the case of the PSD it becomes a function of frequency and wavenumber $P(\omega, k)$, whereas the bicoherence and bispectrum become four-dimensional objects such that they depend on two frequencies and two wavenumbers $B(\omega_1, \omega_2, k_1, k_2)$.

These transforms can also be combined, applying a different analysis along each axis. For example, a Fourier transform is applied in the spatial dimension, and a wavelet transform is applied in the temporal dimension.

4. ANALYSIS OF E × B DISCHARGE

4.1. Problem Setup

As advanced in the introduction, the PICASO PIC model will be used for the analysis of an E × B discharge that mirrors the behavior of a plasma in a HET. In order to study the anomalous transport seen in previous work [3], a homogeneous, collisionless plasma will be inspected in the axial-azimuthal domain defined as $[0, L_z]\times[0, L_y]$, where z and y denote the axial and azimuthal directions, respectively. In order to recreate the axisymmetry of the annular channel, a periodic boundary condition is applied to the y boundaries.

The plasma is set to initially be at equilibrium and subject to an out-of-plane magnetic field $\vec{B}_0 = B_0\vec{e}_x$ and an axial electric field $\vec{E}_0 = E_0\vec{e}_z$. The electrons used to populate the simulation are sampled from a drifting Maxwellian Velocity Distribution Function (VDF) with density n_0, temperature T_{e0} and an E × B drift velocity $\vec{u}_{ye0} = u_{ye0}\vec{e}_y = (E_0/B_0)\vec{e}_y$. On the other hand, ions are assumed to be cold ($T_{i0} \approx 0$), have a density n_0 and a constant velocity $\vec{u}_{zi0} = u_{zi0}\vec{e}_z$. These particles are set to move freely across the y boundaries of the simulation. However, particles crossing the z boundaries are removed from the simulation. To account for this, using the same distribution as before, ions are injected at $z = 0$ with flux density n_0u_{zi0}, and electrons are injected at $z = 0$ and $z = L_z$ with thermal fluxes $\pm n_0c_{e0}/\sqrt{2\pi}$, where $c_{e0} = \sqrt{T_{e0}/m_e}$. Note that this refilling of particles is essential to sustain the discharge and to recreate the conditions away from the anode and the cathode. If this condition is turned off, it would cause the formation of sheaths at the edges of the domain provoked by the fleeing electrons, leading to the discharge dying out. Figure 4.1 illustrates the configuration of the simulation.

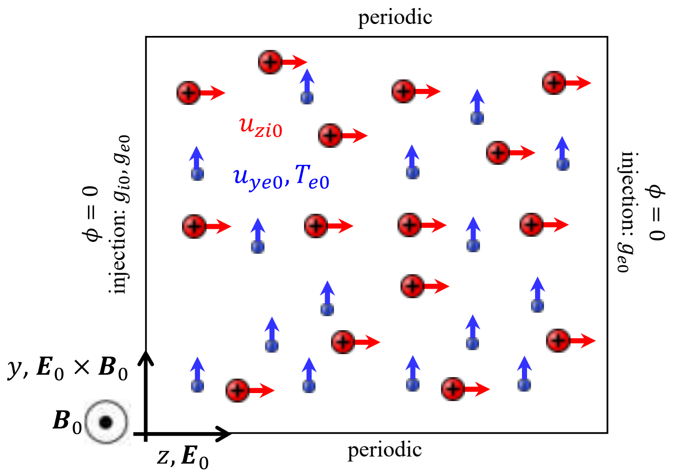

Fig. 4.1. Schematic showing the set up of the simulation: axis, boundary conditions and equilibrium state.

The simulation parameters, which are summarized in Table 4.1, were explicitly chosen so that the plasma would exhibit the instability we want to study. As mentioned in Chapter 3, the development of the ECDI generates a disturbance in the electric field, $\vec{E}_1 = -\vec{\nabla}\phi$, which influences the motion of the particles. The electrostatic potential ϕ is obtained by solving the Poisson equation (Equation 2.2) with periodic boundary conditions at the y edges and Dirichlet conditions at the z borders.

TABLE 4.1. SIMULATION PARAMETERS.

Description	Value
Ion mass, m_i	1 amu
Applied electric field, E_0	10^4 V/m
Applied magnetic field, B_0	200 G
Plasma density, n_0	10^{17} m^{-3}
Ion axial velocity, u_{zi0}	10 km/s
Initial electron temperature, T_{e0}	6 eV
Azimuthal domain length, L_y	5.359 mm
Axial domain length, L_z	2.679 mm
$E_0 \times B_0$ drift, u_{ye0}	500 km/s
Electron thermal speed, c_{e0}	1027 km/s
Ion sound speed, c_{s0}	23.97 km/s
Debye length, λ_{D0}	57.58 μm
Electron Larmor radius, ρ_{e0}	292.0 μm
Electron plasma frequency, ω_{pe0}	2.839 GHz
Electron gyrofrequency, ω_{ce}	0.5600 GHz
Ion plasma frequency, ω_{pi0}	66.26 MHz
Lower-hybrid frequency, ω_{lh}	13.07 MHz
Number of cells in y direction, N_y	100
Number of cells in z direction, N_z	50
Number of particles per cell, N_{ppc}	~ 200
Time step, Δt	$5 \cdot 10^{-12}$ s
Print-out time step, Δt_{print}	10^{-9} s
Total simulation time, t_{final}	$10 \cdot 10^{-6}$ s
Cell size, Δy, Δz	53.59 μm

Source: [3]

Following the same assumption as Bayón-Buján et al. [3], the effects of the background electric and magnetic fields are ignored for the motion of the ions. This approximation is needed for the initial conditions to describe the equilibrium configuration. Note that this approximation is only valid when the values of eB_0/m_i and $E_0L_z/(m_iu_{zi0}^2)$ are small. As the ECDI depends mainly on $\vec{E}_1$ and electron drift, its formation is not affected by this simplification.

At the beginning of the simulation, when it is in equilibrium state, the axial current of electrons $j_{ze0} = 0$. Since the simulation model is collisionless, any transport in this direction is generated by plasma oscillations. Over time, the ECDI grows and eventually saturates, as a result of the in-phase azimuthal oscillations of density and potential, leading to the formation of an axial current. As time goes by, the electron distribution also changes with some electron heating associated with it, yielding a final temperature of about 8-10 eV.

As explained by Bello-Benítez et al. [6], one can take advantage of the periodic boundary condition applied to the y boundaries of the simulation to choose L_y in such a way that the modes agree with the peaks in linear growth predicted by the theory of ECDI. Thus, by setting $L_y = 6 \cdot 2\pi u_{ye0}/\omega_{ce}$, the wavenumbers are given by $k = n\omega_{ce}/(6u_{ye0})$, $\quad n = 1, 2, 3, \ldots$

The initial 1μs of the simulation is ignored, as it represents the transient period during which the instability is developing. For the rest of the simulation (1μs to 10μs) the ECDI is considered to have reached nonlinear saturation.

4.2. Simulation Results

4.2.1. Power Spectrum

The perturbations on the plasma produced by the ECDI are present in multiple variables of the plasma. However, one of the most representative of this phenomenon is the electrostatic potential $\phi(t, y, z)$. From Figure 4.2, it can be clearly seen that the plasma has clear oscillations due to the perturbation produced by the ECDI.

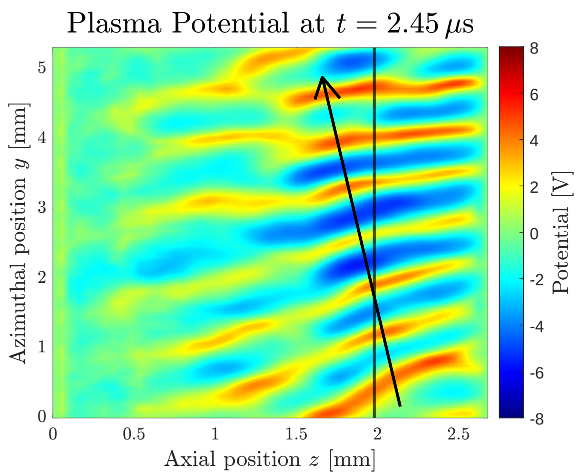

Fig. 4.2. Snapshot of the perturbation electrostatic potential ϕ at $t = 2.45\,\mu$s. The black arrow represents the propagation of the wavefront, which advances on the +y direction with a small component on the -z direction. The black vertical line represents the axial position at which the spectrum of the signal is being analyzed.

Following the same approach as Bayón-Buján et al. [3], the signal spectrum is assumed to be statistically weakly-stationary. To study the oscillations, $\phi(t, y, z)$ is sliced at $z =$

1.98 mm (black vertical line in Figure 4.2) where the oscillations are strong. From this, the two-dimensional PSD and t-k spectrogram are obtained. To do so, windows of 0.5μs with 50% overlap are chosen. For the representation, these values are normalized by their highest value and represented in a logarithmic scale.

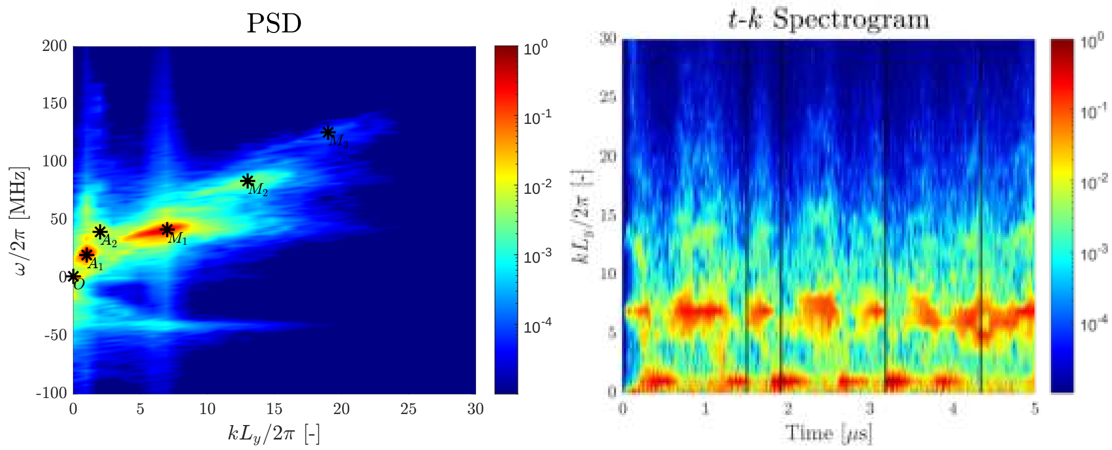

Fig. 4.3. (a) Normalized 2D PSD of the potential at z = 1.98 mm represented in logarithmic scale. (b) Normalized t-k spectrogram of the potential at z = 1.98 mm represented in logarithmic scale. The black vertical lines represent the points at which the snapshots of the wavelet power spectrogram were taken: $t = 1.504, 1.916, 3.185, 4.342\,\mu$s

Looking at Figure 4.3a, six distinct modes (or peaks) can be identified, which are then divided into three groups: the M branch, the A branch, and the near-zero mode.

The M branch corresponds to the cyclotron harmonics predicted by the theory. In Chapter 2.2.1 it was described that these modes were given by the expression: $k_m \approx (m\omega_{ce})/u_{ye0},\ m = 1, 2, 3, \ldots$. When solving the dispersion relation numerically, these modes are located at $kL_y/2\pi = 1 + 6m$ thanks to the discretization previously chosen (Figure 4.4). The M_1, M_2 and M_3 modes identified in Table 4.2 are situated at $kL_y/2\pi = 7, 13, 19$, which coincide with the first three harmonics. In addition, the same goes for the frequencies that follow $\omega/2\pi = m \cdot 42$MHz, as a consequence of the linear approximation of the dispersion relation: $\omega \approx k_y u_{ye0}$.

Unlike the previous branch, the A branch is not predicted by the current theory for ECDI. It is important to note that Figure 4.3b suggests that both branches alternate in time. As a result, this branch is hypothesized to be linked with the nonlinear processes related to the saturation of the instability.

The last one, the O mode, represents an oscillation in the azimuthal direction at a lower frequency than the other modes. This mode is theorized to be related to axial ion dynamics due to its proximity to the ion transit frequency u_{zi}/L_z = 0.9 MHz [3]. As it was proven by Bayón-Buján et al. [3], this mode was shown to have no effect on axial electron transport.

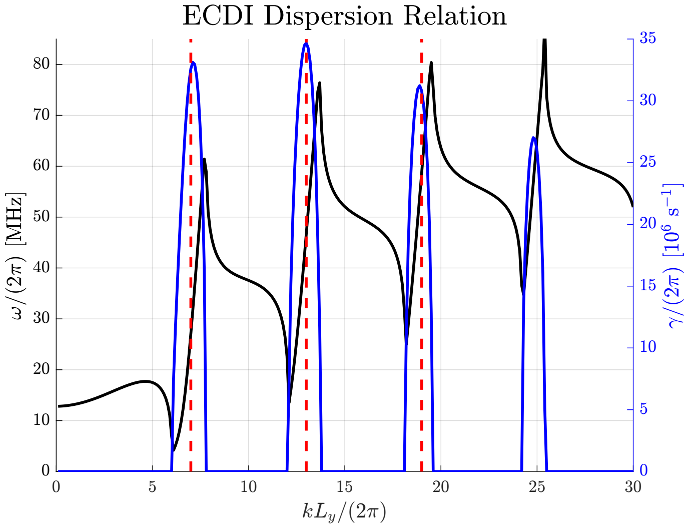

Fig. 4.4. Dispersion Relation of the simulated plasma. On black, the real frequencies of the instability; on blue, the growth rate. The vertical red vertical dashed lines indicate the location of the modes of the M branch: $kL_y/2\pi = 7, 13, 19$. The dispersion relation was obtained following the method described by Cavalier et al. [9].

TABLE 4.2. IDENTIFIED MODES.

Branch	Mode	Coordinates ($\omega/2\pi$, $kL_y/2\pi$)	Description
M	M1	$(42, 7)$	Harmonics of the electron cyclotron frequency
	M2	$(84, 13)$	
	M3	$(126, 19)$	
A	A1	$(20, 1)$	Long-wavelength modes from nonlinear saturation
	A2	$(40, 2)$	
—	O	$(1.6, 0)$	Long-wavelength, low frequency axial mode

As mentioned, branches A and M alternate over time, suggesting that the spectrum of the signal is indeed not stationary. Thereby, instead of applying Fourier analysis, the focus is changed towards wavelet analysis, which is better suited for these cases. To do so, the *semi-wavelet power spectrogram* is introduced to deal with two-dimensional signals. This operation consists of obtaining the Fourier transform of the signal over the spatial dimension and then performing the wavelet transform over time. This semi-wavelet power spectrogram is then evaluated at 4 distinct points that were extracted by looking at Figure 4.3b: one where the M modes are more predominant ($t = 4.342\,\mu$s), one where the A modes are more predominant ($t = 1.916\,\mu$s), one where both are mostly present ($t = 3.185\,\mu$s) and another where both branches look weak ($t = 1.504\,\mu$s). Note that these four timestamps will be used throughout the chapter. The expression describing this semi-wavelet spectrogram is the following:

$$P_\phi^w(\omega, k, t) = |W_t[\tilde{\phi}(t, k)](\omega, t)|^2$$

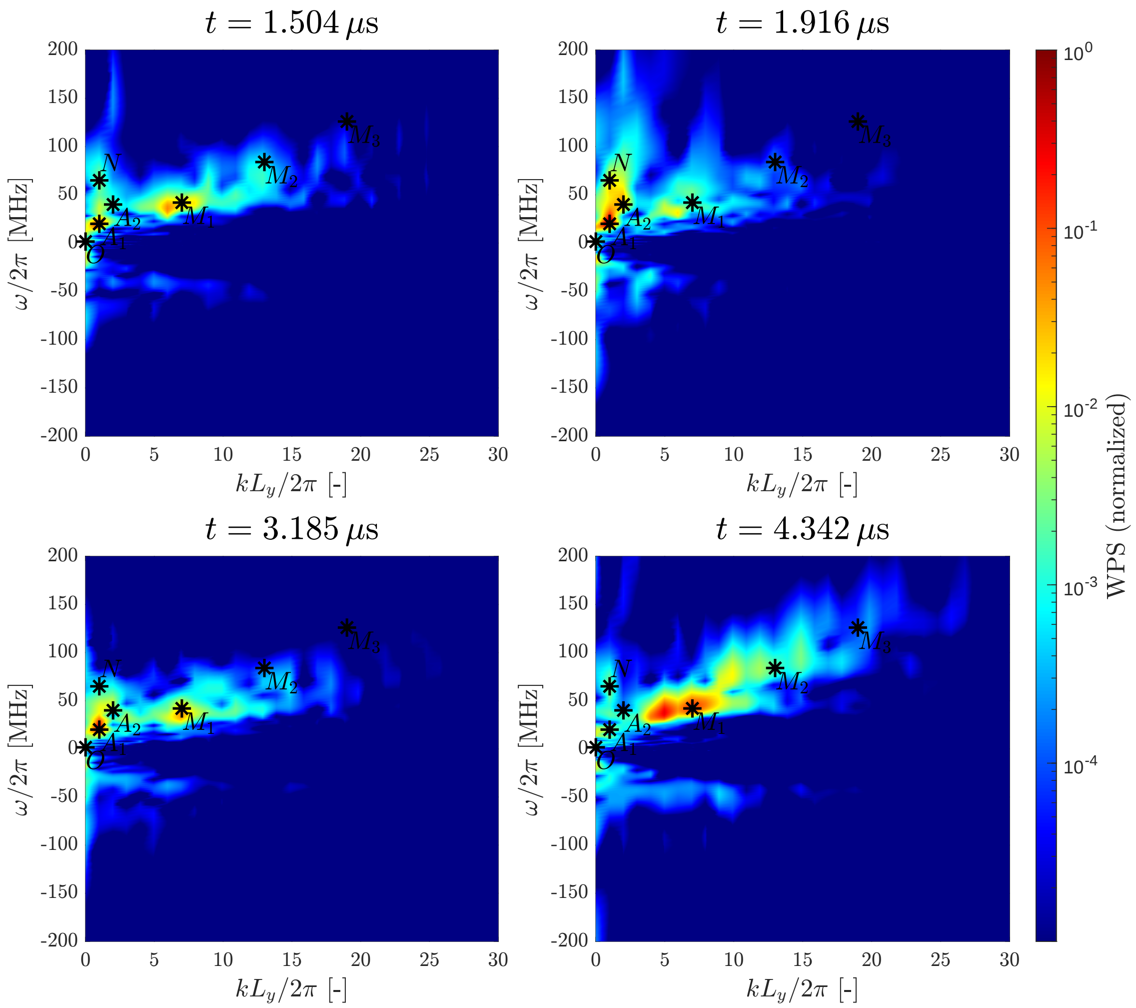

Fig. 4.5. Snapshots of the Wavelet Power Spectrogram of ϕ at different time stamps, overlaid with the modes identified by Bayón-Buján et al. [3] along with the additional mode N.

where $\tilde{\phi}(t, k)$ is the spatial Fourier transform of the slice. The first and most noticeable observation from Figure 4.5 is the confirmation of the non-stationary character of the signal. As shown, for each of the time stamps, the energy distribution along the modes is considerably different, following a cyclic pattern.

Although the four snapshots are not extracted consecutively from the same cycle, they can be used to visualize how the periodic evolution of the modes occurs. To do so, the point of lowest activation ($t = 1.504\mu$s) is selected as the starting point and the plots of Figure 4.5 are followed in the counter-clockwise direction, following the sequence $t = 1.504\,\mu\text{s} \rightarrow 3.185\,\mu\text{s} \rightarrow 4.342\,\mu\text{s} \rightarrow 1.916\,\mu\text{s}$.

At $t = 1.504\,\mu$s both the linear and the nonlinear branches are active but with peaks with relatively low levels of activation. The highest values of activation are around 2 orders of magnitude below the maximum value, with O, A_1 and M_1 being the most active modes.

Furthermore, at this timestamp, a new well-localized mode, designated as mode N, is discovered at coordinates $(\omega/2\pi, kL_y/2\pi) \approx (66, 1)$. Moving on to $t = 3.185\,\mu$s, a clear redistribution of power is identified, where spectral power flows from mode N towards the modes M_1 and A_1. In the next stage, $t = 4.342\,\mu$s, the modes O and A_1 lose intensity, while the N mode gets reactivated along with an increase of the presence of the whole M-branch. Finally, at $t = 1.916\,\mu$s, the energy flows back from the M-branch to the O mode, the N mode, and the whole A-branch.

Note that the overall behavior of the cycle is consistent with the inverse energy cascade described by Bayón-Buján et al. [3]. In their work, they found the net energy transfer to be from high-frequency high-k modes to the low-frequency low-k modes via a statistical approach. As seen, the wavelet analysis is also able to identify this behavior via the time resolution provided by this technique, and rather than a steady flow of energy, it appears to be a cyclic exchange between these modes, which moves both ways, but whose net contribution is that of an inverse cascade. From $t = 4.342\,\mu$s to $t = 1.916\,\mu$s, this inverse energy flow is shown, with energy going from the M-branch to the O, N and A-modes.

As a remark, energy flow in the negative azimuthal direction (negative frequencies) is present, but it remains negligible, with an energy level roughly about 3 orders of magnitude below the maximum.

Regarding the N mode, its characteristic frequency can be directly compared to the parameters displayed in Table 4.1. This reveals that the frequency of this mode is similar to that of the ion plasma frequency $\omega \approx \omega_{pi0} = 66.26\,$MHz, which suggests a relation with ion dynamics, as was the case with mode O. Furthermore, Figure 4.5 shows that the point of highest activation of the N mode is after the inverse energy cascade has taken place and the energy has been redistributed to the low-frequency low-k modes. As a whole, this behavior is consistent with the hypothesis that ions act as an energy sink during the saturation regime, a phenomenon that has already been associated with the saturation of ECDI via ion-trapping vortices [6] and ion wave trapping [68]. However, the wavelet power spectrum indicates only the energy distribution, not a direct measurement of energy flow. As a result, this hypothesis should be regarded as tentative, although consistent with previous studies.

4.2.2. Three-Wave Coupling

Following the same order as Bayón-Buján et al. [3], the anomalous electron transport is now inspected to identify the modes involved in this phenomenon. From Chapter 2, recall that the first order contribution of the $\mathrm{E} \times \mathrm{B}$ axial electron flux is defined as:

$$j_{ze}^{E} = \frac{e}{B_0} E_{y1} n_e$$

As explained, the anomalous axial current is only present when the product of the azimuthal electric field and the electron density $\langle E_{y1} n_e \rangle_{avg}$ does not average to zero. The first step to identify the modes that participate in this electron transport is to look at the energy distribution in a way similar to that done for the plasma potential ϕ. However, this time the Fourier analysis will be skipped. This is due to the fact that in the last section, it was shown that the wavelet power spectrogram was not only able to correctly identify the same modes as the Fourier counterpart but also to add time resolution and provide information about intermittent modes.

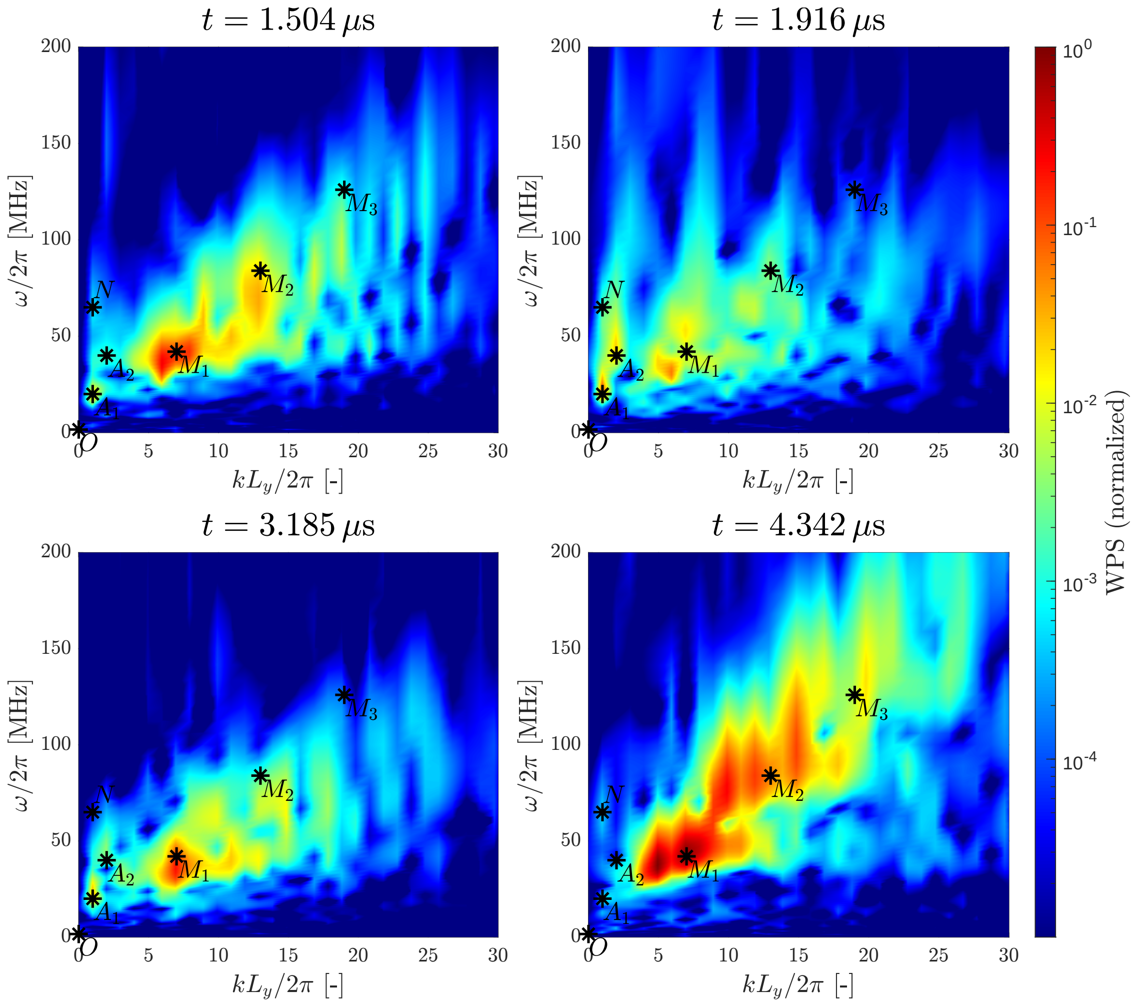

Fig. 4.6. Snapshots of the Wavelet Power Spectrogram of j_{ze}^{E} at different time stamps, overlaid with the modes identified by Bayón-Buján et al. [3] along with the additional mode N.

Figure 4.6 shows that the electron flux inherits the same non-stationary cyclic behavior seen in the plasma potential, which alternates between the A and M modes. This implies that electron transport is itself intermittent. From this figure, it can also be seen that the M mode has higher energy levels for the electron flux when compared to the potential. However, the O mode and A-branch have a similar energy level as that seen in the potential. Nevertheless, the presence of the intermittent N mode is less relevant, being absent at $t = 3.185\,\mu$s.

The wavelet power spectrum is only able to describe the energy distribution of the flux, not the net mean-flow transport. This mean flow electron flux corresponds to the $\omega = 0$, $k = 0$

component of j_{ze}^E. Thus, the nonlinear couplings are studied using the cross-bispectrum under the mean flow condition.

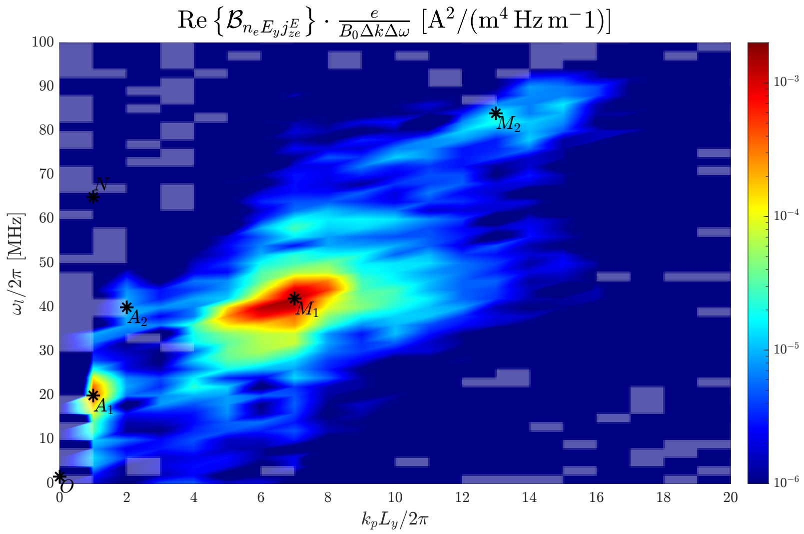

Fig. 4.7. Cross-bispectrum of n_e, E_{y1} and j_{ze}^E for the slice at $z = 1.98$ mm. The white shaded regions represent negative bispectrum values.

Starting with the Fourier cross-bispectrum, Figure 4.7 indicates that the nonlinear interactions are dominated by the mode M_1. In order of contribution to the mean flow transport (from most to least) the modes identified to be involved in the nonlinear couplings are M_1, A_1, M_2 and A_2. In this figure there is no trace of the N mode.

In order to obtain time resolution for the cross-bispectrum, three alternatives are evaluated. Note that in the specific case of mean flow conditions, there is an important caveat that needs to be taken into account. Since this condition requires one frequency and one wavenumber to be equal to zero, the 4-dimensional bispectrum (two frequency dimensions and two wavenumber dimensions) is collapsed into a 2-dimensional $\omega - k$ space. As a result, the azimuthal direction cannot be used to average the bispectrum, as it is now an output dimension. Thus, the three different alternatives proposed are the following:

- The first follows a similar approach as the IWB by taking advantage of the axial direction. Looking at Figure 4.2 the position the slice $z = 1.98$ mm is not the only position where the oscillations are strong. Instead, the range $z \in [1.55, 2.50]$ mm is selected to perform this average.

- The second follows the same averaging process of the WB, using a Hanning window to obtain the time resolution.

- The last method is a hybrid between the WB approach and the Fourier bispectrum. The idea is to perform the average by performing the STFT. Hanning windows of $0.6\,\mu$s are used for this calculation.

Figures 4.8, 4.9 and 4.10 showcase the results of the three bispectrum methods described. The most notable feature of these figures, when compared to the classical Fourier HOS analysis, is the fact that the peaks are more localized. In addition, the cyclic pattern also holds for the bispectrum. Following the evolution of the cycle it can be noted that as the energy is transferred towards the M-modes, the bispectrum magnitude increases at M_1, and then drops drastically. It can also be noted that the A-branch has higher magnitudes just before and after the M-branch peak ($t = 3.185\,\mu$s and $t = 1.916\,\mu$s). Regarding the N mode, there is no presence of it in any of the snapshots. This indicates that this mode is not involved in any quadratic coupling regarding the mean-flow electron flux.

In terms of the comparison between the three approaches, the difference between them is almost negligible. This hints towards the result converging independently of the method used. As can be seen, the shape of the high-bispectrum magnitude regions is practically the same in the three figures. The only noticeable difference is the area of the negative bispectrum values, which seems to be greater for the windowed Fourier bispectrum approach.

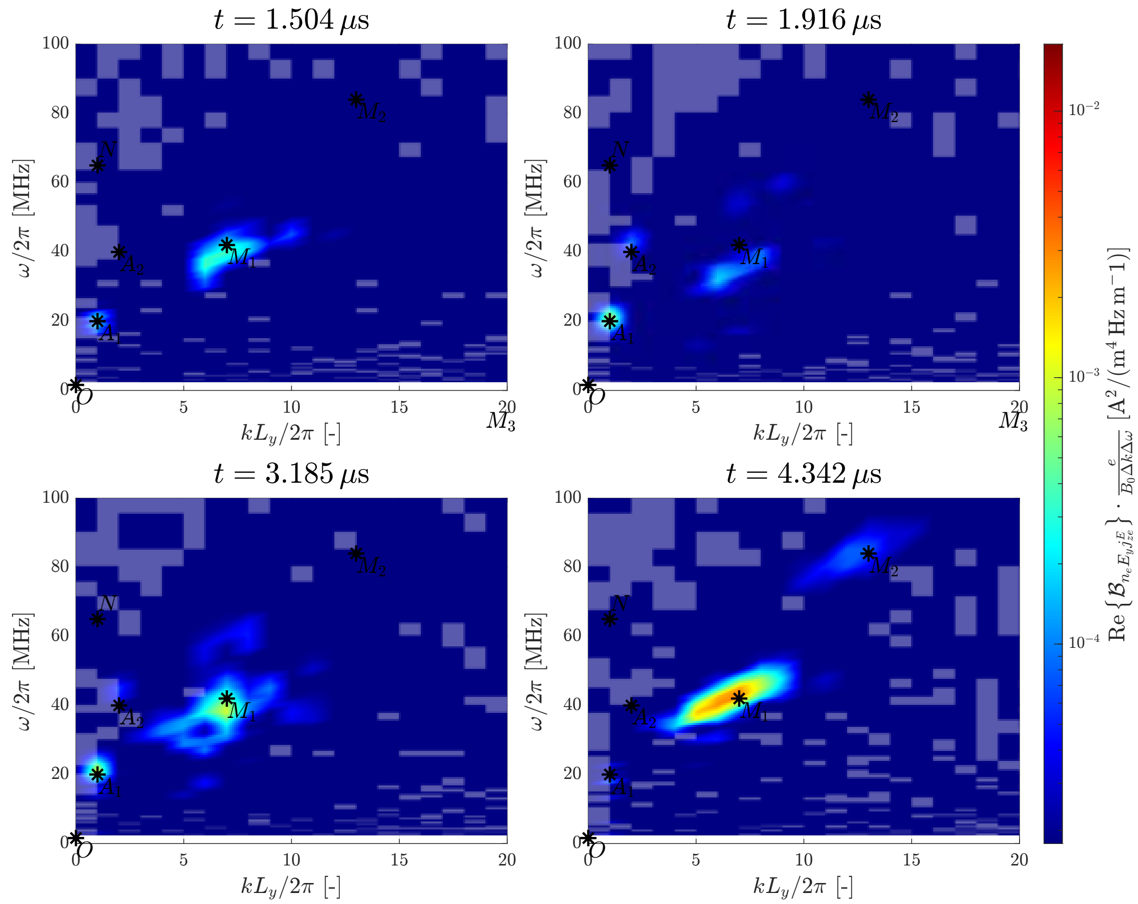

Fig. 4.8. Snapshots of the Instantaneous Wavelet Cross-bispectrum of n_e, E_{y1} and j_{ze}^E at different time stamps, overlaid with the modes identified by Bayón-Buján et al. [3] along with the additional mode N. The white shaded regions represent negative bispectrum values.

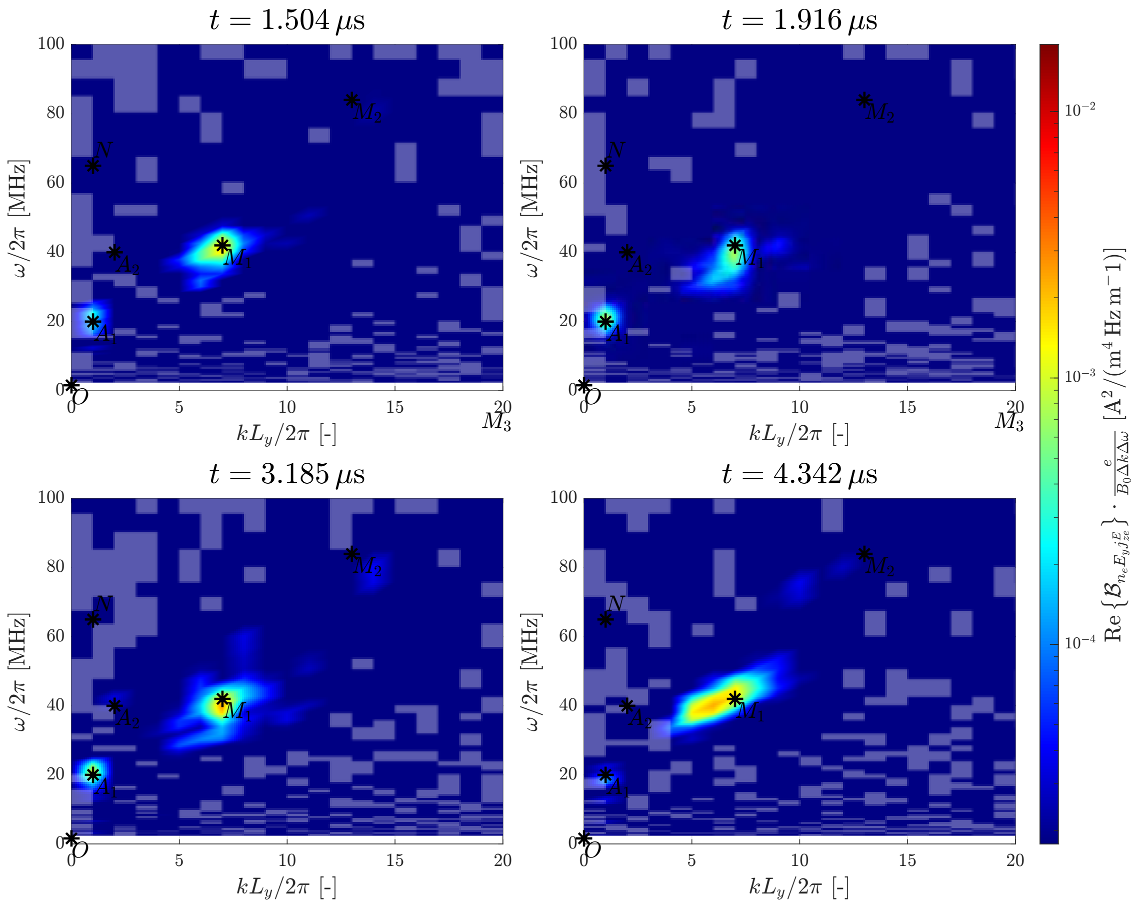

Fig. 4.9. Snapshots of the Wavelet Cross-bispectrum of n_e, E_{y1} and j^E_{ze} at different time stamps, overlaid with the modes identified by Bayón-Buján et al. [3] along with the additional mode N. The white shaded regions represent negative bispectrum values.

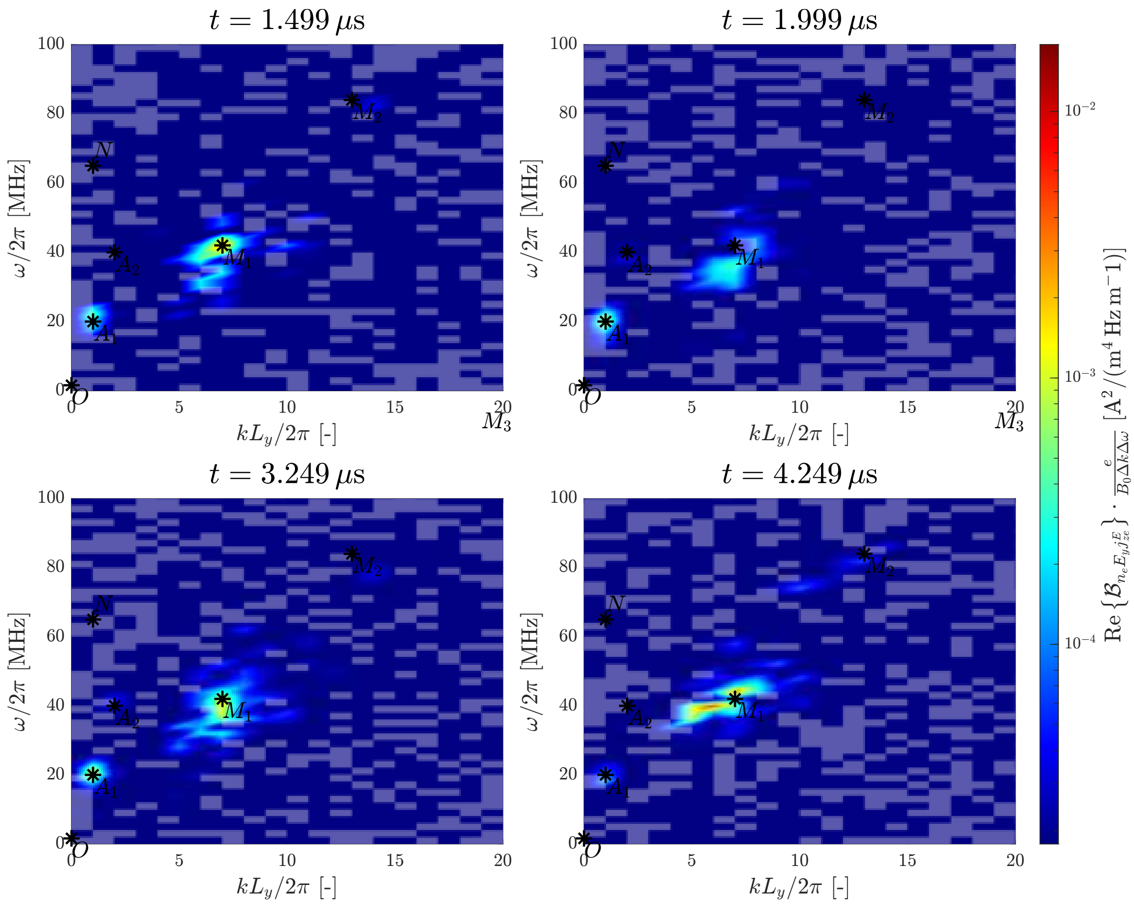

Fig. 4.10. Snapshots of the Windowed Fourier Cross-bispectrum of n_e, E_{y1} and j_{ze}^E at different time stamps, overlaid with the modes identified by Bayón-Buján et al. [3] along with the additional mode N. The white shaded regions represent negative bispectrum values.

4.2.3. Bicoherence

Once branches A and M were identified to have a role in the nonlinear saturation region of the axial transport, the bicoherence of the electric field on the azimuthal direction E_{y1} and the electron density n_e is analyzed (Figure 4.11). To obtain the lower bound for the noise threshold, the number of windows (15) and the number of azimuthal positions (100) are taken into account as independent realizations. When evaluated, this threshold gives a value of $\epsilon[b^2] = 3/M = 3/(15 \cdot 100) = 0.002$.

In terms of the overall behavior of the bicoherence, $\omega_1 - \omega_2$ and $k_1 - k_2$ planes are roughly the same. This is because the frequency and the wavenumber are linked via $\omega = v_{ph} \cdot k$, so if a set of modes has the same velocity, then $\omega \propto k$. This is the case of the M branch, which follows a harmonic pattern, in both their frequencies and wavenumbers, as can be seen in Table 4.2. As a result, both planes show the same frequency scaled by this phase velocity. However, this ratio is not exactly constant, indicating that the modes do not share the same phase velocity. Additionally, each of the peaks is not an isolated point, but rather a small region of bicoherence due to spectral broadening.

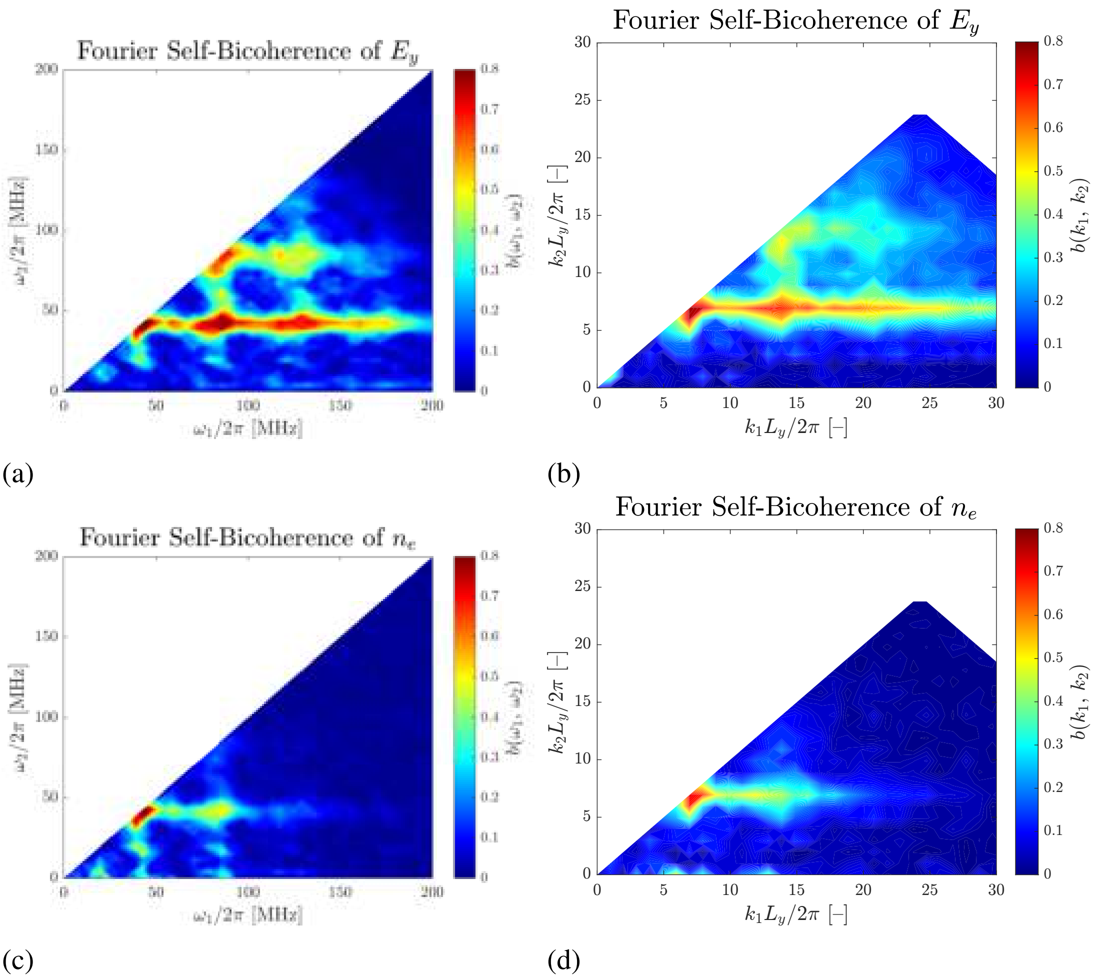

Fig. 4.11. (a) Fourier bicoherence of E_{y1} in the $\omega_1 - \omega_2$ plane. (b) Fourier bicoherence of E_{y1} in the $k_1 - k_2$ plane. (c) Fourier bicoherence of n_e in the $\omega_1 - \omega_2$ plane. (d) Fourier bicoherence of n_e in the $k_1 - k_2$ plane.

Looking at the self-bicoherence of the electric field (Figures 4.11a and 4.11b), the strong interaction between the M branch modes can be easily identified. The most relevant is mode M_1, which interacts with the higher modes through $M_1M_2 \rightleftharpoons M_3$[8] and $M_1M_1 \rightleftharpoons M_2$. These couplings are indicated by the horizontal line at $\omega_2/2\pi = 42\,\mathrm{MHz}$, or equivalently $kL_y/2\pi = 7$. In their work, Bayón-Buján et al. [3] identified these two triads, via Sparse Identification of Nonlinear Dynamics, as those responsible for the inverse cascade that was previously introduced. On the other hand, the A-branch, although visible, has a lower bicoherence, meaning a weaker nonlinear coupling $A_1A_1 \rightleftharpoons A_2$.

For electron density (Figures 4.11c and 4.11d), nonlinear couplings are less present than in the electric field. Although mode M_1 is still present for this variable, the range of frequencies with nonlinear coupling associated to it is significantly lower, suggesting an interaction between modes M_1 and M_2 such that $M_1M_1 \rightleftharpoons M_2$. Directing the attention to the horizontal axis of these figures, a strong interaction between mode O and mode A_1,

[8] The $AB \rightleftharpoons C$ notation means that the modes meet the coupling condition such that $\omega_A + \omega_B = \omega_C$ and $k_A + k_B = k_C$

plus two weaker ones between the former and M_1 and M_2 are identified.

In terms of the N mode, there is a point with intermediate levels of bicoherence ($b \approx 0.5$) at $(\omega_1/2\pi, \omega_2/2\pi) \approx (66, 84)$ MHz in the self-bicoherence of the electric field (Figure 4.11a). However, this point does not correspond to any triad of the modes identified, indicating that N is not involved in the three-wave coupling. This is consistent with the previous cross-bispectrum result, where it was shown that it does not contribute to the anomalous transport.

For the time-resolved analysis, the WB, the IWB and the windowed Fourier bicoherence will be compared to see how they react to the same signal. Starting with the WB, Hanning windows of $0.6\,\mu$s are applied to obtain the time resolution. For these settings, the map of the error threshold is provided in Figure 4.12.

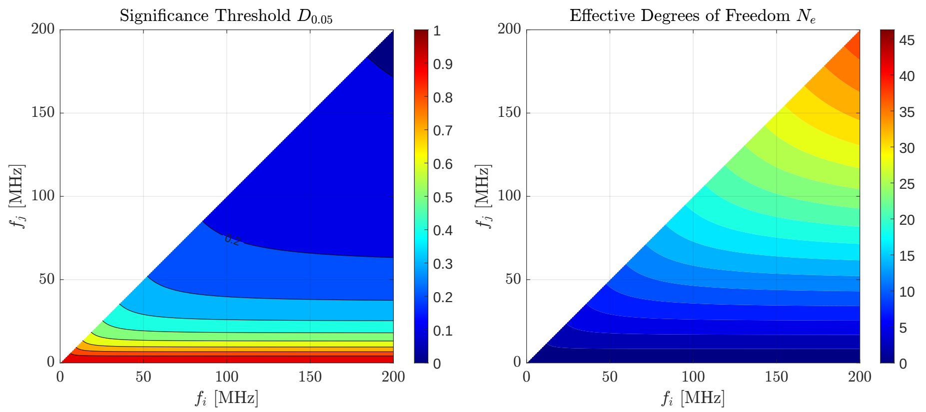

Fig. 4.12. On the left, the map of the significance threshold for the region of the WB that will be analyzed. On the right, the map of the effective degrees of freedom of the slice. Note that although $N_T = 600$ in this case, the error threshold is relatively high due to a sharp decrease in the number of independent samples.

As in the case of the cross-bispectrum, the bicoherence will be obtained at the same four timestamps as before. In this case, to deal with the bi-dimensional slices, the spatial dimension is averaged out, to obtain a function that depends on ω_1, ω_2, and time t. This semi-WB is described as follows:

$$[b^w]^2(t, \omega_1, \omega_2) = \frac{|B(t, \omega_1, \omega_2)|^2}{\left(\int_{-\infty}^{\infty} \left[\frac{1}{N_s}\sum_{s=1}^{N_s} |W_x(\tau, \omega_1, s)|^2 \cdot |W_x(\tau, \omega_2, s)|^2\right] h(t-\tau)\, d\tau\right) \cdot P_x^w(t, \omega_1, \omega_2)}$$

where the WPS and wavelet bispectrum are:

$$P_x^w(t, \omega_1, \omega_2) = \int_{-\infty}^{\infty} \left[\frac{1}{N_s}\sum_{s=1}^{N_s} |W_x(\tau, \omega_1 + \omega_2, s)|^2\right] h(t-\tau)\, d\tau$$

$$B(t,\omega_1,\omega_2) = \int_{-\infty}^{\infty} \left[\frac{1}{N_s} \sum_{s=1}^{N_s} W_x(\tau,\omega_1,s) \cdot W_x(\tau,\omega_2,s) \cdot \bar{W}_x(\tau,\omega_1+\omega_2,s) \right] h(t-\tau)\, d\tau$$

in these expressions $h(t)$ represents the Hanning window used. Note that this method imposes a clear limitation relative to the WB: the $k_1 - k_2$ plane cannot be obtained directly via the CWT, since the frequency domain cannot be "collapsed" in the same way as it is done with the spatial dimension, because the frequencies cannot be treated as independent realizations due to the dependency introduced by the CWT. However, this does not impose a big problem, since it was previously shown that both the $\omega_1 - \omega_2$ and $k_1 - k_2$ planes have the same information.

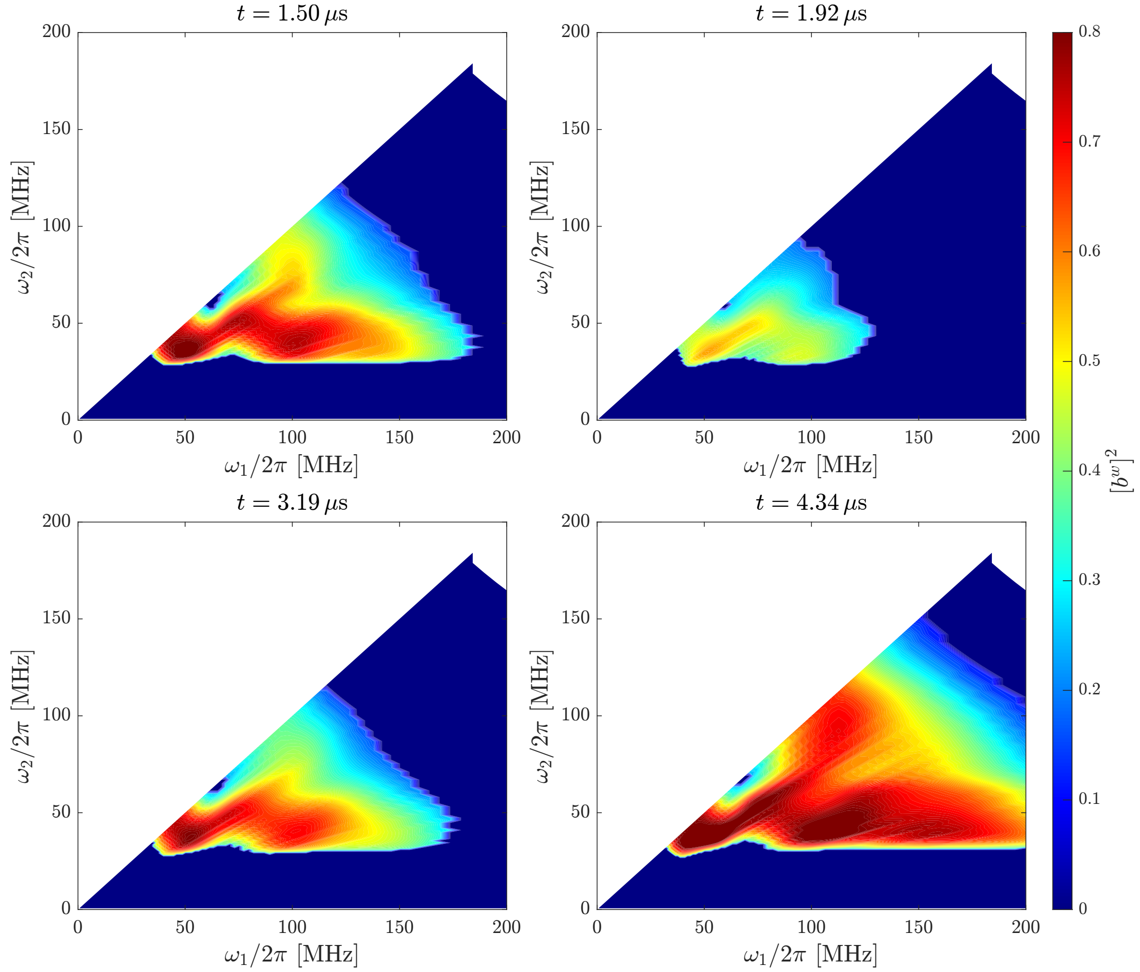

Fig. 4.13. WB of E_{y1} at t = 1.504, 1.916, 3.185, 4.342 μs.

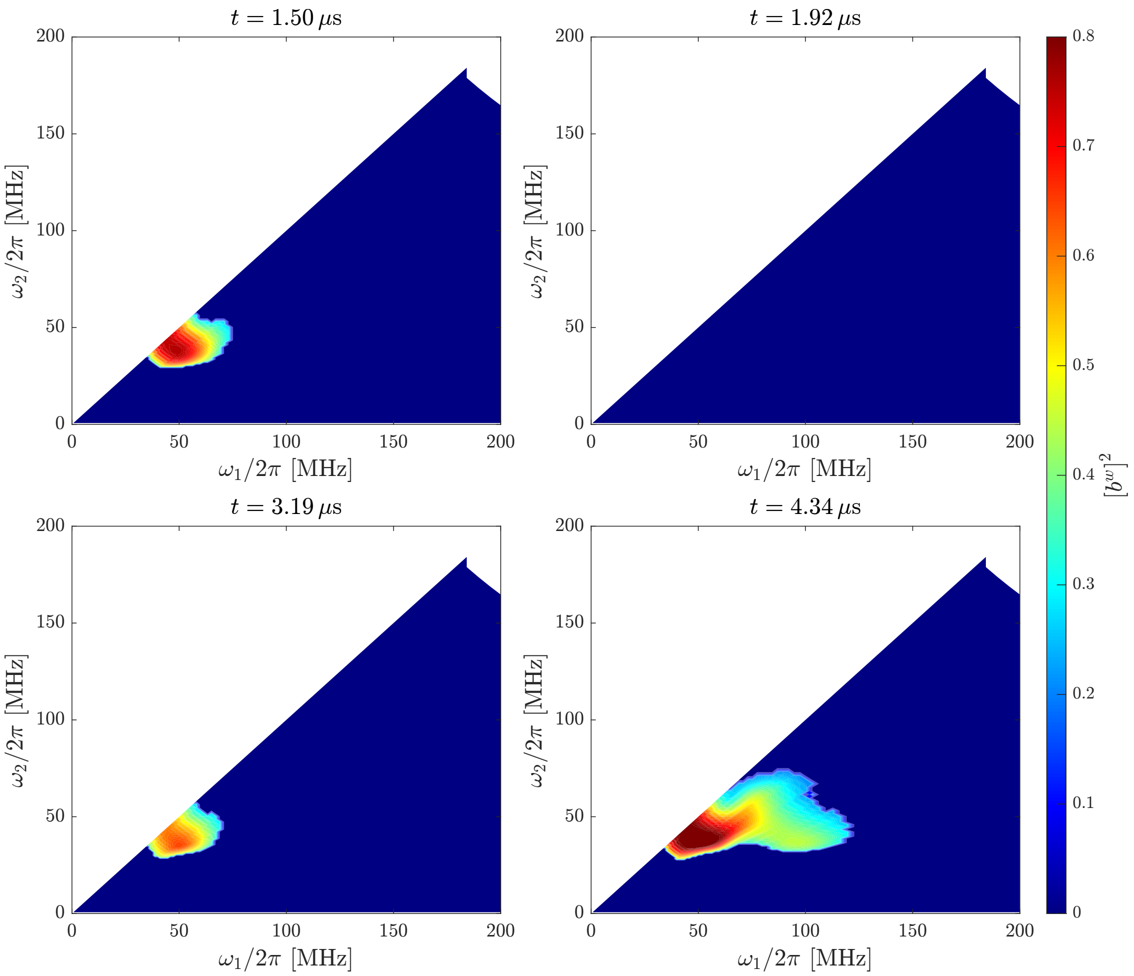

Fig. 4.14. WB of n_e at $t = 1.504, 1.916, 3.185, 4.342\,\mu$s.

Looking at Figures 4.13 and 4.14, the most eye-catching thing is the lack of features present on these plots. However, this is due to the high significance threshold that was obtained for the given parameters used in the analysis. Looking at the modes, the first thing to notice is that these are no longer defined in well-localized frequency bins, but rather in big "blobs" of bicoherence. The influence of M_1 on higher modes is still present in E_{y1}, but the interaction $A_1A_1 \rightleftharpoons A_2$ is no longer visible. In addition, in Figure 4.13, there appears to be a peak of bicoherence around (77, 53) MHz, but no modes were identified for those values. Since this point is close to points that were previously found to have high values of bicoherence, the broadband of these interactions might have produced this point of high bicoherence.

Moving on to the IWB, two averaging methods will be discussed. The first one is to continue with the slab that was taken at $z = 1.98$ mm. As it was previously described in Chapter 3, this version of the wavelet bicoherence needs to be averaged over multiple realizations. Performing an ensemble average with this method would deteriorate the result since the time of the analysis would be determined by the signal length. However, one can take advantage of the fact that we are dealing with spatiotemporal signals to average over the spatial dimensions. Here, a similar approach as that employed for the cross-bispectrum is used: the idea is to average over the azimuthal and axial dimensions to reduce the variability of the result, giving rise to the second average that would be studied. Just as in the WB, averaging over spatial dimensions would remove the ability to obtain a bicoherence function dependent on the wavenumbers and time. In terms of the error, the first average uses 100 azimuthal samples, so that $\epsilon[b^2] = 3/M = 3/100 = 0.03$. For the other method, the 18 samples between $z = 1.55$ mm and $z = 2.50$ mm are taken, as a result $\epsilon[b^2] = 3/M = 3/(18 \cdot 100) = 0.00167$. The selected timestamps are the same as those used for the WB.

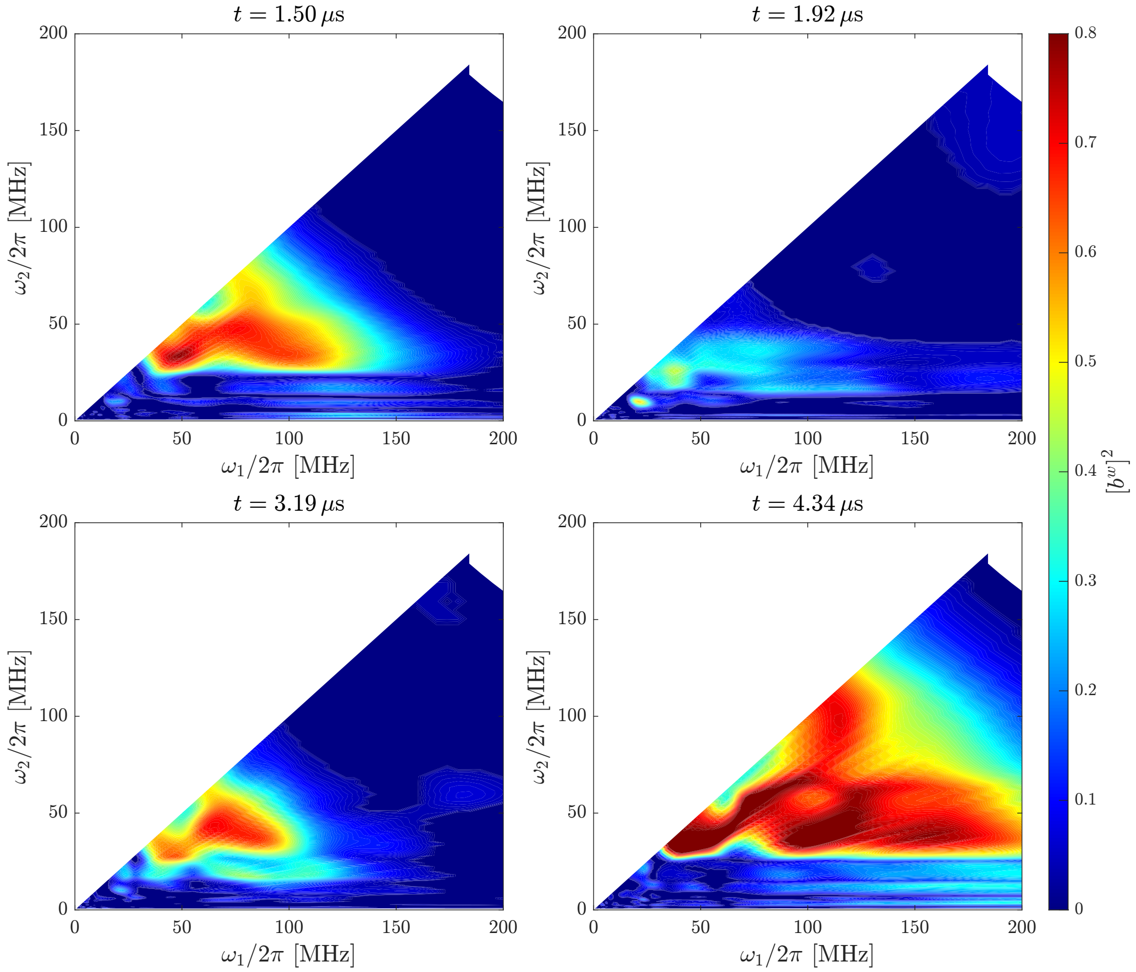

Fig. 4.15. IWB of E_{y1} at slice $z = 1.98$ mm and at $t = 1.504, 1.916, 3.185, 4.342\,\mu$s.

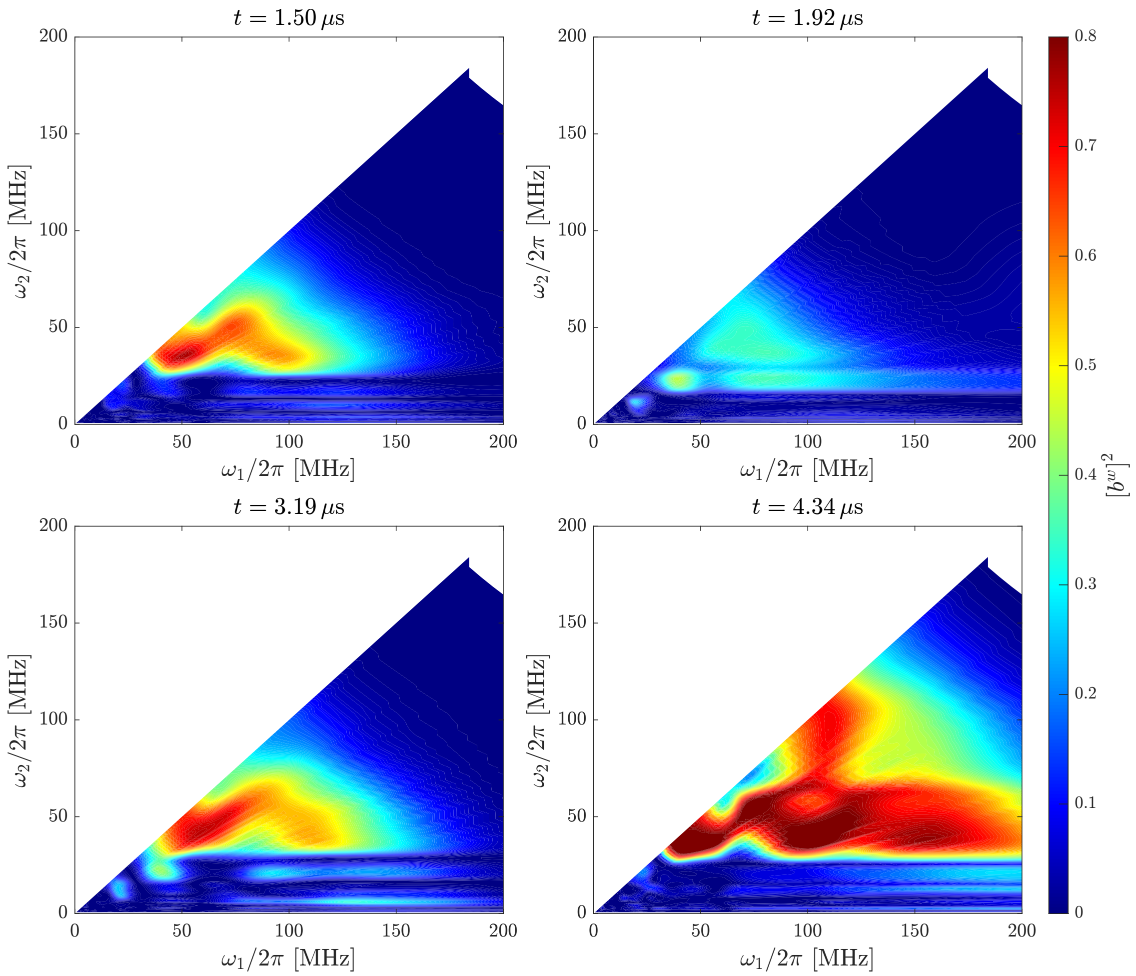

Fig. 4.16. IWB of E_{y1} averaged over multiple slices at $t = 1.504, 1.916, 3.185, 4.342\,\mu$s.

Looking at the IWB of E_{y1}, some notable changes can be seen with respect to the WB. Overall, the amount of features shown in Figures 4.15 and 4.16 is higher than those at Figure 4.13, especially for the A branch, which was not present in the latter. However, the same oscillatory motion is still present. When comparing the two average methods used for the IWB, they show almost identical behaviors as would be expected since they are the same method, but with different amounts of realizations.

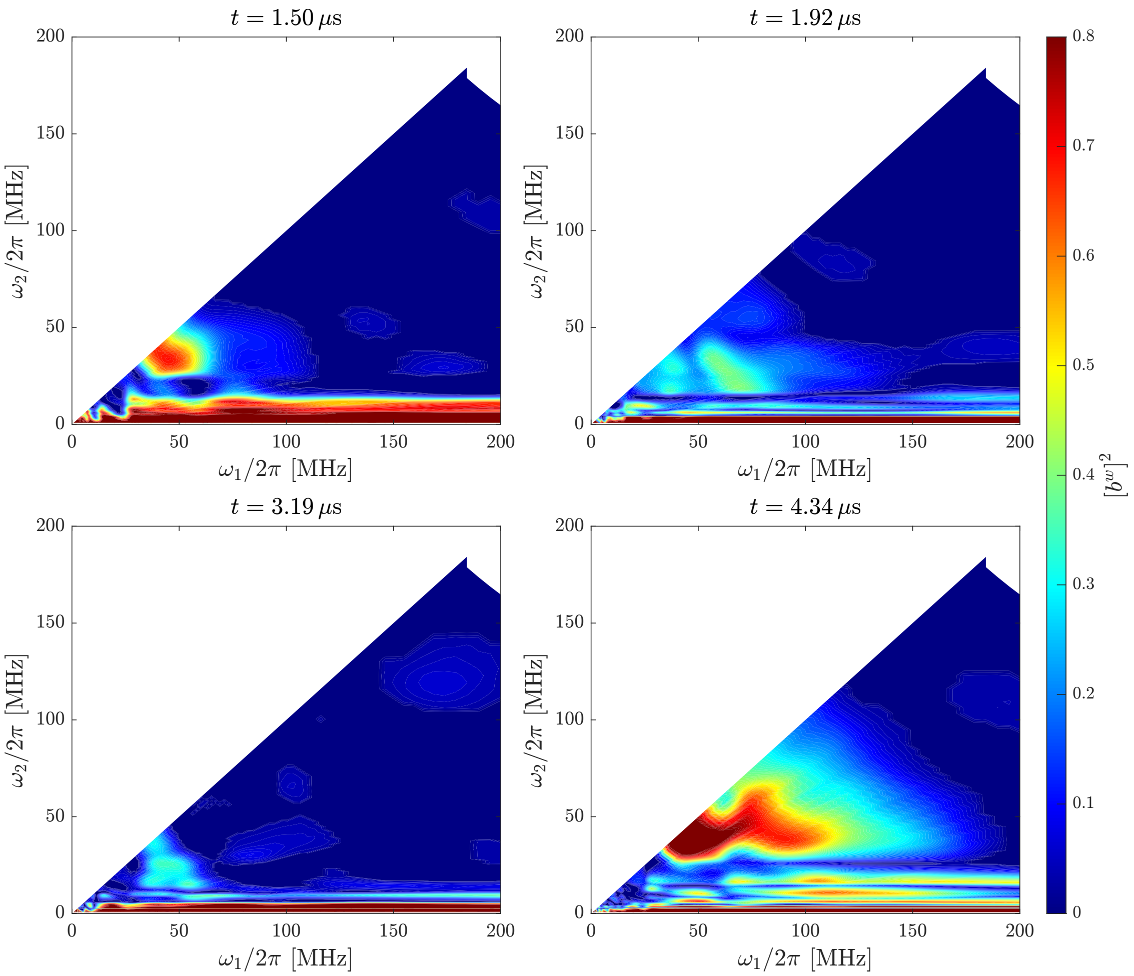

Fig. 4.17. IWB of n_e at slice $z = 1.98$ mm and at $t = 1.504, 1.916, 3.185, 4.342\,\mu$s.

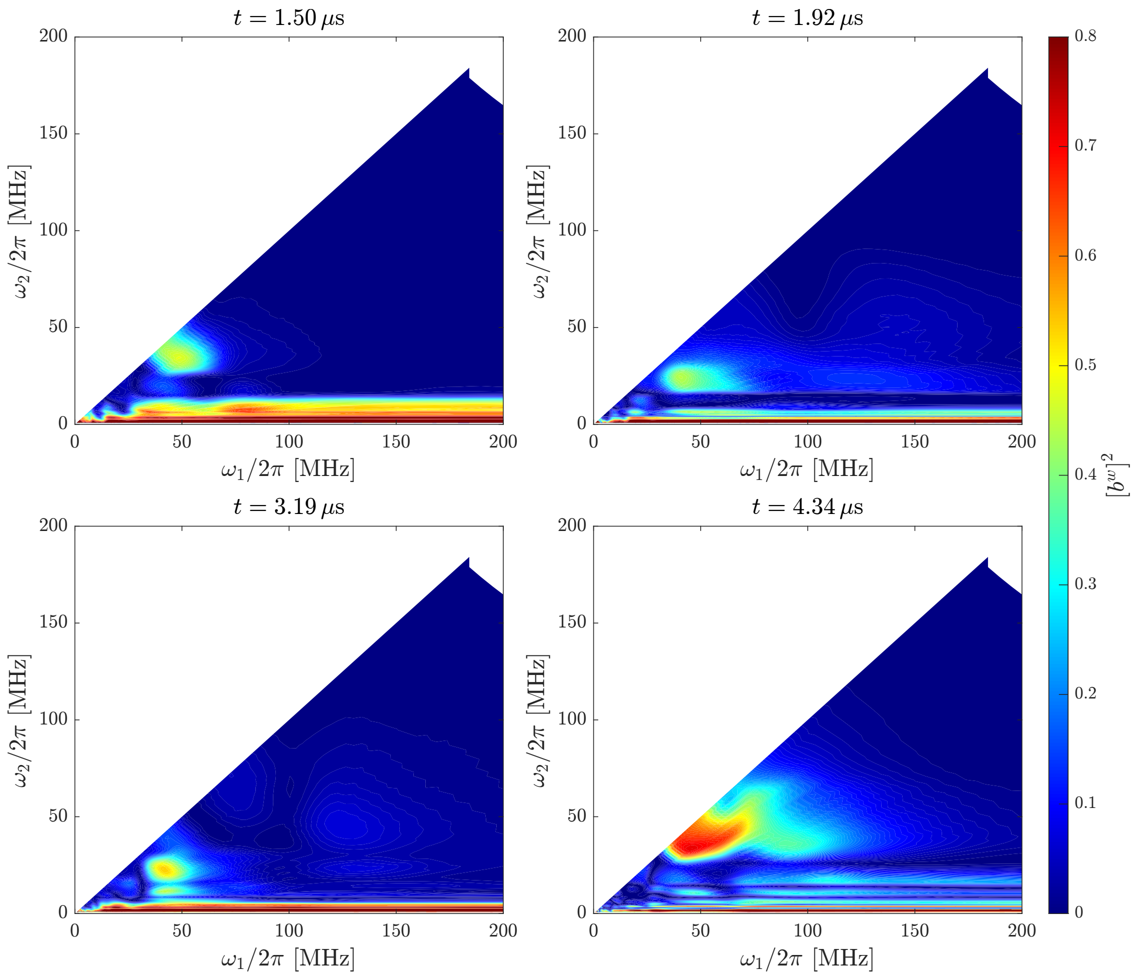

Fig. 4.18. IWB of n_e averaged over multiple slices at $t = 1.504, 1.916, 3.185, 4.342\,\mu$s.

In terms of the IWB of n_e, the comparison with the WB is very similar to that done with E_{y1}. Note that by using this method, the interaction of the O mode spans all over the spectrum. However, one has to be careful with this behavior, since it might be due to the nature of the wavelet bispectrum, which has a higher bias at lower frequencies. As explained in Chapter 3, the WB accounts for this effect by making the threshold depend on the frequency, but this type of adjustment does not exist for the IWB in the literature. As a result, numerical errors are introduced into the analysis, which might lead to false positives. When comparing both averaging methods employed for the IWB it can be clearly seen that many of the artifacts that appear at low frequencies disappear as the number of realizations increases. In conclusion, high values of bicoherence were expected close to $\omega/2\pi = 0\,$MHz, but not for the whole spectrum.

Finally, the results of the windowed Fourier are presented in Figures **??** and 4.20. In this case, the bicoherence regions are reduced to small points with relatively high values. As explained in Chapter 3 this might be due to the fact that the averaging performed by the Fourier counterpart requires a higher number of data points to yield results comparable to those of the wavelet bicoherence.

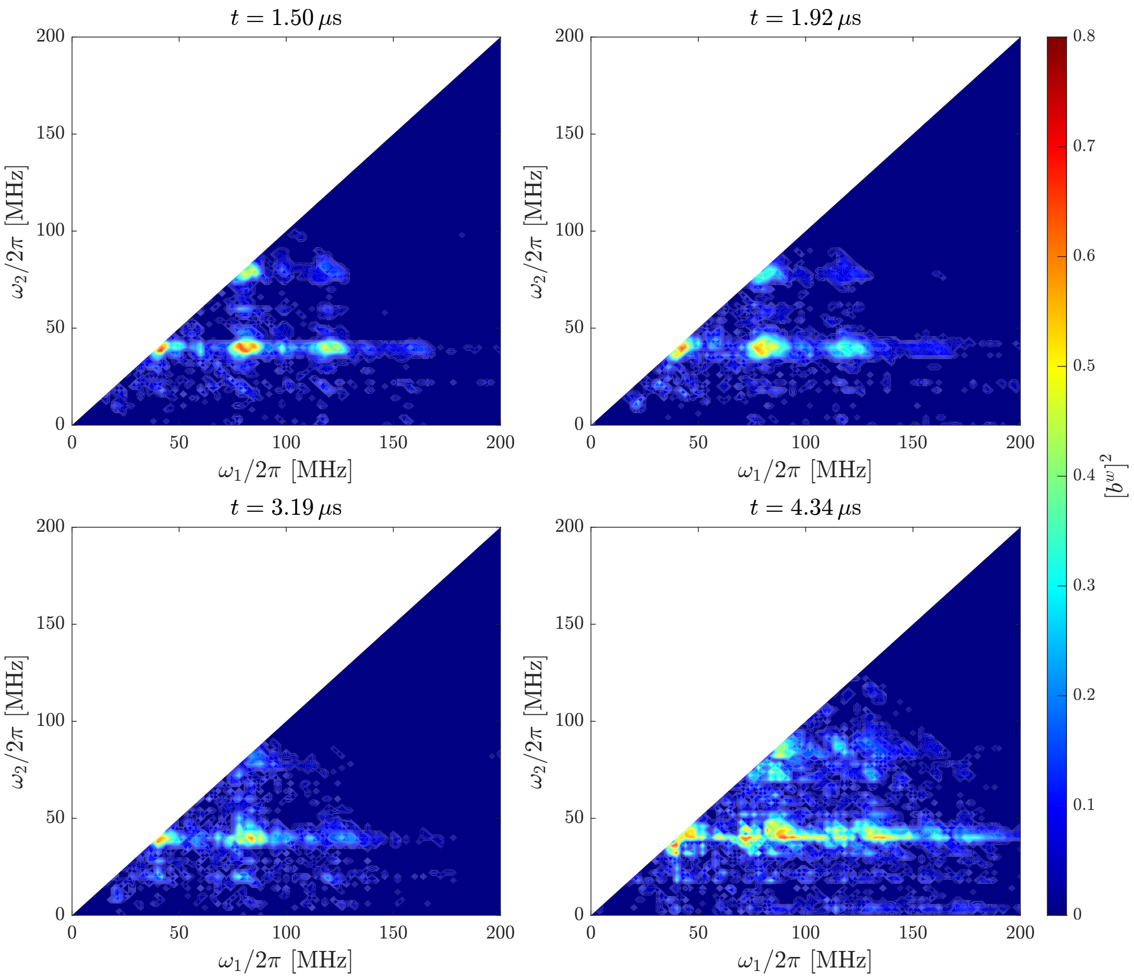

Fig. 4.19. Windowed Fourier self-bicoherence of E_{y1} at slice $z = 1.98$ mm and at $t = 1.504, 1.916, 3.185, 4.342\,\mu$s.

Unlike the Fourier bicoherence presented by Bayón-Buján et al. [3], the results from all these four methods reveal that the couplings of the modes are not only non-stationary, but also that they switch on and off sequentially through the cycle. In terms of E_{y1}, at the beginning only the triads $M_1M_2 \rightleftharpoons M_3$ and $M_1M_1 \rightleftharpoons M_2$ are active. In the next stage, these start to lose intensity and $A_1A_1 \rightleftharpoons A_2$ appears. Then, when the energy is transferred to the M-branch, the coupling extends to a big part of the spectrum. Once the M-branch reduces energy, the couplings of the M-modes get "switched-off" and only the $A_1A_1 \rightleftharpoons A_2$ triad remains.

In the case of n_e, the triad $M_1M_1 \rightleftharpoons M_2$ is present throughout the cycle, having higher nonlinear coupling when the M-branch gets energized. In the IWB and windowed Fourier results, the coupling between the O mode and A_1, M_1 and M_2 seems to be constant over time.

In order to get a sense of how these bicoherence oscillations evolve over time, the *wavelet summed bicoherence* is introduced. This quantity is described as:

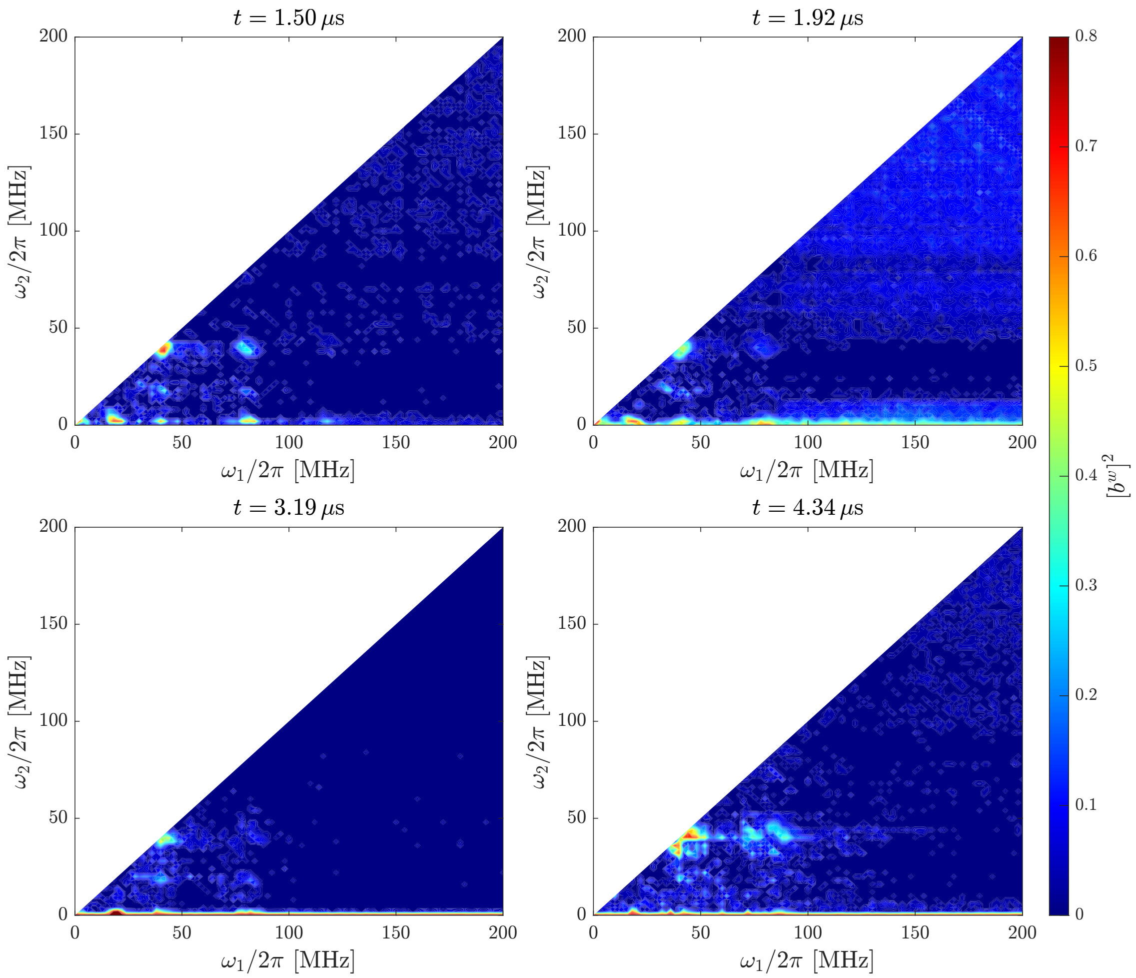

Fig. 4.20. Windowed Fourier self-bicoherence of n_e averaged over multiple slices at $t = 1.504, 1.916, 3.185, 4.342\,\mu$s.

$$[b^w(t)]^2 = \frac{1}{S} \sum \sum [b^w(\omega_1, \omega_2, t)]^2$$

where S is the number of terms of the summation. These quantities are represented in Figures 4.21 and 4.22 for the electric field and plasma electron density, respectively. Looking at these curves for the electric field it can be seen that the highest values of bicoherence are given by the IWB using only azimuthal average, followed by the IWB using the double spatial average, the WB and, finally, the windowed Fourier bicoherence. In the case of the electron density, the windowed Fourier bicoherence presents higher values than the WB, but still lower than the IWB methods. In addition, it can be noted that the oscillations of the wavelet methods have the same periods and phases, while the Fourier one does not match with any.

From this analysis some conclusions can be drawn from the methods used. Windowed Fourier bicoherence is not reliable. Its low tolerance to small windows distorts the overall temporal behavior of the bicoherence. In this specific case, the IWB offers a more reliable alternative due to the availability of multiple ensembles thanks to the multidimensionality

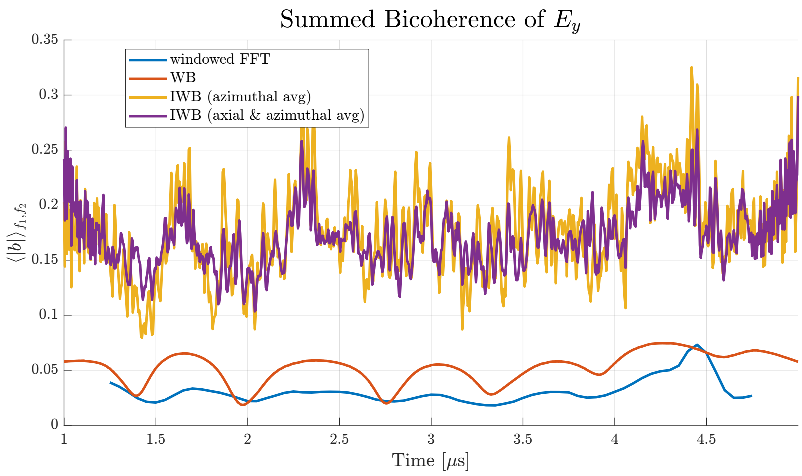

Fig. 4.21. summed bicoherence of E_{y1} using the WB (blue line), the IWB at the slice z = 1.98 mm (orange line), and the IWB averaged over multiple slices (yellow line).

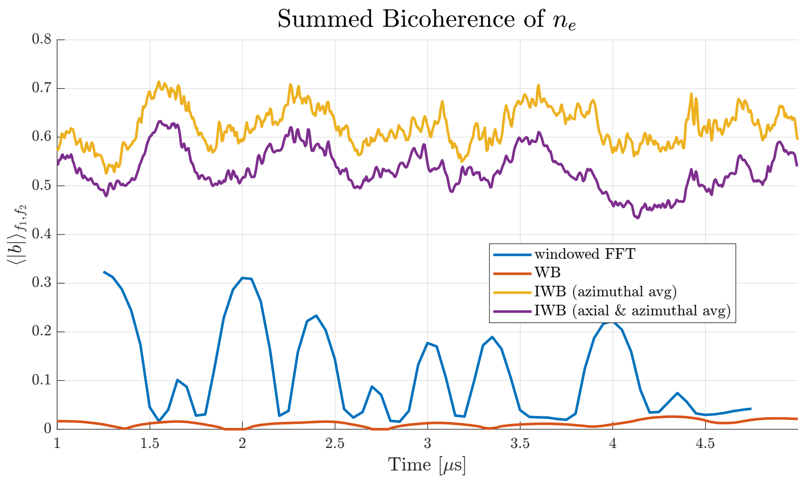

Fig. 4.22. summed bicoherence of n_e using the WB (blue line), the IWB at the slice z = 1.98 mm (orange line), and the IWB averaged over multiple slices (yellow line).

of the data provided. However, the WB seems to be unreliable in the cases where the temporal samples are limited. By looking at Figure 4.12 it can be seen that the minimum threshold is of approximately 0.1, but the values of bicoherence in Figures 4.21 and 4.22 are all below this threshold. This is not the case for the IWB, which stays way above its threshold (0.03 and 0.0017). The conclusions from the comparison of all the bicoherence methods are summarized in Table 4.3.

TABLE 4.3. COMPARISON OF THE DIFFERENT BICOHERENCE METHODS EMPLOYED.

Method	Time resolution	k-plane	$\epsilon[b^2]$	Feature detection	Low-ω bias correction
Fourier (ensemble average)	No	Yes	0.002	High	No
Windowed Fourier	Yes	Yes	0.043	Low	No
WB	Yes	No	≈ 0.1	Low	Yes
IWB (azimuthal avg.)	Yes	No	0.03	Moderate	No
IWB (multi-slice avg.)	Yes	No	0.0017	High	No

5. CONCLUSION

5.1. Objectives Met

This project aimed to reevaluate the results of the study by Bayón-Buján et al. [3], which focused on the nonlinear saturation region of the ECDI instability. In their work, the spectrum was analyzed under the assumption that it is stationary. However, this is known to not be the case for plasma properties. This work tested the hypothesis that a time-resolved tool like the wavelet analysis could reveal information hidden by the averaging performed by Fourier tools.

The main conclusion of this study is that the wavelet analysis was not able to discover large amounts of unseen modes or couplings. The spectral content displayed by the analysis on the same dataset as that used by Bayón-Buján et al. [3] agrees with the stationary analysis. However, the time-resolved analysis revealed a (almost) periodic behavior of the spectrum. This indicates that the Fourier results are a time-average of this cyclic behavior in which the energy is continuously exchanged between the A and M modes of the spectrum. From this perspective, the hypothesis can be considered confirmed since it revealed the temporal evolution of the spectrum, rather than new modes.

This cyclic behavior is the central result of this project, and is seen consistently throughout all the analyses performed, each of them providing a different perspective of the same underlying process:

- The wavelet power spectrogram of the potential revealed the A and M branches alternating in time.
- The wavelet power spectrogram of the axial electron flux showed the intermittent behavior of the anomalous transport.
- The cross-bispectrum exhibited the varying contribution of the M_1 which drives the oscillations of the anomalous axial electron flux.
- The wavelet bicoherence revealed the sequential activation of the three-wave couplings, from the M-branch triads ($M_1M_1 \rightleftharpoons M_2$, $M_1M_2 \rightleftharpoons M_3$) to the A-branch triad ($A_1A_1 \rightleftharpoons A_2$).

As a whole, these four analyses suggest the saturation region of the ECDI is governed by periodic energy exchanges between branches, rather than groups of static interactions.

Furthermore, a new intermittent mode, which was not identified by Bayón-Buján et al., was revealed by the wavelet analysis. This was denoted as the N mode, whose frequency is close to the ion plasma frequency, suggesting a relation with ion dynamics. While bicoherence results hint that N might be involved in some nonlinear couplings, the cross-bispectrum analysis discards it as an actor in the mean-flow anomalous transport.

These results meet the objectives defined in the introduction. On the methodological side, multiple bicoherence methods were tested. The results identified the IWB as the most appropriate estimator for the bicoherence, since the multidimensional origin of the data allowed the use of a larger number of ensembles during the averaging process.

5.2. Future Work

This thesis was subject to a number of limitations, each of which points to towards future research.

One of the main limitations of this study was the simulation data, which limited the statistical resolution of the analysis. Although bicoherence results were sufficient to understand the overall behavior of the couplings, they were not precise enough to determine whether additional couplings went undetected. Larger datasets might allow obtaining cleaner bicoherence plots that would help distinguish actual couplings from artifacts produced by the numerical methods.

A second limitation is that the self-bicoherence was only obtained in the $\omega - \omega$ plane, as opposed to Bayón-Buján et al. [3] who also provide the $k - k$ plane. For this specific dataset, this didn't impose any critical limitations since the phase velocity is shared among different modes, and both planes were shown to share the same information. Due to the nature of one-dimensional wavelet transforms, their two-dimensional counterparts should allow to recover the $k - k$ plane. However, this would require developing the HOS theory for two-dimensional wavelets. Furthermore, two-dimensional wavelets come with an extra constraint which is that they depend on a scaling factor and a rotation, which makes them hard to transform into the frequency and wavenumber domains.

Finally, the methodology studied in this work is not restricted to HET geometries. Since EPTs, like HPTs, are also plasma discharges, they are subject to similar instabilities. As a result, this same time-resolved analysis can be applied to these other devices to better understand the non-stationary behavior that might develop in them.

BIBLIOGRAPHY

[1] NASA/JPL-Caltech, *Psyche's hall thruster (pia24030)*, NASA Jet Propulsion Laboratory (JPL), Accessed: 2026-06-08, 2021. [Online]. Available: https://www.jpl.nasa.gov/images/pia24030-psyches-hall-thruster/.

[2] D. Maddaloni, B. Bayón-Buján, J. Navarro-Cavallé, M. Merino, and F. Terragni, "Low-frequency oscillations in the magnetic nozzle of a Helicon plasma thruster," *Plasma Sources Science and Technology*, vol. 34, no. 4, p. 045 008, 2025. DOI: 10.1088/1361-6595/adc40d. [Online]. Available: https://doi.org/10.1088/1361-6595/adc40d.

[3] B. Bayón-Buján, E. Bello-Benítez, J. Zhou, and M. Merino, "Data-driven analysis of anomalous transport and three-wave-coupling effects in an E × B plasma," *Journal of Electric Propulsion*, vol. 4, no. 1, 2025. DOI: 10.1007/s44205-025-00158-6. [Online]. Available: https://doi.org/10.1007/s44205-025-00158-6.

[4] I. D. Kaganovich *et al.*, "Physics of E × B discharges relevant to plasma propulsion and similar technologies," *Physics of Plasmas*, vol. 27, no. 12, p. 120 601, 2020. DOI: 10.1063/5.0010135. [Online]. Available: https://doi.org/10.1063/5.0010135.

[5] F. Taccogna, F. Cichocki, D. Eremin, G. Fubiani, and L. Garrigues, "Plasma propulsion modeling with particle-based algorithms," *Journal of Applied Physics*, vol. 134, no. 15, p. 150 901, 2023. DOI: 10.1063/5.0153862.

[6] E. Bello-Benítez, A. Marín-Cebrián, and E. Ahedo, "Effect of injection conditions on the non-linear behavior of the ecdi and related turbulent transport," *Physics of Plasmas*, vol. 32, no. 1, p. 012 307, Jan. 2025. DOI: 10.1063/5.0238207. eprint: https://pubs.aip.org/aip/pop/article-pdf/doi/10.1063/5.0238207/20365957/012307_1_5.0238207.pdf. [Online]. Available: https://doi.org/10.1063/5.0238207.

[7] D. W. Forslund, R. L. Morse, and C. W. Nielson, "Electron cyclotron drift instability," *Physical Review Letters*, vol. 25, no. 18, pp. 1266–1270, Nov. 1970. DOI: 10.1103/PhysRevLett.25.1266.

[8] A. Ducrocq, J. C. Adam, A. Heron, and G. Laval, "High-frequency electron drift instability in the cross-field configuration of hall thrusters," *Physics of Plasmas*, vol. 13, no. 10, p. 102 111, 2006. DOI: 10.1063/1.2359718. [Online]. Available: https://doi.org/10.1063/1.2359718.

[9] J. Cavalier, N. Lemoine, G. Bonhomme, S. Tsikata, C. Honoré, and D. Grésillon, "Hall thruster plasma fluctuations identified as the E×B electron drift instability: Modeling and fitting on experimental data," *Physics of Plasmas*, vol. 20, 2013. DOI: 10.1063/1.4817743.

[10] S. Tsikata and T. Minea, "Modulated electron cyclotron drift instability in a high-power pulsed magnetron discharge," *Phys. Rev. Lett.*, vol. 114, p. 185 001, 18 May 2015. DOI: 10.1103/PhysRevLett.114.185001. [Online]. Available: https://link.aps.org/doi/10.1103/PhysRevLett.114.185001.

[11] Z. A. Brown and B. A. Jorns, "Growth and saturation of the electron drift instability in a crossed field plasma," *Phys. Rev. Lett.*, vol. 130, p. 115 101, 11 Mar. 2023. DOI: 10.1103/PhysRevLett.130.115101. [Online]. Available: https://link.aps.org/doi/10.1103/PhysRevLett.130.115101.

[12] J. J. Ramos, E. Bello-Benítez, and E. Ahedo, "Local analysis of electrostatic modes in a two-fluid E×B plasma," *Physics of Plasmas*, vol. 28, no. 5, p. 052 115, 2021. DOI: 10.1063/5.0039341.

[13] J. C. Adam, A. Héron, and G. Laval, "Study of stationary plasma thrusters using two-dimensional fully kinetic simulations," *Physics of Plasmas*, vol. 11, no. 1, pp. 295–305, 2004. DOI: 10.1063/1.1632904.

[14] D. Maddaloni, A. Domínguez-Vázquez, M. Merino-Martinez, and F. Terragni, "Data-driven analysis of breathing mode and ion-transit mode in 2d hybrid hall thruster simulations," in *AIAA Propulsion and Energy 2021 Forum*. DOI: 10.2514/6.2021-3398. eprint: https://arc.aiaa.org/doi/pdf/10.2514/6.2021-3398. [Online]. Available: https://arc.aiaa.org/doi/abs/10.2514/6.2021-3398.

[15] P. Coche and L. Garrigues, "A two-dimensional (azimuthal-axial) particle-in-cell model of a hall thruster," *Physics of Plasmas*, vol. 21, no. 2, p. 023 503, 2014. DOI: 10.1063/1.4864625.

[16] United Nations, *International space law explained*, https://www.un.org/en/peace-and-security/international-space-law-explained, Accessed: 2026-05-30, 2026.

[17] Space Foundation Editorial Team, *International space law*, https://www.spacefoundation.org/space_brief/international-space-law/, Accessed: 2026-05-30, 2025.

[18] European Commission and DG DEFIS, *Eu space act*, https://defence-industry-space.ec.europa.eu/eu-space-act_en, Accessed: 2026-05-30, 2025.

[19] Diario de Sevilla Redacción, *La regulación espacial, ante su momento decisivo: España prepara su primera ley de actividades en el espacio*, https://www.diariodesevilla.es/tecnologia/regulacion-espacial-espana-primera-ley_0_2006544360.html, Accessed: 2026-05-30, Apr. 2026.

[20] Straits Research, “Electric propulsion systems market size, share, growth, analysis, 2034,” Straits Research, Market Research Report, 2026, Accessed: May 31, 2026. [Online]. Available: https://straitsresearch.com/report/electric-propulsion-systems-market.

[21] Dataintelo, *Electric propulsion system market research report 2034*, Market Research Report, Dataintelo Consulting Pvt Ltd. Report ID AD-110574; updated April 2026; accessed 2026-06-08, 2026. [Online]. Available: https://dataintelo.com/report/electric-propulsion-system-market.

[22] J. Trevithick, *A year of firsts for electric propulsion*, Aerospace America (AIAA), Year in Review, Accessed: 2026-06-08, 2024. [Online]. Available: https://aerospaceamerica.aiaa.org/year-in-review/a-year-of-firsts-for-electric-propulsion/.

[23] The MathWorks, Inc., *MATLAB and Simulink student suite*, MathWorks Store, 2026. [Online]. Available: https://www.mathworks.com/store/link/products/student/STUDENT.

[24] Telefónica de España, S.A.U., *Internet en Casa: Tarifas y Ofertas de Fibra óptica*, Movistar España, 2026. [Online]. Available: https://web.movistar.es/landings/?custom=13826616194_kwd-1560486590&sem=900105707&tc_alt=31245&n_o_pst=n_o_pst&n_okw=internet%20en%20casa_b__c_159552305233_13826616194_kwd-1560486590_&gclsrc=aw.ds&gad_source=1&gad_campaignid=13826616194&gbraid=0AAAAAD9hQfsfIY7BM_3bdUXJ3qwx64Dh_&gclid=Cj0KCQjwz9_QBhD_ARIsADnSCfCu_dbzZ7fIJPsqnwL3c4prE0CRCA
QJRra6i6UaAmOUEALw_wcB.

[25] Jobted, *¿cuánto cobra un ingeniero aeroespacial? (sueldo 2026)*, Jobted España, Accessed: 2026-06-08, 2026. [Online]. Available: https://www.jobted.es/salario/ingeniero-aeroespacial.

[26] Jobted, *¿cuánto cobra un profesor universitario? (sueldo 2026)*, Jobted España, Accessed: 2026-06-08, 2026. [Online]. Available: https://www.jobted.es/salario/profesor-universitario.

[27] r/CasualIT Community, *Ma quanto consuma un router Wi-Fi sempre acceso?* Reddit Forum Post, Online discussion thread regarding Wi-Fi router power consumption, 2025. [Online]. Available: https://www.reddit.com/r/CasualIT/comments/1jcgfy4/ma_quanto_consuma_un_router_wifi_sempre_acceso/.

[28] Jefatura del Estado, *Ley 27/2014, de 27 de noviembre, del Impuesto sobre Sociedades*, Boletín Oficial del Estado, núm. 288, págs. 96939 a 97097, Referencia: BOE-A-2014-12328, 2014. [Online]. Available: https://www.boe.es/buscar/act.php?id=BOE-A-2014-12328.

[29] Ministerio de Inclusión, Seguridad Social y Migraciones, *Orden pjc/297/2026, de 30 de marzo, por la que se desarrollan las normas legales de cotización a la seguridad social, desempleo, protección por cese de actividad, fondo de garantía salarial y formación profesional para el ejercicio 2026*, Boletín Oficial del Estado, núm. 78, Referencia: BOE-A-2026-7296, Accessed: 2026-06-08, 2026. [Online]. Available: https://www.boe.es/diario_boe/txt.php?id=BOE-A-2026-7296.

[30] S. D. Heister, W. E. Anderson, T. L. Pourpoint, and R. J. Cassady, *Rocket Propulsion* (Cambridge Aerospace Series). Cambridge, UK: Cambridge University Press, 2019, vol. 47.

[31] D. M. Goebel and I. Katz, *Fundamentals of Electric Propulsion: Ion and Hall Thrusters*. John Wiley & Sons, 2008. DOI: 10.1002/9780470436448.

[32] D. O'Reilly, G. Herdrich, and D. F. Kavanagh, "Electric propulsion methods for small satellites: A review," *Aerospace*, vol. 8, no. 1, p. 22, 2021. DOI: 10.3390/aerospace8010022. [Online]. Available: https://doi.org/10.3390/aerospace8010022.

[33] E. M. Petro and R. J. Sedwick, "Survey of moderate-power electric propulsion systems," *Journal of Spacecraft and Rockets*, vol. 54, no. 3, pp. 529–541, 2017. DOI: 10.2514/1.A33647. eprint: https://doi.org/10.2514/1.A33647. [Online]. Available: https://doi.org/10.2514/1.A33647.

[34] S. Singh, S. Kumar, S. K. Meena, and S. K. Saini, "Introduction to plasma based propulsion system: Hall thrusters," in *Propulsion: New Perspectives and Applications*, M. Kazuo and H. Hiroaki, Eds., IntechOpen, 2021, ch. 4. DOI: 10.5772/intechopen.96916. [Online]. Available: https://doi.org/10.5772/intechopen.96916.

[35] J.-P. Boeuf, "Tutorial: Physics and modeling of hall thrusters," *Journal of Applied Physics*, vol. 121, no. 1, p. 011 101, 2017. DOI: 10.1063/1.4972269.

[36] J. A. Bittencourt, *Fundamentals of Plasma Physics*, 3rd. New York, NY: Springer, 2004.

[37] University of Sydney, *Introduction to plasma physics*, YouTube playlist, USYD - Senior Plasma Physics Lectures, Accessed: 2025-03-11, n.d. [Online]. Available: https://www.youtube.com/playlist?list=PLogdluxJPZEqNAICx2zBrmoYNr_F_jhM3.

[38] R. J. Goldston and P. H. Rutherford, *Introduction to Plasma Physics*. Bristol: Institute of Physics Publishing, 1995.

[39] R. Fitzpatrick, *Plasma Physics: An Introduction*, 2nd. Boca Raton, FL: CRC Press, 2022. DOI: 10.1201/9781003268253.

[40] F. F. Chen, *Introduction to Plasma Physics and Controlled Fusion*, 3rd. Cham, Switzerland: Springer, 2016. DOI: 10.1007/978-3-319-22309-4.

[41] B. B. Hubbard, *The world acccording to wavelets : the story of a mathematical technique in the making*, eng. Wellesley: : AK Peters, 1996.

[42] D. Alcaraz Candela, *Series y transformadas de Fourier (Apuntes de la asignatura)*, Universidad Politécnica de Cartagena (UPCT), Accessed: 27-11-2025, n.d. [Online]. Available: https://www.dmae.upct.es/~paredes/am_ti/apuntes/Tema%202.%20Series%20y%20transformadas%20de%20Fourier.pdf.

[43] S. Roberts, *Lecture 7: The Discrete Fourier Transform*, Lecture notes for Signal Processing, University of Oxford, Accessed: 27-11-2025, n.d. [Online]. Available: https://www.robots.ox.ac.uk/~sjrob/Teaching/SP/l7.pdf.

[44] *Wavelet toolbox for use with MATLAB : user's guide version 3*, eng, Repr. version 3.0.2. Natick (MA): : The MathWorks, 2006.

[45] N. Kutz, *Time Frequency Analysis & Wavelets*, YouTube, Channel: Nathan Kutz. Accessed: 27-11-2025, Jul. 2016. [Online]. Available: https://www.youtube.com/watch?v=ViZYXxuxUKA.

[46] S. Mallat, *A Wavelet Tour of Signal Processing: The Sparse Way*, 3rd. Burlington, MA: Academic Press, 2009.

[47] A. Graps, “"an introduction to wavelets",” *IEEE Comp. Sci. Engi.*, vol. 2, pp. 50–61, Feb. 1995. DOI: 10.1109/99.388960.

[48] C. K. Chui, *An Introduction to Wavelets* (Wavelet Analysis and Its Applications). San Diego, CA: Academic Press, 1992, vol. 1.

[49] C. Torrence and G. P. Compo, “A practical guide to wavelet analysis,” *Bulletin of the American Meteorological Society*, vol. 79, pp. 61–78, 1998. DOI: 10.1175/1520-0477(1998)079<0061:apgtwa>2.0.co;2.

[50] The MathWorks, Inc., *Continuous 1-d wavelet transform - matlab cwt*, Accessed: May 26, 2026, The MathWorks, Inc., Natick, MA, USA, 2026. [Online]. Available: https://www.mathworks.com/help/wavelet/ref/cwt.html.

[51] P. Stoica and R. L. Moses, *Spectral Analysis of Signals*. Upper Saddle River, NJ, USA: Pearson/Prentice Hall, 2005.

[52] B. Van Veen. “Practical digital signal processing.” YouTube Playlist, YouTube. (2014), [Online]. Available: https://www.youtube.com/playlist?list=PLGI7M8vwfrFM08D4s2vUGIKRHw7W1rMvG (visited on 05/13/2026).

[53] C. L. Nikias and A. P. Petropulu, *Higher-Order Spectra Analysis: A Nonlinear Signal Processing Framework*. Englewood Cliffs, NJ: Prentice-Hall, 1993.

[54] G. Koukiou, “Identifying system non-linearities by fusing signal bispectral signatures,” *Electronics*, vol. 13, no. 7, p. 1287, 2024. DOI: 10.3390/electronics13071287.

[55] Y. C. Kim and E. J. Powers, “Digital bispectral analysis and its applications to nonlinear wave interactions,” *IEEE Transactions on Plasma Science*, vol. 7, no. 2, pp. 120–131, 1979. DOI: 10.1109/tps.1979.4317207.

[56] S. Elgar and R. T. Guza, “Statistics of bicoherence,” *IEEE Transactions on Acoustics, Speech, and Signal Processing*, vol. 36, no. 10, pp. 1667–1668, 1988. DOI: 10.1109/29.7555.

[57] B. P. van Milligen *et al.*, "Wavelet bicoherence: A new turbulence analysis tool," *Physics of Plasmas*, vol. 2, no. 8, pp. 3017–3032, 1995. DOI: 10.1063/1.871199.

[58] P. Z. Poloskei, G. Papp, G. Por, L. Horvath, and G. I. Pokol, "Bicoherence analysis of nonstationary and nonlinear processes," *arXiv preprint arXiv:1811.02973*, 2018. DOI: 10.48550/arxiv.1811.02973.

[59] Z. Ge, "Significance testing for wavelet bicoherence and its application in analyzing nonlinearity in turbulent shear flows," *Physical Review E*, vol. 81, no. 5, p. 056 311, 2010. DOI: 10.1103/PhysRevE.81.056311.

[60] L. Gelman, K. Soliński, and A. Ball, "Novel instantaneous wavelet bicoherence for vibration fault detection in gear systems," *Energies*, vol. 14, no. 20, p. 6811, 2021. DOI: 10.3390/en14206811.

[61] Z. Ge, "Significance tests for the wavelet cross spectrum and wavelet linear coherence," *Annales Geophysicae*, vol. 26, no. 12, pp. 3819–3829, 2008. DOI: 10.5194/angeo-26-3819-2008.

[62] F. J. Harris, "On the use of windows for harmonic analysis with the discrete fourier transform," *Proceedings of the IEEE*, vol. 66, no. 1, pp. 51–83, 1978. DOI: 10.1109/PROC.1978.10837.

[63] J. W. Kirchner, *Data analysis toolkit {#}12: Weighted averages and their uncertainties*, Course notes for Analysis of Environmental Data, University of California, Berkeley, Accessed: May 2026, 2006. [Online]. Available: https://seismo.berkeley.edu/~kirchner/Toolkits/Toolkit_12.pdf.

[64] F. Li, G. Meng, K. Kageyama, Z. Su, and L. Ye, "Optimal mother wavelet selection for lamb wave analyses," *Journal of Intelligent Material Systems and Structures*, vol. 20, pp. 1147–1161, Jun. 2009. DOI: 10.1177/1045389X09102562.

[65] M. Rhif, A. Ben Abbes, B. Martínez, I. R. Farah, and M. A. Gilabert, "Optimal selection of wavelet transform parameters for spatio-temporal analysis based on non-stationary ndvi modis time series in mediterranean region," *ISPRS Journal of Photogrammetry and Remote Sensing*, vol. 193, pp. 216–233, 2022. DOI: https://doi.org/10.1016/j.isprsjprs.2022.09.007. [Online]. Available: https://www.sciencedirect.com/science/article/pii/S092427162200243X.

[66] M. Farge, "Wavelet transforms and their applications to turbulence," *Annual Review of Fluid Mechanics*, vol. 24, pp. 395–457, 1992. DOI: 10.1146/annurev.fluid.24.1.395.

[67] J. M. Lilly and S. C. Olhede, "Higher-order properties of analytic wavelets," *Lilly, J. M., and S. C. Olhede, (2009). Higher-order properties of analytic wavelets. IEEE Transactions on Signal Processing, 57 (1), 146–160*, 2008. DOI: 10.1109/TSP.2008.2007607.

[68] T. Lafleur, S. D. Baalrud, and P. Chabert, "Theory for the anomalous electron transport in hall effect thrusters. i. insights from particle-in-cell simulations," *Physics of Plasmas*, vol. 23, no. 5, p. 053 502, May 2016. DOI: 10.1063/1.4948495. eprint: https://pubs.aip.org/aip/pop/article-pdf/doi/10.1063/1.4948495/15938713/053502_1_online.pdf. [Online]. Available: https://doi.org/10.1063/1.4948495.

[69] B. Illowsky and S. Dean, *Introductory Statistics*. OpenStax, 2013, Available for free at OpenStax. [Online]. Available: https://openstax.org/books/introductory-statistics/pages/1-introduction.

[70] P. Z. Peebles Jr., *Probability, Random Variables and Random Signal Principles*, 4th. New York: McGraw-Hill, 2001.

[71] G. Casella and R. L. Berger, *Statistical Inference*, 2nd ed. Pacific Grove, CA: Duxbury, 2002.

[72] A. Marín-Cebrián, E. Bello-Benítez, A. Domínguez-Vázquez, and E. Ahedo, "Non-maxwellian electron effects on the macroscopic response of a hall thruster discharge from an axial–radial kinetic model," *Plasma Sources Science and Technology*, vol. 33, Feb. 2024. DOI: 10.1088/1361-6595/ad227c.

[73] M.-C. Casabán, J.-C. Cortés, J.-V. Romero, and M.-D. Roselló, "Determining the first probability density function of linear random initial value problems by the random variable transformation (rvt) technique: A comprehensive study," *Abstract and Applied Analysis*, vol. 2014, no. 1, p. 248 512, 2014. DOI: https://doi.org/10.1155/2014/248512.

[74] C. Fassino, G. Pistone, and M. P. Rogantin, "Computing the moments of the complex Gaussian: Full and sparse covariance matrix," *Mathematics*, vol. 7, no. 3, p. 263, Mar. 2019. DOI: 10.3390/math7030263. [Online]. Available: https://www.mdpi.com/2227-7390/7/3/263.

[75] A. Winkelbauer, "Moments and absolute moments of the normal distribution," *arXiv*, 2012. DOI: 10.48550/arxiv.1209.4340.

[76] R. G. Gallager, "Circularly-symmetric Gaussian random vectors," Massachusetts Institute of Technology, Lecture notes, Jan. 2008, Accessed: 2026-05-25. [Online]. Available: https://www.rle.mit.edu/rgallager/documents/CircSymGauss.pdf.

[77] Tarifa Luz Hora, *Precio de la luz hoy por horas*, Web Portal, 2026. [Online]. Available: https://tarifaluzhora.es/.

A. CWT OF A CONSTANT-VALUED SIGNAL

Let $x(t)$ be a signal of constant value C. Then, the CWT of x is given by:

$$W_\psi[x](b,a) = \frac{1}{\sqrt{|a|}} \int_{-\infty}^{\infty} x(t) \cdot \bar{\psi}\left(\frac{t-b}{a}\right) dt = \frac{C}{\sqrt{|a|}} \int_{-\infty}^{\infty} \bar{\psi}\left(\frac{t-b}{a}\right) dt$$

To simplify the integral, a substitution factor u is introduced, so that:

$$u = \frac{t-b}{a} \qquad \Longrightarrow \; dt = a\,du$$

Substituting into the integral yields:

$$W_\psi[x](b,a) = \frac{C}{\sqrt{|a|}} |a| \int_{-\infty}^{\infty} \bar{\psi}\left(\frac{t-b}{a}\right) dt = C\sqrt{|a|} \int_{-\infty}^{\infty} \bar{\psi}(u)\; du \tag{A.1}$$

Since $a \in \mathbb{R}$ and the limits of integration do not change (as $\pm t \to \pm\infty$, then $\pm u \to \infty$), a is taken out of the integral as an absolute value. Now, to solve the integral, the wavelet admissibility condition is used. According to this condition, any wavelet must fulfill that:

$$C_\psi = \int_{-\infty}^{\infty} \frac{|\Psi(\omega)|^2}{|\omega|} d\omega \; < \infty$$

Focusing on a small interval around the origin $[-\epsilon, \epsilon]$ such that $0 < \epsilon \ll 1$, the latter expression becomes:

$$\int_{-\epsilon}^{\epsilon} \frac{|\Psi(\omega)|^2}{|\omega|} d\omega \; < \infty$$

Now, assume that $\Psi(\omega)$ is continuous at $\omega = 0$ and that $|\Psi(\omega)|^2 = k$, where k is a positive non-zero constant. As a result, the integral evaluated close to $\omega = 0$ behaves like:

$$\int_{-\epsilon}^{\epsilon} \frac{k}{|\omega|} d\omega = 2k \int_{0}^{\epsilon} \frac{1}{\omega} d\omega$$

By solving the integral, it can be seen that it diverges:

$$2k \int_{0}^{\epsilon} \frac{1}{\omega} d\omega = 2k[\ln(\omega)]_0^\epsilon = 2k\,(\ln(\epsilon) - \ln(0)) = \infty$$

Thus, the only way to prevent this divergence is that the transform of the wavelet at $\omega = 0$ is zero: $\Psi(0) = 0$.

By definition, the Fourier transform of the wavelet is given by:

$$\Psi(\omega) = \int_{-\infty}^{\infty} \psi(t) \cdot \exp(-i\omega t)\, dt$$

Evaluating at $\omega = 0$, the previous expression yields:

$$\Psi(0) = \int_{-\infty}^{\infty} \psi(t) \cdot \exp(-i(0)t)\, dt = \int_{-\infty}^{\infty} \psi(t)\, dt = 0$$

Introducing this result into Equation A.1, it is proven that for a constant-valued signal, its CWT is equal to zero:

$$W_{\psi}[x](b, a) = 0$$

B. STATISTICAL PROPERTIES OF THE WAVELET BICOHERENCE

B.1. Noise Floor Level

The expressions provided by Ge to obtain the α-significance level for the wavelet bicoherence are given by [59]:

$$\int_{D_\alpha}^{\infty} f_{[b^w]^2}(z)\, dz = \alpha \tag{B.1}$$

$$f_{[b^w]^2}(z) = \frac{\sqrt{N_e}}{\sqrt{2\pi z}(1-z)} \exp\left(-\frac{\operatorname{arctanh}^2(\sqrt{z})}{2/N_e}\right) \tag{B.2}$$

where N_e was defined in Section 3.3.3 (Equation 3.15). Note that in Equation B.1, the upper limit of integration can be changed from ∞ to 1. This is due to the fact that the WB is only defined between zero and one: $b^w \in [0, 1]$. As a result, the probability of obtaining a value greater than one is zero.

Introducing Equation B.2 into B.1 gives:

$$\int_{D_\alpha}^{1} \frac{\sqrt{N_e}}{\sqrt{2\pi z}(1-z)} \exp\left(-\frac{\operatorname{arctanh}^2(\sqrt{z})}{2/N_e}\right) dz = \alpha \tag{B.3}$$

To solve this integral, the following substitution is used:

$$\sqrt{z} = \tanh(u) \implies z = \tanh^2(u)$$

Now, taking derivatives:

$$du = \frac{1}{1-z} \cdot \frac{1}{2\sqrt{z}} \cdot dz \qquad \Rightarrow \qquad dz = 2\sqrt{z}(1-z)\, du$$

Applying these changes to Equation B.3 yields:

$$\int_{u_\alpha}^{\infty} \frac{\sqrt{N_e}}{\sqrt{2\pi z}(1-z)} \exp\left(-\frac{\operatorname{arctanh}^2(\sqrt{z})}{2/N_e}\right) 2\sqrt{z}(1-z)\, du = \alpha$$

where $u_\alpha = \operatorname{arctanh}^2(\sqrt{D_\alpha})$. Rearranging the terms the following is obtained:

$$\int_{u_\alpha}^{\infty} \frac{1}{\sqrt{2\pi(1/N_e)}} \exp\left(-\frac{u^2}{2(1/N_e)}\right) du = \alpha/2 \tag{B.4}$$

Before further simplifying the above equation, let us take a look at the probability density function of a normal distribution [69]:

$$f_N(x) = \frac{1}{\sqrt{2\pi\sigma^2}} \exp\left(-\frac{(x-\mu)^2}{2\sigma^2}\right)$$

Thus, Equation B.4 can be seen as the integral of the upper tail probability of a normal distribution with a mean of $\mu = 0$ and a variance of $\sigma^2 = 1/N_e$. As a result, the α-significance can be expressed as a function of the Z-score:

$$Z_{\alpha/2} = \frac{u_\alpha}{1/\sqrt{N_e}}$$

After reversing the substitution, the following expression is obtained:

$$D_\alpha = \tanh^2\left(\frac{Z_{\alpha/2}}{\sqrt{N_e}}\right)$$

Finally, for a confidence level of 95%, $\alpha = 0.05$, so $Z_{\alpha/2} = Z_{0.025} \approx 1.96$. Thus, the expression for the significance threshold is:

$$\epsilon\left[[b^w(\omega_1, \omega_2)]^2\right] = D_{0.05} = \tanh^2\left(\frac{1.96}{\sqrt{N_e}}\right)$$

C. STATISTICAL PROPERTIES OF THE INSTANTANEOUS WAVELET BICOHERENCE

C.1. Noise Floor Level

The derivation begins with the expression for the WB introduced in Section 3.3.3 (Equation 3.13). Now, let us define the IWB estimator as:

$$\left[\hat{b}^w\right]^2 = \frac{\left|\frac{1}{M}\sum_{m=1}^{M} W_{x,m}(t,a_1)\cdot W_{x,m}(t,a_2)\cdot \bar{W}_{x,m}(t,a_3)\right|^2}{\left(\frac{1}{M}\sum_{m=1}^{M}\left|W_{x,m}(t,a_1)\cdot W_{x,m}(t,a_2)\right|^2\right)\cdot\left(\frac{1}{M}\sum_{m=1}^{M}\left|W_{x,m}(t,a_3)\right|^2\right)} \tag{C.1}$$

where $W_{x,m}(t,a_i)$ denotes the m$^{\text{th}}$ realization of the CWT of a function x at a time t and scale a_i. To simplify the notation, the following variables are introduced:

- $A_m = W_{x,m}(t,a_1)\cdot W_{x,m}(t,a_2)\cdot \bar{W}_{x,m}(t,a_3)$
- $B_m = \left|W_{x,m}(t,a_1)\cdot W_{x,m}(t,a_2)\right|^2$
- $C_m = \left|W_{x,m}(t,a_3)\right|^2$

So, Equation C.1 becomes:

$$\left[\hat{b}^w\right]^2 = \frac{\left|\frac{1}{M}\sum_{m=1}^{M} A_m\right|^2}{\left(\frac{1}{M}\sum_{m=1}^{M} B_m\right)\cdot\left(\frac{1}{M}\sum_{m=1}^{M} C_m\right)} \tag{C.2}$$

Since the goal is to find the statistical error (noise floor) for the IWB, it is assumed that the true bicoherence is exactly zero. In other words, since the signal being analyzed is Gaussian white noise, there is no bicoherence in the signal. Under this assumption, the expected value of the numerator must be zero, which implies $\mathrm{E}\{A_m\} = 0$.

Taking a closer look at the denominator, by the Law of Large Numbers, if the number of samples M is large enough, the sample means $(1/M)\sum B_m$, and $(1/M)\sum C_m$ converge to their expected values $\mathrm{E}\{B_m\}$ and $\mathrm{E}\{C_m\}$. As a result, the denominator can be treated as a constant V:

$$V = \mathrm{E}\{B_m\}\cdot \mathrm{E}\{C_m\}$$

Returning to the numerator, $\hat{N}$ is defined as the sample mean of the crossed terms:

$$\hat{N} = \frac{1}{M}\sum_{m=1}^{M} A_m$$

Since the realizations of the signal are independent of each other, A_m is also independent. Thus, by the application of the Central Limit Theorem [69], for large M, $\hat{N}$ converges to a complex Gaussian distribution. Thus, $\hat{N}$ can be seen as a Gaussian distribution with zero-mean. Furthermore, since A_m is independent across realizations, the variance of the sample mean is [71]:

$$\begin{aligned}
\mathrm{Var}\{\hat{N}\} =& \mathrm{Var}\left\{\frac{1}{M}\sum_{m=1}^{M} A_m\right\} = \frac{1}{M^2}\sum_{m=1}^{M}\mathrm{Var}\{A_m\} = \frac{1}{M}\mathrm{Var}\left\{A_m\right\} \\
=& \frac{1}{M}\mathrm{E}\left\{|A_m - \mathrm{E}\{A_m\}|^2\right\} = \frac{1}{M}\mathrm{E}\left\{|A_m|^2\right\}
\end{aligned}$$

In order to obtain the expected value of $|A_m|^2$, the multiplicative property of complex numbers can be applied. In this way:

$$\begin{aligned}
|A_m|^2 &= \left|W_{x,m}(t, a_1) \cdot W_{x,m}(t, a_2) \cdot \bar{W}_{x,m}(t, a_3)\right|^2 \\
&= \left|W_{x,m}(t, a_1) \cdot W_{x,m}(t, a_2)\right|^2 \cdot \left|\bar{W}_{x,m}(t, a_3)\right|^2 = B_m \cdot C_m
\end{aligned}$$

Taking the expected value on both sides gives:

$$\mathrm{E}\left\{|A_m|^2\right\} = \mathrm{E}\left\{B_m \cdot C_m\right\}$$

Under the null hypothesis that the signal being analyzed is Gaussian white noise, the wavelet coefficients also follow a zero-mean circularly-symmetric[9] complex Gaussian variables and are uncorrelated at different scales, i.e. $\mathrm{E}\left\{W_{x,m}(t, a_i) \cdot \bar{W}_{x,m}(t, a_j)\right\} = 0$ for $i \neq j$. This allows the use of Isserlis' theorem[10] to simplify the above expression by separating the expectation of B_m and C_m:

[9]Given a complex random vector $\vec{Z}$, it is said to be circularly-symmetric if its probability distribution remains unchanged by rotations, i.e. $\vec{Z} \overset{d}{=} e^{i\theta}\vec{Z} \quad \forall\theta \in \mathbb{R}$. In the case of complex Gaussian variable Z, this is true if and only if the imaginary and real parts of the random vector are independent and equally distributed. [76].

[10]The complex Isserlis' theorem states that for a complex multivariate normally distributed random vector with zero-mean, then $\mathrm{E}(Y_1 Y_2 \cdots Y_n \bar{Y}_1 \bar{Y}_2 \cdots \bar{Y}_n) = \sum_{\sigma\in S(n)} \prod_{k=1}^{n} \mathrm{E}(Y_k \bar{Y}_{\sigma(k)})$, where $S(n)$ is the symmetric group of permutations on $\{1, \ldots, n\}$, e.g. $S(3) = \{e, (1\,2), (1\,3), (2\,3), (1\,2\,3), (1\,3\,2)\}$, where e denotes the identity permutation [74].

$$
\begin{aligned}
\mathrm{E}\left\{|A_m|^2\right\} &= \mathrm{E}\left\{\left|W_{x,m}(t,a_1)\cdot W_{x,m}(t,a_2)\cdot \bar{W}_{x,m}(t,a_3)\right|^2\right\} \\
&= \mathrm{E}\left\{W_{x,m}(t,a_1)\cdot \bar{W}_{x,m}(t,a_1)\cdot W_{x,m}(t,a_2)\cdot \bar{W}_{x,m}(t,a_2)\cdot W_{x,m}(t,a_3)\cdot \bar{W}_{x,m}(t,a_3)\right\} \\
&= \mathrm{E}\left\{W_{x,m}(t,a_1)\cdot \bar{W}_{x,m}(t,a_1)\right\}\cdot \mathrm{E}\left\{W_{x,m}(t,a_2)\cdot \bar{W}_{x,m}(t,a_2)\right\}\cdot \mathrm{E}\left\{W_{x,m}(t,a_3)\cdot \bar{W}_{x,m}(t,a_3)\right\} \\
&= \mathrm{E}\left\{W_{x,m}(t,a_1)\cdot \bar{W}_{x,m}(t,a_1)\cdot W_{x,m}(t,a_2)\cdot \bar{W}_{x,m}(t,a_2)\right\}\cdot \mathrm{E}\left\{W_{x,m}(t,a_3)\cdot \bar{W}_{x,m}(t,a_3)\right\} \\
&= \mathrm{E}\left\{\left|W_{x,m}(t,a_1)\cdot W_{x,m}(t,a_2)\right|^2\right\}\cdot \mathrm{E}\left\{\left|W_{x,m}(t,a_3)\right|^2\right\} \\
&= \mathrm{E}\left\{B_m\right\}\cdot \mathrm{E}\left\{C_m\right\} = V
\end{aligned}
$$

So, the variance of $\hat{N}$ is V/M. Since, as mentioned before, $\hat{N}$ is a complex normal distribution, its real and imaginary parts also follow a normal distribution with zero-mean and variance $V/2M$ [70]. With this in mind, the numerator of Equation C.2 can be seen as the sum of two squared Gaussian variables:

$$
\left|\hat{N}\right|^2 = \mathrm{Re}\left(\hat{N}\right)^2 + \mathrm{Im}\left(\hat{N}\right)^2 \tag{C.3}
$$

The above expression can be expressed in terms of two independent standard normal distributions $Z_1, Z_2 \sim \mathcal{N}(0,1)$. The relations between these variables and the real and imaginary components of $\hat{N}$ are given by [69]:

$$
Z_1 = \frac{\mathrm{Re}\left(\hat{N}\right) - \mu_R}{\sigma_R} = \frac{R-\mu_R}{\sigma_R} \qquad \Rightarrow \qquad R^2 = \frac{V}{2M}Z_1^2
$$

$$
Z_2 = \frac{\mathrm{Im}\left(\hat{N}\right) - \mu_I}{\sigma_I} = \frac{I-\mu_I}{\sigma_I} \qquad \Rightarrow \qquad I^2 = \frac{V}{2M}Z_2^2
$$

Applying these changes to Equation C.3 yields:

$$
\left|\hat{N}\right|^2 = \frac{V}{2M}\left(Z_1^2 + Z_2^2\right) = \frac{V}{2M}Z
$$

where $Z = Z_1^2 + Z_2^2$. Here, the latter expression follows a Chi-squared distribution with 2 degrees of freedom multiplied by $V/2M$ [69]:

$$
\left|\hat{N}\right|^2 \sim \frac{V}{2M}\chi_2^2
$$

For the Chi-squared distribution with k degrees of freedom, the PDF for $x > 0$ is given by [70]:

$$
f_X(x) = \frac{x^{(k/2)-1}}{2^{k/2}}\frac{1}{\Gamma(k/2)}e^{-x/2} \tag{C.4}
$$

where Γ is the gamma function [70]:

$$\Gamma(l) = \int_0^\infty \xi^{l-1}\, e^{-\xi}\, d\xi$$

In the case of the random variable Z, Equation C.4 becomes:

$$f_Z(z) = \frac{1}{2} e^{-z/2}$$

With this, the PDF for the numerator in Equation C.2 can be obtained [73]:

$$f_{|\hat{N}|^2}(u) = f_Z\left(\frac{2M}{V}u\right) \cdot \left|\frac{d}{du}\left(\frac{2M}{V}u\right)\right| = \frac{M}{V} e^{-Mu/V}$$

With this, a similar thing can be done, since Equation C.2 can be expressed as $\left[\hat{b}^w\right]^2 = \left|\hat{N}\right|^2 / V$. In an analogous way to what was done in the previous step, the PDF of the bicoherence is given as:

$$f_{[\hat{b}^w]^2}(x) = f_Z\,(Vx) \cdot \left|\frac{d}{dx}\,(Vx)\right| = Me^{-Mx}$$

From this, it is clear that the IWB follows an exponential distribution with $\lambda = M$. From this it can be concluded that the α-significance level for the IWB is given by:

$$\int_{D_\alpha}^\infty Me^{-Mz} dz = \alpha$$

Solving the integral gives:

$$D_\alpha = \frac{-\ln(\alpha)}{M}$$

For a significance level of 95% ($\alpha = 0.05$) this gives:

$$\epsilon\left[[b^w(\omega_1, \omega_2)]^2\right] = \frac{3}{M}$$

DECLARACIÓN DE USO DE IA GENERATIVA EN EL TRABAJO DE FIN DE GRADO

He usado IA Generativa en este trabajo

Marca lo que corresponda: *SI*

SI	NO

Si has marcado SI, completa las siguientes 3 partes de este documento:

Parte 1: reflexión sobre comportamiento ético y responsable

Ten presente que el uso de IA Generativa conlleva unos riesgos y puede generar una serie de consecuencias que afecten a la integridad moral de tu actuación con ella. Por eso, te pedimos que contestes con honestidad a las siguientes preguntas (*Marca lo que corresponda*):

Pregunta		
1. En mi interacción con herramientas de IA Generativa he remitido **datos de carácter sensible** con la debida autorización de los interesados.		
SÍ, he usado estos datos con autorización	NO, he usado estos datos sin autorización	NO, no he usado datos de carácter sensible
2. En mi interacción con herramientas de IA Generativa he remitido **materiales protegidos por derechos de autor** con la debida autorización de los interesados.		
SÍ, he usado estos materiales con autorización	NO, he usado estos materiales sin autorización	NO, no he usado materiales protegidos
3. En mi interacción con herramientas de IA Generativa he remitido **datos de carácter personal** con la debida autorización de los interesados.		
SÍ, he usado estos datos con autorización	NO, he usado estos datos sin autorización	NO, no he usado datos de carácter personal

4. Mi utilización de la herramienta de IA Generativa ha **respetado sus términos de uso**, así como los principios éticos esenciales, no orientándola de manera maliciosa a obtener un resultado inapropiado para el trabajo presentado, es decir, que produzca una impresión o conocimiento contrario a la realidad de los resultados obtenidos, que suplante mi propio trabajo o que pueda resultar en un perjuicio para las personas.	
SI	NO

Si **NO** has contado con la autorización de los interesados en alguna de las preguntas 1, 2 ó 3, explica brevemente el motivo *(por ejemplo, "los materiales estaban protegidos pero permitían su uso para este fin" o "los términos de uso, que se pueden encontrar en esta dirección (…), impiden el uso que he hecho, pero era imprescindible dada la naturaleza del trabajo".*

Parte 2: declaración de uso técnico

Utiliza el siguiente modelo de declaración tantas veces como sea necesario, a fin de reflejar todos los tipos de iteración que has tenido con herramientas de IA Generativa. Incluye un ejemplo por cada tipo de uso realizado donde se indique: *[Añade un ejemplo].*

Declaro haber hecho uso del sistema de IA Generativa ChatGPT, Gemini, Claude y Copilot para:

Documentación y redacción:

- *Soporte a la reflexión en relación con el desarrollo del trabajo: proceso iterativo de análisis de alternativas y enfoques utilizando la IA*

Todos los modelos descritos con anterioridad han sido para explorar y evaluar distintas ideas antes de la incorporación en el texto. Por ejemplo: "I am currently working on the chapter of my thesis related to signal processing and I am having some problems with the notation. For discrete signals people usually utilize the index \$k\$, but in the context of my project this might be confused with the symbol I use for wavenumbers, which is also \$k\$. Could you please propose symbols I could use to indicate the Fourier index. For each of the candidates I want you to check if it interferes with any other symbol on my thesis."

- *Revisión o reescritura de párrafos redactados previamente*

Para los todos modelos descritos con anterioridad para la revisión gramatical del texto, identificación de errores lógicos y uso símbolos matemáticos inconsistentes o errores en las ecuaciones. A estos modelos sólo se les ha pedido la identificación de estos errores, no la modificación de manera automática. Los errores encontrados han sido resueltos de manera manual.

- *Búsqueda de información o respuesta a preguntas concretas*

Los modelos de ChatGPT, Gemini y Claude han sido utilizados para buscar referencias académicas. Para ello se les ha dado un contexto del tema y se les ha solicitado la búsqueda de referencias académicas. Ejemplo: "I am working on my bachelor thesis, which talks about ECDI instabilities in plasma discharges. Since I am getting started with this topic I would like to know more about the physics behind this phenomenon. To do so, I would like you to help me by providing 10 different academic resources (books, papers, etc.) so that I can learn more about it. If you find less than 10 references, please do not make up new ones or propose unrelated ones. In addition, for each of the sources provide a working link, make sure it is accessible today."

- *Búsqueda de bibliografía*

Se ha aplicado el mismo método descrito en el anterior punto.

- *Resumen de bibliografía consultada*

Los modelos de ChatGPT, Gemini y Claude han sido utilizados para resumir los documentos reunidos usando el anterior prompt. El proceso de iteración ha sido el siguiente: Pedir a los modelos diferentes fuentes → Descargar los contenidos → Pedir un resumen de cada una de las fuentes usando el siguiente prompt: "I have just given you a paper/book about X topic, I would like you to sumarize the whole text/a certain chapter using three bullet points. Be concise." → Selección manual de las fuentes más relevantes → Leer el documento y tomar apuntes.

- *Traducción de texto consultados*

No se ha solicitado la traducción de ningún texto.

Desarrollar contenido específico

Se ha hecho uso de IA Generativa como herramienta de soporte para el desarrollo del contenido específico del TFG, incluyendo:

- *Asistencia en el desarrollo de líneas de código (programación)*

He utilizado todos los modelos descritos con anterioridad para entender como funcionaban ciertas funciones de la librería estándar de MATLAB. Por ejemplo, el orden en el que la función `fft` devuelve el domino de frecuencias.

- *Generación de esquemas, imágenes, audios o vídeos*

Ninguno de los modelos ha sido utilizado para crear contenido multimedia.

- *Procesos de optimización*

Todos los modelos descritos con anterioridad han sido utilizados para identificar errores en el código, optimizar bucles anidados vía vectorización de las matrices y el uso de las matrices optimizadas para su uso en GPU que provee MATLAB

- *Tratamiento de datos: recogida, análisis, cruce de datos…*

Ninguno de los modelos se ha usado directamente para el tratamiento de datos.

- *Inspiración de ideas en el proceso creativo*

Ninguno de los modelos ha sido usados para la inspiración en el proceso creativo de la tesis.

- *Otros usos vinculados a la generación de puntos concretos del desarrollo específico del trabajo*

Parte 3: reflexión sobre utilidad

Por favor, aporta una valoración personal (formato libre) sobre las fortalezas y debilidades que has identificado en el uso de herramientas de IA Generativa en el desarrollo de tu trabajo. Menciona si te ha servido en el proceso de aprendizaje, o en el desarrollo o en la extracción de conclusiones de tu trabajo.

La Inteligencia Artificial ha sido una herramienta que me ha ayudado en el desarrollo de mi tesis y ha acelerado mi proceso de aprendizaje durante la realización de esta. A diferencia de buscadores convencionales, la IA entiende el contexto, por lo que resulta una herramienta muy útil para la búsqueda de información. Además, en el ámbito de la programación tiene unas habilidades considerablemente mayores que las de cualquier ingeniero que no está directamente especializado en software, por lo que es de gran ayuda para optimizar códigos o encontrar errores que requieren un mayor entendimiento de la arquitectura del lenguaje que se está usando. A pesar de esto, hoy en día, la IA sigue teniendo grandes limitaciones. Una de las principales es que no es capaz de explicar conceptos complejos sin un contexto anterior. Un ejemplo sería que explicase con profundidad como funciona la bicoherencia wavelet. Aunque en ámbitos generales va a saber describir este método, todavía falla en los pequeños detalles que suponen la diferencia entre saber de qué va el método de manera general y entenderlo con profundidad y saber aplicarlo correctamente. Otras de estas limitaciones son las alucinaciones. A pesar de que a veces le digamos al modelo que no invente o no mienta, sigue teniendo delirios y añadiendo información que afirma ser verdad, pero que omite la fuente ya que es una invención del modelo.